C. P. Mook, RV-1

NASA CR-73443

003

FINAL REPORT

SOLAR WIND SIMULATION TECHNIQUES

By
H. J. KING AND D. E. ZUCCARO

HUGHES RESEARCH LABORATORIES
3011 Malibu Canyon Road
Malibu, California 90265

Prepared for

NATIONAL AERONAUTICS AND SPACE ADMINISTRATION
AMES RESEARCH CENTER

APRIL 1970

CONTRACT NAS 2-5585

NASA CR-73443

SOLAR WIND SIMULATION TECHNIQUES

By H.J. King and D.E. Zuccaro

April 1970

Prepared under Contract No. NAS 2-5585
HUGHES RESEARCH LABORATORIES
Malibu, California 90265

for

AMES RESEARCH CENTER
NATIONAL AERONAUTICS AND SPACE ADMINISTRATION

PRECEDING PAGE BLANK NOT FILMED.

TABLE OF CONTENTS

LIST OF ILLUSTRATIONS

SECTION I

INTRODUCTION AND SUMMARY

The goals of this program were to analyze the techniques for laboratory simulation of the solar wind and to establish an optimized design for such a system. Simulation of the solar wind is necessary for the development of long lived, radiation-resistant thermal control coatings for use on spacecraft. This program was motivated by the fact that laboratory experiments did not appear to duplicate the changes that occurred in the thermal control coatings used on operational spacecraft.

This study consists of four major elements: (1) the evaluation of the experimental data of the solar wind, (2) the establishment of a set of requirements for a solar wind simulation system, (3) the evaluation of the techniques and apparatus that could be used to generate the required ion beam, and (4) the design of an optimized solar wind simulation system.

This study was limited to the simulation of energetic particulate solar radiation (i.e., protons, alpha particles, highly charged heavy ions, and electrons), and did not include consideration of the simulation of the solar photon (i.e., electromagnetic) radiation. It also did not extend to the analysis of the effects of the particulate radiation on the thermal control coatings.

The first task was to characterize the solar wind. Under quiet sun conditions, the solar wind consists of about 95% H^+, 4% He^{2+}, and 0.5% heavy ions of which only O^{7+}, O^{6+}, and O^{5+} have been identified. During periods of solar activity, the He^{2+} (and by inference the heavy ion) concentration is greatly

increased. The H energy ranges from the quiet sun value of 0.5 keV to solar flare conditions of 3 keV, with a mean value about 1 keV. The normal particle flux is 2×10^{8} cm^{-2} sec^{-1}, which is equivalent to an ion current density of 3×10^{-11} A cm^{-2}. The solar wind electrons have a maximum energy in the range of 20 to 40 eV.

With this information concerning the solar wind and with limitations imposed by the experimental conditions, the requirements for the system are developed as part of the second task in this study. While the proton energy range of 0.5 to 3 keV and the flux range of 2×10^{8} cm^{-2} sec^{-1} for a normal exposure to a value of 2×10^{11} cm^{-2} sec^{-1} for accelerated testing are easily specified, the specification of the ion composition requires information about chemical and mass effects that is not presently available. Second order simulation with protons and alphas and third order simulation with protons, alphas, and stripped heavy ions are considered; however, because few, if any, experiments have been performed with an adequate first order simulation (only protons), this study was limited to a proton beam.

In addition to these requirements, the following set of test conditions was defined to achieve adequate first order simulation of the solar wind.

(a) Beam purity — The proton beam must be pure to avoid sample degradation by materials not present in the solar wind. The contaminants most likely to be found include fast charge-exchange neutrals, material sputtered from the electrodes or walls of the vacuum chamber, and Lyman alpha radiation generated by the hydrogen discharge in the source. The charge exchange neutrals, which are created when protons pass through a relatively high pressure hydrogen gas such as in the extraction canal of the ion source, are particularly bad because they are not easily detected and yet will produce degradation equivalent to protons of the same kinetic energy. The best means of

providing a pure beam is to physically deflect the desired particles (i.e., the protons) out of the beam and onto the target, leaving the contaminants (fast neutrals and Lyman alpha photons) to pass undeflected into a trap or onto the chamber walls (see section on mass separators).

(b) Test chamber pressure — It was estimated that the test chamber should be held to an ambient pressure of less than 5×10^{-7} Torr of background hydrogen pressure and that other gases have a total pressure of less than 1×10^{-8} Torr. It is particularly important to keep the test environment free of all hydrocarbons such as diffusion pump oil and vacuum grease.

(c) Sample temperatures — It was estimated that all tests would be conducted between the temperatures of 100 to 450°K.

(d) Test system lifetime — Typical tests were estimated to be of the order of 1000 hours. Some shorter tests may be conducted at an accelerated rate by increasing the flux density, although a limit based on a reciprocity failure relationship has not yet been defined. It is suggested that a valve be provided between the ion source and the sample chamber so that repairs or modifications to the source can be made if they become necessary during a test.

(e) Neutralization of surface charge — It was shown that a positive surface charge may accumulate on the samples when they are bombarded by the ion fluxes to be used during the test. While the extent of this accumulation depends on the sample resistivity, it is suggested that all tests be conducted with a neutralizer consisting of an electron gun which floods the target with 20 to 40 V electrons.

Figure IV-1 shows a typical solar wind simulator which is described in detail in the report. It consists of five basic elements — the proton source, the mass separator, the ion beam transport system, the beam measurement apparatus, and the vacuum system (which contains the entire device and provides the proper atmosphere for the tests). Each of the first three units is treated separately, and then an example design is discussed that includes a typical beam monitor apparatus and vacuum installation.

The ion source must provide a proton beam with the necessary energy, intensity, and stability over the desired lifetime. The only practical sources that provide the desired quantity of protons with a sufficiently small energy spread to traverse the mass separator, create the protons by electron bombardment of hydrogen gas. The characteristics of all the sources considered are summarized in Table IV-2 in the body of the report. Only two have the required properties. Of these, the rf discharge was chosen as most suitable because it is able to produce the desired total current required to irradiate 10 standard samples at an accelerated test rate 1000 times greater than the "standard" solar wind. The second choice — the low voltage electron source — is able to operate stably over a much wider current range than the rf source, but it is very inefficient at the high current levels and would place an undue load on the vacuum pumps. Techniques for extracting and focusing the protons from each of these sources are discussed.

The mass separator must bend the proton beam out of the main beam from the source, while introducing a minimum of aberrations that will perturb the beam uniformity at the target. The four types of separators studied and their characteristics are listed in Table IV-4. Again, two types — the

magnetic sector and crossed electric and magnetic field — were found suitable for this application. The magnetic sector was chosen for the example design, primarily because it is much more generally used and its performance more completely documented.

The ion optical system is critical in fulfilling the required specifications because it transports the ion beam from source to target and provides a means of attenuating the beam to achieve various flux levels. The output from the ion source and hence the input to the ion optical system are characterized by an emittance diagram that defines the angular divergence of the ion trajectories at every radius. The critical source parameters should be measured for any particular source to be used, before the ion optical system design is finalized. The basic philosophy of design used here was to maintain a small beam with little angular divergence along the path from the source through the separator up to the final lens, which expands the beam to cover the target. By keeping the beam diameter below 0.5 cm and using einzel or unipotential lenses 10 times this diameter, the aberrations can be kept small to preserve the laminar nature of the beam and hence the uniform coverage of the target. A digital computer technique was evolved to perform the iterative calculations to define the beam shape.

Two system advantages arise from this design. First, by keeping the beam small it is possible to insert a small aperture between the source and the target chamber. This aperture provides a relatively high impedance to the neutral hydrogen gas that flows from the ion source thus permitting a differential pumping system to be effectively used to remove the hydrogen before it raises the pressure in the target chamber. A second advantage is that with the system described above, it

is possible to maintain the beam diameter small all the way to the target and to substitute a set of deflection plates for the final diverging lens. These plates may be used to raster the small proton beam over the target. This rastering system has the advantages of providing more uniform target coverage, better control over the beam intensity, and more accurate measure of the beam intensity. The principal disadvantage is that the ion arrival at the target pulsates at the raster frequency; it has not yet been established that this accurately simulates a dc beam of an intensity equal to the average intensity of the rastered beam. Because of the significant system advantages, it is suggested that this point be established and that a rastered beam be used if possible.

The proton, electron, and photon detectors are mounted on the underside of the sample mounting plate. A faraday collector is used to determine the ion beam flux, flux distribution, energy, and energy spread. It is also used to monitor the beam during the run. A servo loop is used to adjust the beam parameters to hold them to a fixed value.

The vacuum system consists of two main elements — the beam forming components and the sample chamber. These can be isolated by means of a gate valve to permit pressurization of one half without affecting the other. The system is all metal, with titanium sublimation and sputter-ion pumps.

SECTION II

PARTICULATE ENVIRONMENT IN SPACE

The energetic particle flux found in space can be divided into three major categories. One includes a number of particles found within the space over which the earth's magnetic field extends. This consists of the "thermal plasma" which extends out from the ionosphere into the geomagnetic cavity, the plasma sheath, the Van Allen radiation belts, and the magneto-sheath. The second category is the solar plasma or solar wind found in the interplanetary regions. The third consists of the cosmic rays.

The particle environments of principal interest to the designers of spacecraft are the solar wind and the radiation that exists at synchronous orbit. Stanley and Ryan (Ref. II-1) have published an extensive summary of the synchronous orbit charged particle radiation environment. This section of this report summarizes the properties of the solar wind that have been determined by satellite probes. This summary will be used to establish the general requirements for an optimized solar wind simulator.

The solar wind is the term applied to the streaming plasma which is evolved from the sun. Because the energy of the particles is much greater than that which can be associated with the corona temperatures, it is believed to result from a supersonic expansion of the corona's charged particles coupled to the sun's magnetic field (Refs. II-2 to II-4). The plasma is neutral, having an equal number of positive charges and electrons per unit volume. The ions and electrons have much different velocities.

A. SOLAR WIND COMPOSITION

The most abundant ion is the hydrogen ion, H^+, (i.e., a proton). The second most abundant is that of helium He^{2+} (i.e., an alpha particle).* Although there are spectroscopic data indicating the presence of many other elements in the sun, only multiply charged oxygen ions O^{5+}, O^{6+}, and O^{7+} have been identified (Ref. II-6) at this time. Other ions are believed to be present, but their low relative abundance and the number of ionic states makes it very difficult to identify them by means of energy per charge detectors. The foil collector experiments made during the recent Apollo flight should provide more information about the heavy ion composition of the solar wind.

The He^{2+} to H^+ ratio (n_α/n_p) has been measured by the Vela satellite and found to vary from less than 1% to over 15% (Ref. II-5). This variation is believed to reflect true changes in the plasma composition. The average value of n_α/n_p (for quiet sun conditions) is about 4.5%.† During solar flares, the plasma contains a much greater He^{2+} content. In a recent class 3B flare, an n_α/n_p ratio of 22% was observed (Ref. II-7). Under this condition nearly half the charge of the solar wind is carried by the He^{2+} ions.

---

*The major part of the information in this section has been obtained from Hundhausen's paper on the direct observation of solar wind particles (Ref. II-5). Material not referenced to others was obtained from this paper.

†The n_α/n_p ratio was measured over a 2 year period by the Vela 3A and 3B satellites. During this time the ratio varied from 0.01 to 0.08 and had an average value of 0.037. (D.E. Robbins, A.T. Hundhausen, and S.J. Bame, J. Geophys. Res. 75, 1178 (1970).)

This indicates that the solar plasma composition varies with solar activity. The heavy ion components could be resolved only under quiet sun conditions. During this period it was about 0.5% (by number ratio) of the proton flux (Ref. II-6).

B. SOLAR WIND PARTICLE ENERGIES

The solar wind proton energies were first accurately measured by the Mariner 2 satellite (Ref. II-8) during the period September through December 1962. The average of the daily average proton velocity for the period was 504 km sec^{-1} (equivalent to 1325 eV energy).* The 3 hour averages ranged from a low energy of 532 eV (v = 319 km sec^{-1}) to a high energy of 3100 eV (v = 771 km sec^{-1}). A graph of the 3 hour average values of the plasma velocity and of the proton number density is presented in Fig. II-1. During this period the solar wind consisted of a series of long-lived high velocity streams separated by a slower plasma. This slower plasma is associated with the quiet sun condition and has an energy of about 534 to 603 eV (v = 320 to 340 km sec^{-1}).

*The satellite instrumentation measured the proton energy. These data were reported as a velocity using the following relationship

$$eV = \frac{1}{2} m_H v^2$$

$$V = 5.22 \times 10^{-9} v^2$$

$$v = 1.38 \times 10^{4} V^{1/2}$$

where

$e = 1.60 \times 10^{-19}$ coulomb

V = volts

$m_H = 1.67 \times 10^{-27}$ kgm (proton mass)

v = m sec^{-1}

In this summary, we have converted the velocities to the appropriate energy unit.

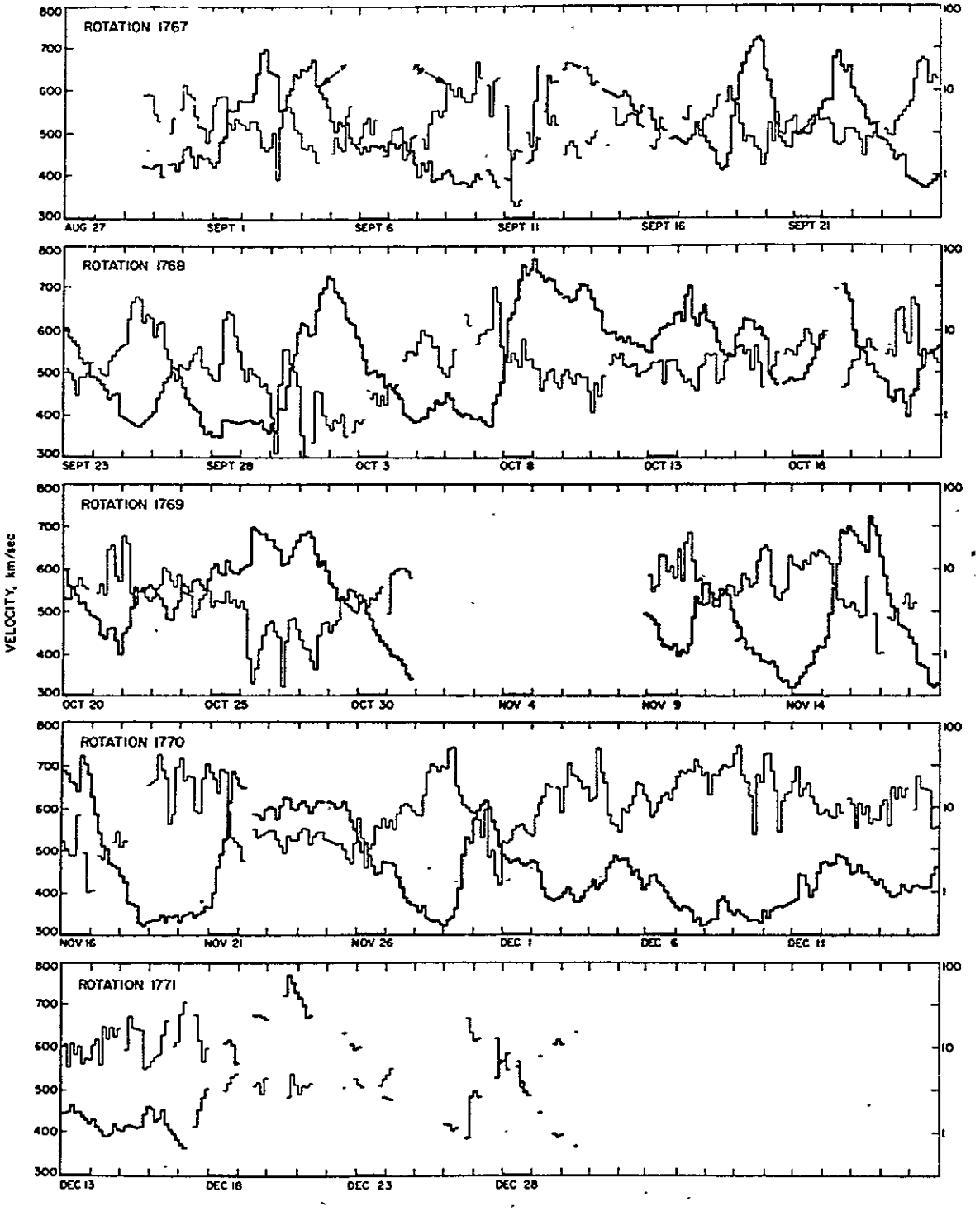

Fig. II-1. Three-hour averages of the solar wind flow speed and proton density, as measured on Mariner 2. The time interval has been broken into standard 27-day solar rotation periods (from Ref. II-8).

The Vela 2, Vela 3, and Vela 4 series of satellites have made observations over the period from 1964 to 1967, which was a period of minimum solar activity. During the period of July 1964 to July 1965, the Vela 2A and Vela 2B satellites (Ref. II-9) made about 13000 measurements. The mean value was 920 eV (v = 420 km sec^{-1}), and the largest number of cases were for a 550 eV (v = 325 km sec^{-1}) particle energy. This is shown in Fig. II-2. The largest peak appears to be associated with the quiet sun condition which was prevalent throughout most of this period.

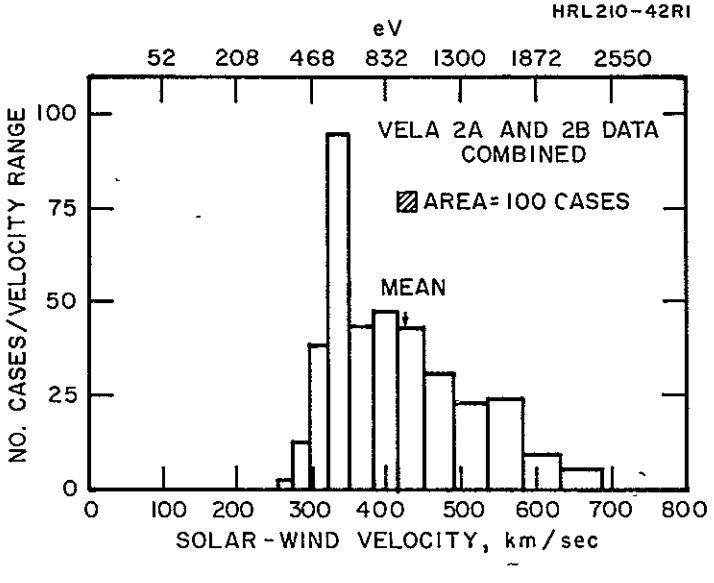

Fig. II-2. Distribution of solar-wind ion energy and velocity from July 1964 to July 1965 (from Ref. II-9).

The He^{2+} is observed to have an energy per charge (E/Q) ratio that is twice that of the protons (Refs. II-6, II-8). Thus the energy of the alpha particles is 4 times that of the protons. The highly charged heavy ions (O^{7+}, O^{6+}, and O^{5+}), which could be resolved only in a quiet sun period (Ref. II-6), had energies of about 14 keV and an E/Q ratio of 2.65 that of the protons.

In summary, the solar wind proton energy ranges from a low value of about 550 eV that is associated with quiet sun conditions, to a mean value in the neighborhood of 1000 eV and to an upper limit of about 3000 eV that is associated with solar flares. The energies of the He^{2+}, O^{7+}, O^{6+}, and O^{5+} are related to the solar activity in a similar fashion.

C. SOLAR WIND PARTICLE FLUX

The solar wind ion flux during quiet sun conditions is apparently a constant value of approximately 2×10^8 cm^{-2} sec^{-1}. The fraction of time in which the solar wind exhibits the quiet sun condition varies with the solar activity over the 11 year solar cycle. During the Mariner 2 measurements, which were made during a period of declining solar activity, the quiet sun condition was observed for short periods between long lived higher velocity plasma streams (see Fig. II-1). The average value of the density was 5.4 protons cm^{-3}, which leads to a flux of 2.4×10^8 protons cm^{-2} sec^{-1}. During the Vela 2 and 3 measurements, which took place during the minimum in solar activity, the quiet sun condition was present for a large fraction of the time.

During the quiet sun period in which the Vela series of satellites were operating, an average total positive ion flux of 1.75×10^8 positive electronic charges cm^{-2} sec^{-1} were observed (Ref. II-5). Under these conditions the plasma consisted of approximately 4.5% He^{2+} (by number), which represents about 9% of the total charge in the solar plasma.* The differences in these values reflects both a difference in the degree of solar activity and that the Mariner 2

*The aluminum foil collector experiment performed during the Apollo 11 mission showed the He^4 component of the solar wind to have a flux of $6.3 \pm 1.2 \times 10^6$ particles cm^{-2} sec^{-1}. (F. Bühler, P. Eberhardt, J. Geiss, J. Meister, and P. Signer, Science 166, 1502 (1969).)

values were obtained under an assumption of a radial solar wind velocity. Vela 2A and 2B (Ref. II-9) measurements of the flow direction of the solar plasma indicated a mean flow about 1-1/2° east of the Earth-Sun line.

An example of the change in flux that occurs is taken from the plasma shock that resulted from the class 3B flare of 13 February 1967 (Ref. II-7). The proton flux changed from a preshock wave value of 2.0×10^8 cm^{-2} sec^{-1} to a post shock wave value of 5.8×10^8 cm^{-2} sec^{-1}. At the maximum, the flux was 8.3×10^8 cm^{-2} sec^{-1}. These increases were associated with an increase in the proton energy from 385 eV to 770 eV to 1920 eV, respectively.

D. SOLAR WIND ELECTRONS

Observations of the properties of the electrons in the solar wind are difficult because of the fact that the average energy of the electrons is low. The low energy of the electrons means that the spacecraft potential can perturb the measurement and that solar light formed photoelectrons can cause erroneous measurements.

The most accurate measurements are the recent ones obtained with the Vela 4B satellites (Ref. II-10). The electron properties were measured with an electrostatic analyzer which had 20 continuous energy intervals (channels). The results, which are presented in Fig. II-3, show that the electron energy spectrum has a broad maximum in the energy range of 20 to 40 eV. The electron distribution function shows a Maxwellian distribution for those with velocities less than about 5000 km sec^{-1} (or energy less than 140 V) and a high energy tail (at higher velocities) that has a different distribution. The measurements of the electron bulk speed and density agreed with measurements of the positive ion bulk speed and density, thus indicating the validity of these measurements of the electron properties.

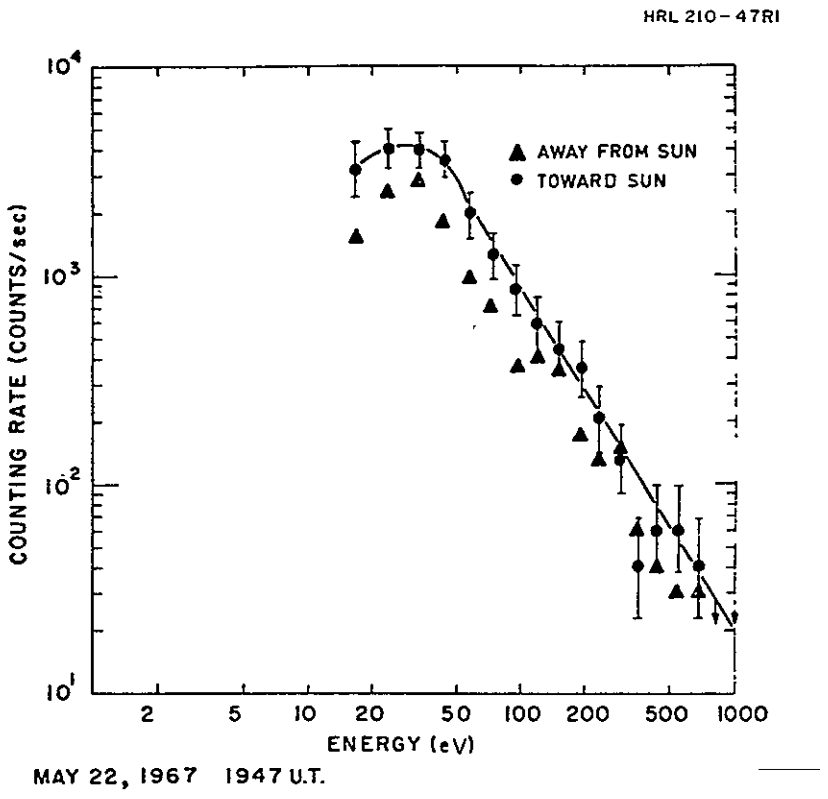

Fig. II-3. Electron-energy spectrum measured on the Vela 4 spacecraft (Ref. II-10).

SECTION III

SOLAR WIND SIMULATOR REQUIREMENTS

The design analysis for the optimized solar wind simulator must have as a foundation a set of requirements that are based on the characteristics of the solar wind (summarized in Section II), and on the limitations imposed by the laboratory environment. The following specifications, presented in RFP A-15122 (FG-5), are typical of those generally used. The simulator would have a 99% pure proton beam of 10 cm diameter at the target plane with a ±5% uniformity. The proton energy should be controllable at any point from 0.5 to 3.0 keV with less than a 10% spread. The proton flux should range from 2×10^{8} to 2×10^{11} cm^{-2} sec^{-1} at the sample for the total energy range. The system should be capable of continuous operation for 1000 hours. It should operate with a chamber pressure of 5×10^{-7} Torr or less, with a sample temperature controllable over the range of 100 to 450°K, and with simultaneous solar ultraviolet radiation (vacuum and near ultraviolet), protons and electrons of 10 to 100 eV energy and flux range of 1×10^{8} to 1×10^{12} cm^{-2} sec^{-1} at the sample plane.

A detailed analysis of these and other physical characteristics of the solar wind simulator is presented in Section III-A. In addition, a theoretical analysis of problems such as the neutralization of the ion beam charges, ion-atom charge exchange, and ion solid reactions such as sputtering is presented in Section III-B.

A. PHYSICAL CHARACTERISTICS OF THE SOLAR WIND SIMULATOR

The objective of this subsection is to establish the conditions for the laboratory simulation of the solar wind. The analysis of the particulate environment of space (Section II) is used as a basis for this discussion. Additional factors such as the duration of the tests, the cost and complexity of the equipment, and the problems of accelerated testing are also considered. The discussion involves establishing the ion composition, flux and energy spectrum, electron flux and energy spectrum.

1. Positive Ion Composition

All efforts to date to simulate the solar wind have used either proton beams that were purified by mass separation or mixed (unpurified) proton-molecular ion (H_2^+) beams. Simulation in this manner was justified by the fact that the solar wind is predominantly composed of protons. This element of the report will analyze the factors which determine the ion composition necessary for simulation of the solar wind.

The average composition of the solar wind during quiet sun conditions is about 95% H^+, 4% He^{2+}, and less than 0.5% total heavy ions. The heavy ions can be distinguished only under quiet sun conditions. The n_α/n_p ratio (the number of He^{2+} to the number of H^+) varies from less than 1% to more than 15%. The higher values are associated with solar activity. The implication is that the solar plasma composition changes with solar activity and that the heavy ion concentration can be larger during solar flares.

The degree of simulation of the solar wind can be divided into three categories:

(1) first order simulation, which uses only protons
(2) second order simulation, which uses both protons and alphas in about a 95:4 number ratio
(3) third order simulation with protons, alphas, and highly charged heavy ions (such as O^{7+}, O^{6+}, O^{5+}, etc.) in about a 95:4:1 number ratio.

The significance of these three levels of simulation is presented in the following discussion.

A third order simulation of the solar wind involves the use of three different ion sources, and thus is extremely complex. In particular, the production of highly charged species, such as O^{6+}, with energies ranging from 10 to 50 keV is a difficult problem and is prohibitively expensive. In the event that the effects of the heavy ion component (such as sputtering, chemical reactivity, and energetic x-ray photons and Auger electrons produced by the interaction of the ions and the surface) are significant, an alternative technique could be used which involves an O^{+} ion source to simulate the heavy ion mass and chemical effects, and a low energy x-ray source to simulate the x-ray and Auger electron effects.

Second order simulation with both H^{+} and He^{2+} ion sources does not appear particularly useful when compared with a first order simulation. The alpha particles do not react chemically with the target. The sputter yield of the alphas is not significantly greater than that of the protons. The x-rays and Auger electrons resulting from the neutralization of the 25 and 54 eV first and second ionization potentials may be significant. It should be possible to duplicate the He^{2+} effects with protons and thus avoid the increased costs and complexity of a dual source system.

Based on the present information concerning radiation effects of the solar wind on the thermal control materials, a first order simulation with only protons is an adequate degree of simulation. In addition, the development of an optimized proton simulator, which is the goal of this program, has yet to be completed; realistic tests must be run and evaluated before second and third order effects can be considered. In some cases, modification of the proton dose (flux and energy) may serve to simulate some of the second and third order effects. Thus it is concluded that a simulated solar wind should consist only of protons.

2. Ion Flux

The simulation of the solar wind requires an ion flux of 2×10^{8} cm^{-2} sec^{-1}, which corresponds to a proton current density of 3×10^{-11} A cm^{-2}. This value is based on the Mariner 2 data which were obtained during a period of declining solar activity and the Vela series which operated during a period of minimum solar activity. It may be necessary to modify this value when measurements are made during the next period of maximum solar activity. Based on the flux changes observed during a flare and the differences between the Mariner and the Vela values, it is estimated that the change in value will be no more than a factor of three.

Accelerated testing of the thermal control coatings may be necessary in order to shorten the laboratory testing period. This is particularly true when radiation resistant coatings have been developed. At present, accelerated testing is performed with 5 to 50 equivalent suns of photon radiation. The limitation is the limited output of the light sources and the problem of reciprocity failure of the samples.

A goal of this study was to design a simulator capable of operating at proton flux levels up to 2×10^{11} cm^{-2} sec^{-1}, which would make possible testing at levels up to 1000 times the normal solar plasma flux. This is an acceptable design goal as far as the ion physics or engineering aspects are concerned. It is important to note that the operating limit may be less than 1000 times the solar plasma flux because of reciprocity failure in the sample. This is determined by an analysis of the dose versus damage curve for the specific material.

The flux level may be greater if a scanned beam is used to irradiate the sample. In this technique, an intense beam of small area is swept over the sample surface in much the same way as an electron beam is used to form a television image. The advantage of this method is that it makes possible a very uniform irradiation of the total sample area and that it makes the control of the flux level easier. The two major conditions associated with the raster technique are that the local increase in beam intensity must not be large enough to result in reciprocity failure and that the lifetime of the proton induced radiation damage must be such that there is no difference in the damage that results from the scanned beam and that which results from a continuous beam. An analysis of the latter condition is presented in Appendix A of this report. The conclusion of this analysis which is based on a thermal spike model of radiation damage, is that the damage (i.e., color center density) is established by the defect density which is a function of the dose. There is no significant difference between the continuous and the rastered irradiation of the samples. In addition, the bleaching time is large enough that the raster rate will not be a significant factor.

3. Proton Energy

The energy of the solar wind protons varies with the solar activity. As summarized in Section II-B, the proton energies range from the quiet sun condition with 500 eV protons to the flare conditions when the protons can have 3 keV energy. There is always sufficient solar activity that even during the period of minimum solar activity the mean energy of the protons is about 1 keV.

4. Electron Flux and Energy

The most direct way of specifying the electron emission capability of the neutralizer is to state that it be capable of providing sufficient electron current to neutralize the proton beam charge at any proton beam operating level. Based on the observations of the solar wind electron energy, the neutralizer should produce electrons of about 20 to 40 eV energy.

5. Beam Purity

It is desirable to have a proton beam of the highest practical purity. However, limiting the impurity ions to a particular concentration does not insure that the physical effects of the impurities will be small compared with that of the protons. An example is that of sputtering, which is discussed in Section III-B-3. The sputter yield for heavy ions is about 100 times that of protons, so that the sputtering effect of a 1% heavy ion impurity would be equivalent to the 99% of the beam that is protons.

A solution to this problem is to set a dual impurity specification which permits up to 1% of H_2^+ in the beam, and a maximum of 10^{-3}% of all other heavy ions. The molecular

hydrogen ion (H_2^+), which is the major impurity, has chemical and physical effects that are quite similar to those produced by the protons. Therefore, the effect of the molecular ion should scale approximately as does its concentration in the proton beam.

There are two sources of gas that are responsible for the heavy ion impurity: (1) the impurities that are present in the hydrogen gas supply; (2) the gases that are desorbed from the surfaces of the ion source and from the walls of the vacuum chamber. The amount of adsorbed gas can be controlled in two ways. The first is to remove it by pumping. This can be accelerated by "baking out" the vacuum system (i.e., heating the system to about 250 to 350°C). The second way is to operate the source for a period of a few hours (Ref. III-1) prior to the actual run. The presence of heat and ions from the plasma will clean the surfaces of the system. The control of the impurities in the hydrogen gas supply requires the use of the research grade of hydrogen which has a purity of 99.9995% minimum (Ref. III-2).

Another aspect of beam purity not specified is the presence of energetic neutrals formed by charge exchange (see Section III-B-2). As the fast neutrals will have the same mass effects on the surface as do ions, and because they are not registered as a current and are therefore not included in the dose measurements, it is essential that the number of charge exchange neutrals not exceed 1% of the proton flux. This factor is also discussed in Section IV-B, as it is an important element in the selection of the mass separator system.

The beam purity requirement should also specify a limit for energetic photons (Lyman α radiation) which are produced in the ion source. An estimate of the magnitude of the photon production in an rf ion source is presented in Appendix B.

These photons, which are due to the excitation of hydrogen atoms and molecules by electron bombardment, have energies of about 10 eV. They can cause a very marked effect in the degradation of thermal control coatings (Ref. III-3). The production of photons is negligible in the low pressure electron bombardment ion sources and pronounced in the plasma type ion sources. This factor is considered in the selection of the ion source in Section IV-A and in the selection of the mass separator in Section IV-B.

6. Vacuum Requirement

The vacuum requirement for this type of test has typically required the solar wind simulator to operate with a sample chamber pressure of 5×10^{-7} Torr or less. It is useful to augment this specification by defining the operating conditions in terms of the partial pressures of the residual gases that are present. This is important because some gases are known to cause bleaching of some of the color centers formed in the degradation of the thermal control coatings. The tolerance limits for these gases must be set to insure that they will not interfere with the experiments.

Duplication of the vacuum conditions that exist in the interplanetary space (i.e., a random gas with a pressure of the order of 10^{-13} Torr and a directed pressure of the order of 10^{-11} Torr due to streaming from the sun (Ref. III-4) is unrealistically expensive. This is discussed in greater detail in Section V-E. However, because there is evidence of a significant difference between the results of simulation experiments performed at 10^{-6} Torr and with coatings that have operated in the space environment, it will be necessary to determine experimentally the reasonable limits for the partial pressure of gases such as oxygen. Experiments have been performed (Ref. III-5) which show marked changes in reflectivity at 10^{-5} Torr partial pressure of oxygen, indicating the need for further research.

An approximation of the arrival rate of oxygen gas for the estimated conditions to be found in space and in the laboratory vacuum system indicates the magnitude of the difference between the two environments. If the laboratory vacuum oxygen partial pressure is estimated to be 1×10^{-7} Torr and its temperature to be 300°K, the molecular arrival rate at a surface ν is given as follows (Ref. III-6):

$$\nu = 3.513 \times 10^{22} \frac{P_{Torr}}{(MT)^{1/2}} \text{ cm}^{-2} \text{ sec}^{-1}$$

where

$M \equiv$ molecular weight
$T \equiv$ gas temperature °K
$P_{Torr} \equiv$ gas pressure.

Thus the arrival rate of oxygen is

$$\nu \simeq 3.5 \times 10^{22} \times 10^{-7}/(32 \times 300)^{1/2}$$
$$\simeq 3.6 \times 10^{13} \text{ molecules cm}^{-2} \text{ sec}^{-1}.$$

If we estimate that the number of lattice sites on a surface is about 4×10^{14}, under these conditions the oxygen molecules will arrive at the rate of a monolayer in 10 sec.

If we estimate that the oxygen gas content in space is about 10% of the total, it would have a partial pressure of about 10^{-14} Torr. The black body temperature of space is about 4°K and the gases are dissociated so that the oxygen atomic weight is 16. The arrival rate is

$$\simeq 3.5 \times 10^{22} \times 10^{-14}/(16 \times 4)^{1/2}$$
$$\simeq 4.4 \times 10^{7} \text{ atoms cm}^{-2} \text{ sec}^{-1}$$

Under these conditions, therefore, a period of about three years is necessary for a monolayer of oxygen to arrive at the surface.

The significance of this estimate is that it will be necessary to perform experiments on the irradiation of identical samples under a range of vacuum conditions to determine if the experiments are sensitive to the presence of specific gases. This is a standard procedure when operating an experiment in the presence of additional factors that can influence the results.

The vacuum conditions also may be set by the presence of sensitive elements of the simulator system. For example, the predominant gas in a typical unbaked system is water vapor, which is evolved from its adsorbed state on the surfaces within the system. There is a high probability that this will occur in the simulator system due to the very high surface-to-volume ratio of both the reflective white coating in the integrating sphere and the samples of the thermal control coatings. These surfaces can act as a significant water vapor reservoir. If impregnated cathodes are used in the ion source, the neutralizer source, the mass analyzer, or the pressure sensor, it is possible for the water vapor to "poison" the cathode surface.

Because of the uncertainties in the estimation of residual gas effects on the experiments, the a priori establishment of partial pressure limits is not possible. Instead, it is necessary to set up guidelines which will result in the design of a system that has the capability to operate at pressures below the 5×10^{-7} Torr level. This will permit the establishment of these basic partial pressure parameters. In view of the fact that hydrogen will be the major gas present (due to the operation of the proton

source), it is possible to set the total operating pressure limit at 5×10^{-7} Torr and to set, as a design goal, the limit on the total of all other gases as about 1×10^{-8} Torr.

Shrouds to Trap Radiation

In addition to the requirements for the system operating pressure, it is necessary to duplicate the condition that exists in space where none of the radiation from the surface and none of the gas desorbed by the surface is returned to the surface. The 3°K black body conditions of space can be simulated by placing a cryogenically cooled shroud whose surface has been treated to give it a 95% absorptivity. The shroud will prevent radiation that is either emitted or reflected by the surface from being reflected back to any of the samples. In addition, for a sample at 300°K and a shroud at 100°K, the net radiated power from the sample is about 99% of that when the 300°K sample is exposed to the 3°K black body of space. The cryogenic nature of the baffle will serve to trap most of the gases (except hydrogen) that are desorbed from the sample surfaces.

8. Proton Beam Diameter

The specification of a proton beam diameter of 10 cm at the sample plane (with a ±5% uniformity), is needed to expose simultaneously about eight samples of 2 cm diameter size. The 10 cm diameter represents an upper limit to the size to which a single ion beam can be expanded. The design of a system to expose larger sample areas will involve a scanned ion beam. The present system should have both the capability of a broad continuous ion beam and of a small scanned ion beam.

9. System Operating Lifetime

The continuous operating lifetime of 1000 hours is necessary to prevent the nullifying of extended testing due to the failure of the system. If a run were stopped and the samples were pressurized to 1 atmosphere to allow the repair of the system, the effect of the irradiation would be lost due to the possibility of bleaching of the color centers. As a result, the requirement for a 1000 hour lifetime has been placed on the system.

There is an alternative system in which the proton beam-forming apparatus and the sample chamber are each provided with the complete vacuum pumping facility and can be isolated from each other by a gate valve. This system has the advantage that one component can be modified or repaired without affecting the vacuum condition in the other component. This system also makes possible the differential pumping of the ion source, which minimizes the gas load to the sample chamber and thus makes it easier to obtain lower pressures in the sample chamber.

B. INTERACTION OF THE PROTON BEAM WITH OTHER MATERIALS

This subsection is concerned with the interaction of the proton beam and the other constituents in the system. A principal one is the interaction of the proton and electron beams to produce a neutralized beam at the sample surface. This is of critical importance for dielectric samples such as the thermal control coating materials. Another type of interaction is that of charge transfer between the protons and the neutral atoms and molecules. The third type is the ion-solid interactions which consist of sputtering, lattice displacements, and tunneling, among others.

1. Neutralization of the Proton Beam Charge

A critical aspect of experiments involving proton irradiation of samples of dielectric materials used in thermal control coatings is to maintain the sample surface in an essentially neutral electrical condition. If the electron source is inadequate to neutralize the proton beam charge, the sample surface can develop a positive potential whose magnitude depends on the dielectric strength and electrical resistance of the sample, on the proton energy, and on the presence of secondary and thermionic electrons.

The failure to neutralize the proton beam charge by means of low energy electrons can affect the experiments in a number of ways. The formation of a surface potential can cause a decrease in the kinetic energy of the protons that strike the surface, and can affect the ion trajectories and produce a nonuniform irradiation. The potential will cause an increase in the energy of the electrons that strike the surface. Neutralization by means of breakdown can occur. The mechanisms can include the formation of conduction paths, collisional ionization, and discharge phenomena (including field emission and ionic conductivity).

The need to neutralize the proton beam stems from the nature of the system. Protons (as well as any other ions) are formed in sources described in Section IV-A of this report. They are accelerated from the source and travel through the vacuum to impinge on the samples, the sample holder, and the vacuum chamber wall. This is shown in schematic form in Fig. III-1. As the positive ions are immobilized at the impact site, it is necessary to have an equivalent flow of negative charge (in the form of electrons) from the source to the impact sites, in order to maintain the electrical neutrality of the system and thus the continued operation of the system.

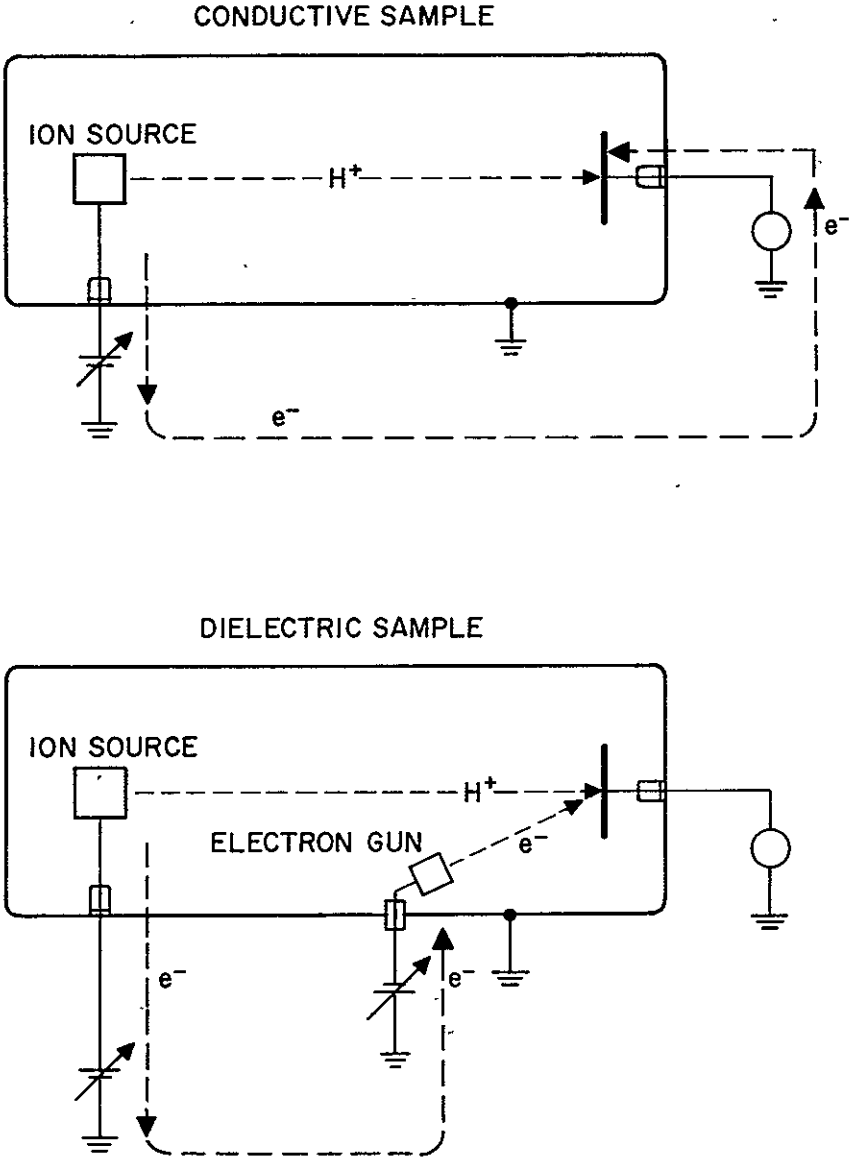

Fig. III-1. Schematic view of proton and electron flow in systems with metallic and dielectric targets.

In general, this supply of neutralizing electrons can flow through the power supply, which provides the bias to the ion source, through the external circuit to the impact sites. In the case of nonconductive dielectric materials, the electrons are stopped at the metal-dielectric interface and ions on the vacuum surface of the dielectric to form a capacitor. This capacitor would continue to charge until the field is great enough to cause an electrical breakdown of the insulator or until the surface potential becomes equal to the ion potential, causing the ion beam to be deflected to other surfaces.

Neutralization of the surface charge on a dielectric target may be accomplished by means of a thermionic electron source in the manner shown in Fig. III-1. The electrons are emitted from the filament and accelerated from the source; they travel across the vacuum to the sample surface, thus neutralizing the proton charge.

An important condition imposed on the neutralizer source is that the electron energy be limited to the order of 20 to 40 eV. This is necessary in order to simulate the energy of electrons present in the solar wind and to ascertain that the electron energy is not large enough to cause ionization in the sample.

The problem of charging of the sample surface can be observed only in samples having a high resistivity and a high dielectric strength. For example, alumina (Al_2O_3) has a room temperature resistivity of about 10^{15} Ω-cm^{-1} and a breakdown voltage of about 10^5 V cm^{-1}. Let us consider a 0.1 cm (0.040 mil) thick sample of Al_2O_3 that is exposed to a 1 keV proton beam with a 10^{-8} A cm^{-2} current density.

The resistance of the sample (per square centimeters of area) is 10^{15} Ω-cm^{-1} x 10^{-1} cm = 10^{14} Ω. The leakage current for a 10^{3}V potential across the sample is (I = (V/R)) = 10^{-9} A. As this quantity is smaller than the proton arrival rate, the surface ~~should~~ will rapidly charge up to a 10^{3} V potential In addition, the breakdown voltage of the 10^{-1} cm thick sample is 10^{5} V cm^{-1}x10^{-1} cm = 10^{4} V, which exceeds the beam potential. cont

In a second example, a zirconia sample of the same dimensions would exhibit a different behavior. Zirconia has a room temperature resistivity of about 10^{8} Ω-cm^{-1}, so that the resistance of the sample would be 10^{7} Ω. A leakage current of 10^{-8} A would occur at a voltage of 10^{-1} V. Thus, the zirconia sample would not develop a surface potential because of the conductivity of the sample.

Similar problems exist in the comparison of samples of a pigment in various binders. The higher conductivity of the thermal control coatings using a potassium silicate binder, compared with the coatings which use silicone resins, can result in different experimental conditions.

The failure to neutralize the proton charge during the irradiation of high resistivity-high dielectric strength samples (such as thick anodized metal surfaces) can result in mechanical damage due to breakdown. One possible mode is discharge breakdown. In Fig. III-2(a), the electronic states of an insulator and a metal are shown before irradiation by the proton beam. After the accumulation of positive charge on the surface of the dielectric, the potential energy is shown in Fig. III-2(b). Electron conduction can result from tunneling through the barrier, from a decrease in the barrier potential (Schottky emission), or from field emission which is associated with the depression of the barrier to near the Fermi level of the metal.

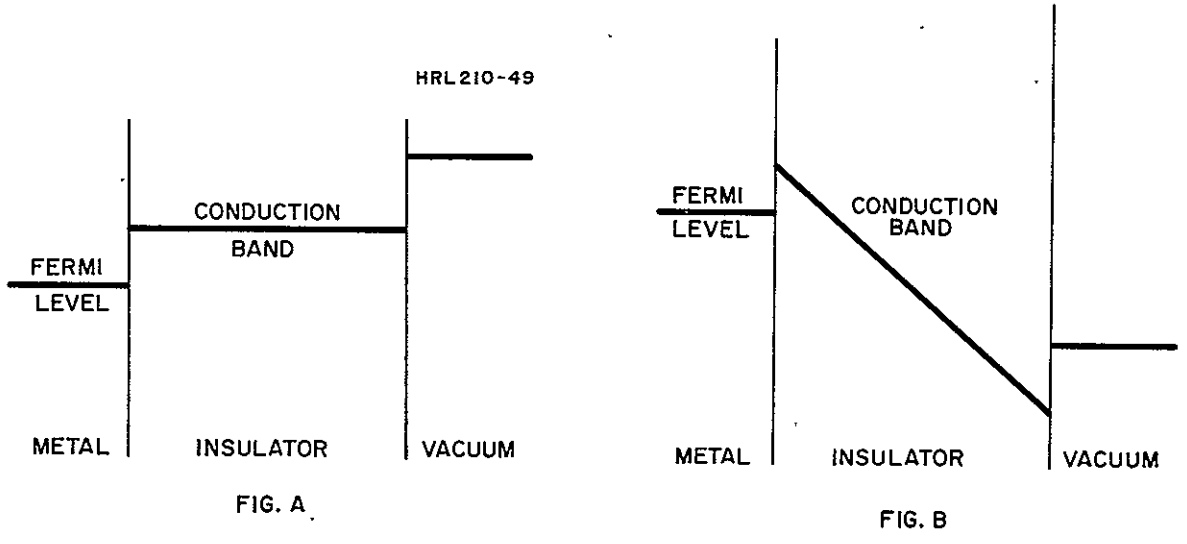

Fig. III-2. Electronic levels in a neutral and in a positively biased dielectric target.

Breakdown also can result from collisional ionization (avalanche breakdown), and from the formation of conductive paths by metal ion migration and by ionic conductivity.

In summary, it is necessary to provide a neutralizer to supply electrons in sufficient numbers to offset the positive charge due to the energetic protons. The electron energy should be about 20 to 40 eV to duplicate the electrons in the solar wind. Instrumentation (which will be

described in Section V-D-2) is necessary to separate the ion and electron currents to be able to regulate these two sources during the operation of the solar wind simulator.

2. Charge Transfer

Charge exchange is one of a number of gas phase reactions involving the collision of an ion and a neutral atom or molecule. In this process, which is shown in (III-1), an electron can transfer from the neutral particle to the ion during the brief period when they are in close proximity.

$$M^+ + N \rightleftarrows (MN)^+ \rightarrow M + N^+ \quad . \qquad \text{(III-1)}$$

The process involves an inelastic collision (i.e., there is no momentum transfer), and thus the two particles retain their original kinetic energy. This fact is of considerable importance in the design of a solar wind simulator because it means that energetic protons will charge exchange to form energetic neutrals. This is in contrast to other inelastic collision processes (see Table III-1) which do not produce energetic neutrals.

TABLE I

Inelastic Collision Processes

(1) $M^+ + N \rightarrow M^+ + N^*$	excitation
(2) $M^+ + N \rightarrow M + N^+$	charge transfer
(3) $M^+ + N \rightarrow M^+ + N^+ +$ electron	ionization
(4) $M^+ + N \rightarrow M^{++} + N +$ electron	stripping

The fast neutrals present the following problem in the application of the solar wind simulator when the samples are located in line of sight with the ion source. The beam of fast neutrals will strike the sample surface and cause the same damage as do the protons, but the neutrals will not be recorded as an electrical current; this gives an erroneous value for the flux of particles that is responsible for the observed damage. An additional problem results from the anisotropic distribution of the fast neutrals. While the proton beam is expanded (about 100 diameters) and collimated by means of electrostatic or magnetic lenses to form a uniform beam over a 100 cm^2 target surface, the fast neutrals are unaffected by these devices and thus retain the trajectories that are established in the ion source exit aperture. As a consequence the fast neutral beam will be concentrated and produce a nonuniform irradiation of the samples. This also means that even if the magnitude of charge exchange is small, it still may have a pronounced effect on a specific area.

The basic expression for the attenuation of an ion beam due to charge transfer is given by

$$I_\ell = I_o \exp(-\sigma n \ell) \qquad \text{(III-2)}$$

where I_o is the ion current entering the region which contains a neutral particle density of n particles/cm^3, I_ℓ is the ion beam current at a distance ℓ cm, and σ is the reaction cross section in square centimeters.

The magnitude of the charge transfer cross section is dependent on the nature of the ion-neutral pair involved in the reaction. It is convenient to distinguish between the symmetric resonance charge transfer between like atoms $M^+ + M \rightarrow M + M^+$ and the asymmetric charge transfer between

unlike particles $M^+ + N \rightarrow M + N^+ + \Delta E$ where the energy defect ΔE is the effective energy difference between the initial and final states of this system. When all particles are in their ground state, ΔE is the difference in the ionization potentials of the neutral particles M and N. In general ΔE also includes terms for polarization and excitation.

In the symmetric resonance case, an example being the proton-hydrogen atom reaction, the cross section is largest at low ion velocities and decreases as ion velocity increases. The proton-hydrogen atom charge exchange has been measured by many investigators, of whom Fite (Ref. III-7) is the most recent. The proton-hydrogen atom charge exchange cross section is shown in Fig. III-3 (Ref. III-8).

HRL210-45

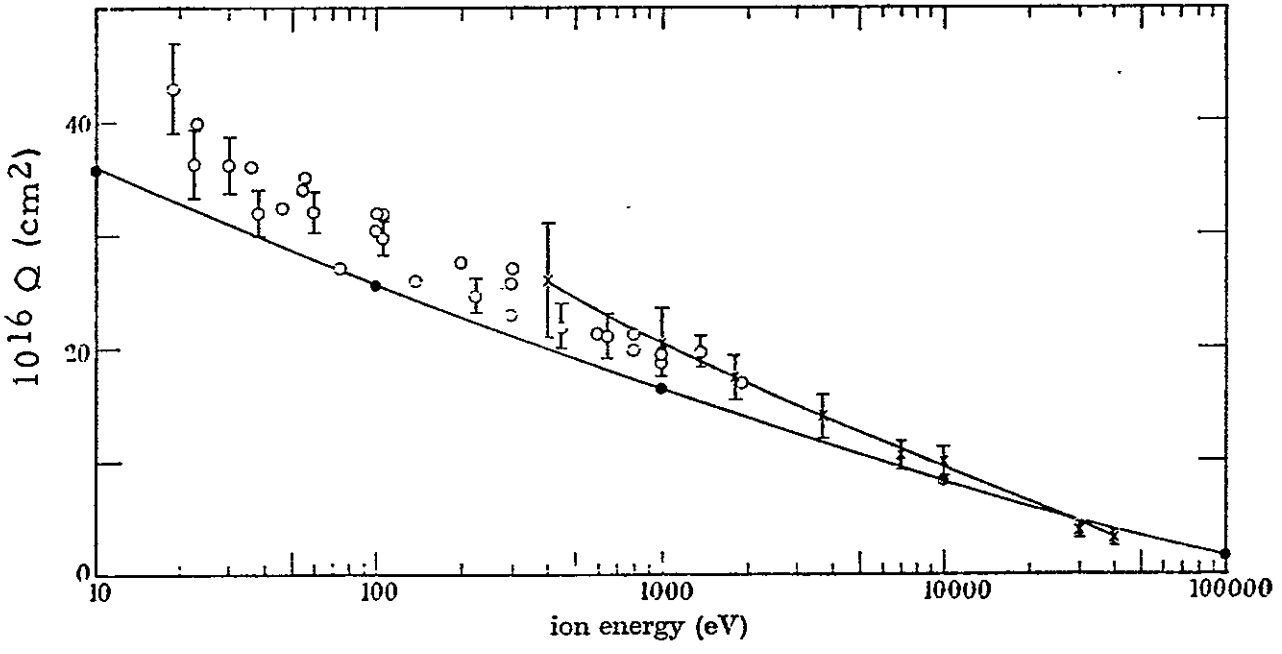

Fig. III-3. Cross sections for charge transfer between H^+ ions and atomic hydrogen. o, data from Ref. III-8; x, data from Ref. III-9; ●, data from Ref. III-10.

The cross section for the asymmetric case, an example of which is the proton-molecular hydrogen reaction, depends very strongly on the magnitude of the energy defect. This dependence has been treated by Massey (Ref. III-11) by means of a near-adiabatic hypothesis. It involves a characteristic collision time (a/v) where a is an interaction range of the order of 5 to 10 Å and v is the relative velocity of the ion and neutral particles. The electronic transaction time is $h/\Delta E$. The asymmetric charge transfer should have a maximum value when $(a\Delta E/vh) \simeq 1$, where the relative velocity of the particles is comparable to the velocity of the electrons involved in the transfer. This is shown in Figs. III-4 and III-5 for the H^+-H_2 charge transfer reaction (Refs. III-12, III-13).

In view of the fact that the presence of charge exchange neutrals would be detrimental in the proposed experiments and that the measurement of the magnitude of this flux would require a very elaborate technique, the design of a solar wind simulator should be such as to prevent the arrival of fast neutrals. It is significant that this design is also necessary to prevent the energetic photons (which are formed in the hydrogen discharge) from irradiating the samples. It is possible to estimate the magnitude of the charge exchange in a typical source and thus show the importance of the proposed design.

In order to estimate the charge exchange, it is necessary to specify or estimate the operating parameters of the source. These include the temperature and pressure of gas inside the ion source, the geometry of the exit orifice of the source, the atomic to molecular ion (H^+/H_2^+) ratio, and the ion energy. A calculation will be carried out for a generalized case in sufficient detail to make it applicable to any specific source.

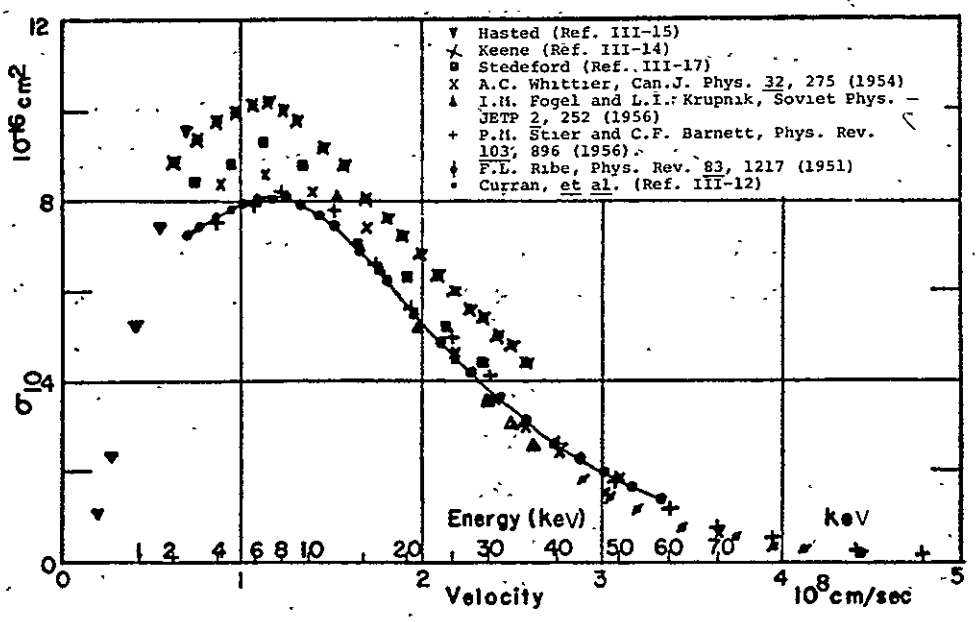

Fig. III-4. Measurements of electron capture cross sections σ_{10} for protons in H_2 (Ref. III-12).

HRL 210-44

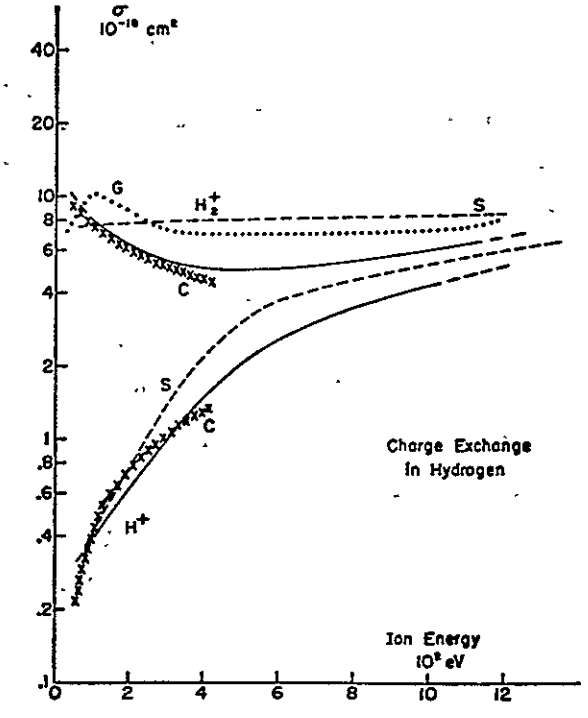

Fig. III-5.
Charge-exchange cross sections for H^+ and H_2^+ in hydrogen (Ref. III-13). Solid curve, present work; S, Stedeford and Hasted (Ref. III-17); G, Gilbody and Hasted (Ref. III-18); C, Cramer (Ref. III-19).

A typical rf ion source operates with a hydrogen gas pressure of about 35 μm (3.5×10^{-2} Torr). The temperature of the gas is estimated to be about 500°K. The source exit geometry is taken from a widely used commercial source. The diameter of the exit canal is 1.5 mm and its length is 12.7 mm. The extent of dissociation of the molecular hydrogen gas into atomic hydrogen is estimated to be about 90%, based on the ratio of molecular and atomic ions produced in this type of source and on the ionization cross section for this process. The last parameter to be established is the ion energy, which in turn establishes the magnitude of the charge exchange cross section. For this calculation we will use a value of 1.0 keV for the energy, which sets the charge transfer cross section at 21×10^{-16} cm^2 (see Fig. III-3).

Based on the kinetic theory of gases, the number density of hydrogen atoms per cubic centimeters (for a gas in a closed system so that the atoms have a random direction) is given by (Ref. III-6)

$$n = 10^{19} \frac{P}{T}$$

where P is the hydrogen pressure in Torr and T is the gas temperature in degrees Kelvin. For gas having a directed flow the number density is given by (Ref. III-6)

$$n = 2.4 \times 10^{19} \frac{P}{T}$$

The variation in gas density in the channel is approximated as being inversely proportional to the distance down the channel. This assumes that the density goes to zero at the end of the channel. This means the average density in the channel is $(n/2)$. This is a very rough approximation, but

it is adequate for this calculation. The source produces about 600 mA of protons, which represents a particle flux of 10^{13} ion/sec. This is about 3% of the gas which leaves the source.

The estimate of the decrease in the photon flux due to charge transfer is given by the following modification of (III-2):

$$\log (I_o/I) = \frac{1}{2.3} n_H \sigma \ell$$

where n_H, the number density of the atomic hydrogen gas, is given by the following quantity which includes corrections for the extent of dissociation and the proton beam:

$$n_H \quad \left[\left(\frac{1}{2}\right)\left(0.9 \times 10^{19} \frac{P}{T}\right) - 10^{13}\right]$$

$$= \left[\left(\frac{1}{2} \times 0.9 \times 10^{19} \times \frac{3.5 \times 10^{-2}}{500}\right) - 10^{13}\right]$$

$$= 3.05 \times 10^{14} .$$

The extent of charge transfer of the proton beam is as follows:

$$\log (I_o/I) = \frac{1}{2.3} (3.05 \times 10^{14})(21 \times 10^{-16})(1.27)$$

Therefore,

$$I/I_o = 0.443.$$

This means that about half of the proton beam is converted to fast neutrals in the 1.27 cm long exit channel.

This calculation demonstrates that charge exchange will be significant in the ion source exit channel. Although the magnitude depends on the estimates of the source operating parameters, it is sufficient to require that the bending of the proton beam axis purify the beam of the fast neutrals.

3. Ion Interaction with the Solid

The task of estimating the effects of the bombardment of the thermal control coatings by the solar plasma ions is very difficult because of the large number of variables involved in the process. The velocity (and thus the energy) of the ions in the solar wind, the flux of particles in the solar plasma, and the ratio of the different species in the plasma all vary with the solar activity. The purpose of this section is to summarize some of the interactions between the ions and solids, so that any reaction that is directly associated with or dependent on a specific ion energy, ion flux, or the ion itself may be noted. These factors could influence the design of the optimized solar wind simulator.

The most important effect of the solar wind irradiation of the thermal control coatings is the formation of color centers that cause a degradation of the optical properties of the coatings; in turn, this causes degradation of the desired thermal control properties of the surfaces. The mechanism for the degradation involves the ion bombardment of the pigment particles to cause both the displacement of atoms by nuclear elastic collsions, creating lattice vacancies or Frankel defects, and the formation of hole-electron pairs by ionization. The combination of these processes with the migration of the electrons to the lattice vacancies results in the formation of the color centers.

The task of estimating the extent of color center formation due to the solar wind bombardment is very difficult because of the number of variables involved. These include the ion energy, flux, mass, and degree of ionization. For example, the concentration of highly charged oxygen ions O^{7+} O^{6+}, and O^{5+} most likely increases during solar flares, as does the He^{2+} concentration. This concentration could be significant in lattice displacement effects and perhaps in ionization effects. The energy transfer factor,

$$\frac{4M_1 M_2}{(M_1 + M_2)^2} E_1$$

where E_1 is the energy of the incident particle of mass M_1, and M_2 is the mass of the lattice atoms, shows that 14 keV oxygen ions impact about 90 times as much energy to the oxygen in a thermal control coating as do 700 eV protons.

$$E(\text{transferred by oxygen}) = \frac{4 \times 16 \times 16}{(16 + 16)^2} 14 = 14.0$$

$$E(\text{transferred by } H^+) = \frac{4 \times 1 \times 16}{(1 + 16)^2} 0.7 = 0.155$$

This factor does not take into account the differences in the momentum transfer that occurs when the particles are sufficiently energetic to experience nuclear scattering. This is true of the high energy protons when they interact with low Z lattice ions.

The nature of the momentum transfer from the incident solar wind particles to the lattice atom varies as a function of the energy of the incident particle. Particles with high energy interact through the coulombic repulsion of the nuclear charges, which is termed Rutherford scattering. For

intermediate energies, the electron clouds partially screen the nuclear charges and thus the collisions are referred to as weak-screened coulomb collisions. At low energies the electron clouds are not penetrated and the collisions are of the hard sphere type.

For all ions, except the proton, the lower energy limits for Rutherford and weak-screened coulomb collisions are much greater than the ion energies associated with the solar wind. Kaminsky (Ref. III-20) gives the lower limit for Rutherford scattering as

$$E_B = 4\, E_R^2\, Z_1^2\, Z_2^2\, (Z_1^{2/3} + Z_2^{2/3})\, \frac{M_1}{M_2}\, \frac{1}{E_d} \quad .$$

where E_R is the Rydberg energy for hydrogen (13.68 eV); Z_1, Z_2, M_1, M_2 are the atomic numbers and masses of the incident particle and the target atom; E_d is the energy to displace an atom from the lattice site which ranges from 20 to 25 eV for many metals. The lower limit for the weak-screened collisions is given as

$$E_A = 2E_R\, Z_1\, Z_2\, (Z_1^{2/3} + Z_2^{2/3})\, \frac{M_1 + M_2}{M_2} \quad .$$

For silver and copper targets, these values were calculated by Kaminsky and given in Table III-2.

Another factor is the energy loss mechanism. The dominant mode of energy loss for fast ions in a solid is by inelastic collisions which excite the electrons of the lattice atoms. This mode of energy loss is much greater than any other mode when the ion energy E is greater than a limiting energy E_c, and it is negligible when $E < E_c$. The limiting energy E_c for protons can be approximated by

$$E_c = \frac{1}{16}\, \frac{M_1}{M_e}\, W_i \simeq 10^2\, W_i$$

where M_e is the electron mass and W_i the Fermi energy of free electrons in the solid. Thus, for protons the limiting energy is of the order of 0.5 to 1 keV for various solids. Under conditions of a quiet sun, most of the proton energy would be given up to the lattice as thermal energy. Under periods of solar activity, the energy of the ions would be higher and thus would result in a modified energy decay mode. In this case, the initial energy loss would be by means of an electron excitation mode. As the proton energy decreased, the energy loss would be due to nuclear elastic collisions which cause the lattice displacements.

TABLE III-2

Energy Limits for Weak-Screened and Rutherford Scattering

Ion	Silver target Z = 47 M = 107.9		Copper target Z = 29 M = 63.5	
	E_A keV	E_B keV	E_A keV	E_B keV
H^+	4.8	10.2	2.6	4.1
He^+	10.1	160	5.6	69.1
O^+	48.5	12.58×10^3	29.0	5.39×10^3

An equivalent factor present in the flux of highly charged ions (O^{7+}, O^{6+}, and O^{5+}) is the production of x-ray photons or Auger electrons resulting from the neutralization of these ions at the surface of the target. Both the photons and electrons could cause other ionizations in the lattice.

In addition to the formation of color centers, bombardment by the solar wind will cause sputtering of the surface. Sputtering is the term applied to the process of removal of material from the surface as a result of ion bombardment of the surface. The kinetic energy of the ion is distributed rapidly to the neighboring atoms, with the result that some of the surface atoms will acquire enough energy to break the chemical bonds and evaporate from the surface. The evaporated material includes neutral atoms, ions, and electrons. The loss of ions and electrons is often treated individually and referred to as secondary ion and secondary electron emission resulting from ion bombardment.

The magnitude of sputtering is dependent on the ion mass and energy and on the nature of the structure of the target. There is a threshold energy of about 20 to 50 eV for the onset of sputtering. At low ion energies (of the order of 100 to 500 eV), the ion penetrates only a few atomic layers, and the yield is small but increases with increasing ion energy. The sputter yields are greatest for ions in the energy range of about 10^3 to 10^4 eV. Depending on the mass and energy of the incident ion and on the atomic mass and crystallographic structure of the target, the maximum yield can range from about 1 to 10 atoms/incident ion (for all ions excluding the hydrogen and helium ions). The yield then decreases at higher ion energies (above 10^4 eV) because the ion penetrates the surface to greater depths, thus decreasing the chance that surface atoms will acquire sufficient energy to evaporate from the surface.

The mass dependence of the sputter yield results from the mass dependence of energy or momentum transfer. The energy transfer factor $(4M_1M_2/(M_1 + M_2)^2)$ is greatest when

the mass of the incident particle. M_1 is equal to the mass of the target atom M_2. Experiments have shown that the sputter yield has this incident ion-target atom mass dependence.

There have been very few experimental measurements of the proton sputtering yield. The main reason appears to be that due to the very low mass of the ion; the yield is very small and therefore very difficult to measure. The conventional method of comparing the ion beam current and the mass loss by a target cannot be used with sufficient accuracy in the proton case because the mass loss of the target is obscured by the hydrogen uptake.

Grønlund and Moore extended the earlier work of O'Brian, Lindner, and Moore (Ref. III-21) and measured the sputter yields for 2 to 12 keV protons bombarding a silver target. They found the yield to be about 0.035 atoms/proton over a broad energy range; the results are shown in Fig. III-6. Yonts, Normand, and Harrison (Ref. III-22) observed a yield of 0.011 atoms of copper per 30 keV proton. Finfgeld (Ref. III-23) measured the yield for 0.5 to 8 keV protons on a gold target using a nuclear activation technique to measure the sputtered gold films. He observed a maximum yield of 0.014 atoms/proton at proton energies of 4 to 5 keV. These data are shown in Fig. III-7.

Although it is not valid to extrapolate from these data for protons on copper, silver, and gold, it is possible to estimate the magnitude of the sputtering of lower Z targets as being no larger than 0.1 atom/proton under the optimum conditions.

Using this estimate it is possible to estimate the material loss from the surface provided the magnitude of the heavy ion component in the solar wind is small enough to be

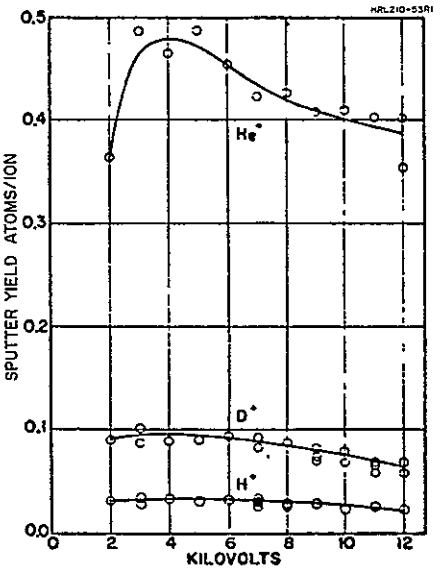

Fig. III-6.
Sputtering yield (atoms/ion) as a function of ionic energy for atomic ions normally incident on electroplated silver targets (from Ref. III-1).

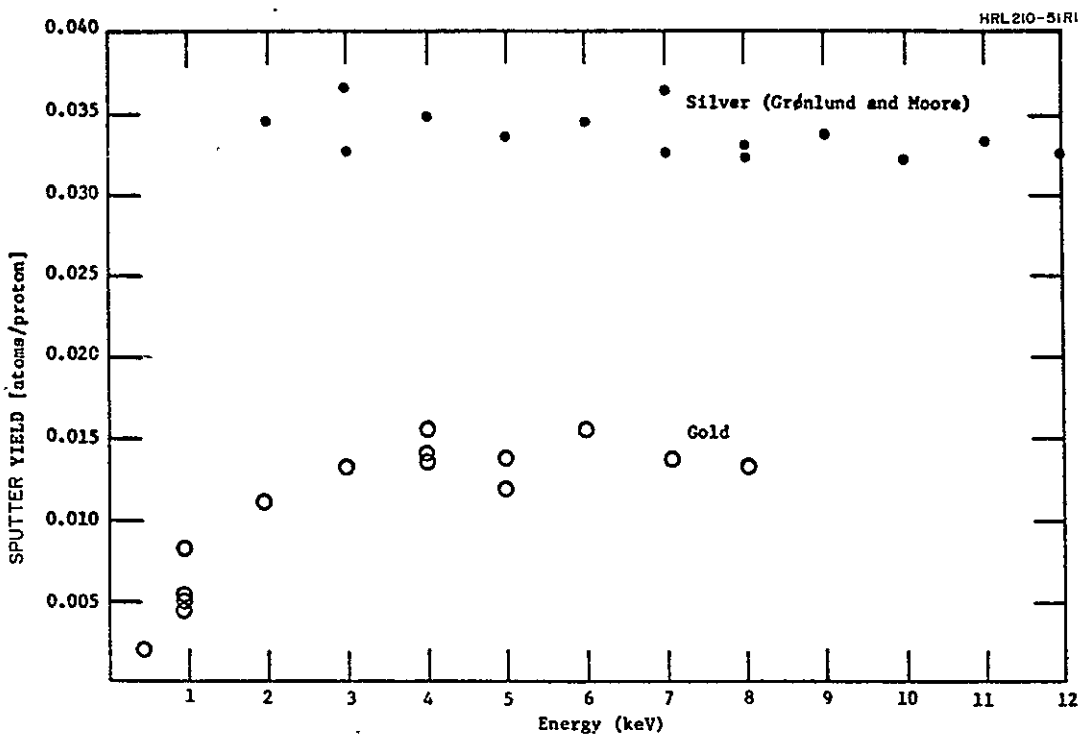

Fig. III-7. Yield versus proton energy for H^+ on silver and gold (from Ref. III-23).

neglected. This assumption will be discussed later. The normal proton flux of about 10^8 H^+ $cm^{-2}sec^{-1}$ would cause the loss of about 10^7 atoms $cm^{-2}sec^{-1}$, or about 3×10^{14} atoms $cm^{-2}yr^{-1}$. This means the loss of about a monolayer per year. This is a negligible quantity in terms of a material loss if we consider only the loss of the thermal control coating. However, if the argument presented by Gilligan and Zerlant (Ref. III-5) concerning the relationship between photodegradation mechanisms and the surface adsorbed states of oxygen is correct, this surface loss coupled with the very low partial pressure of oxygen in space could prove to be a significant factor in explaining the difference between laboratory and space degradation of the coatings.

The sputter yield of the heavy ion component would be dependent on the mass and energy. If one uses a worst case which involves approximating the sputter yield to be 10 atoms/ion based on the comparison made by Grønlund and Moore (Fig. III-8), the concentration of these ions would have to be 1% of the solar wind to produce the same effect as the protons. Because the heavy ion concentration is approximately 1%, this means their contribution has an effect equivalent to that of the protons.

Although sputtering may be considered to be negligible for operation in space, it can be a most serious problem in the laboratory simulation of these thermal control materials. These problems involve (1) the sputtering of metals from the other components onto the samples, (2) the sputtering of the dielectrics onto metal electrodes, and (3) the sputtering of charged particles (ions and electrons).

SECTION IV

COMPONENT COMPARISON AND SELECTION

A. ION SOURCES

Introduction

The characteristics of the ion source affect all the other major components of the system – the ion optics, the mass separator, and the vacuum station itself. Fortunately, for this study, proton sources have played an important role in nuclear physics for many years, so that a large body of information is available to define and compare the various possible source configurations. Before considering individual ion sources in detail, it is appropriate to interpret the previous section in terms of the conditions which it imposes on the ion source.

a. Total Ion Current

The proton flux in the solar wind is nominally 2×10^{8} particles cm^{-2} sec^{-1}. This is equivalent to 3×10^{-11} A cm^{-2}. In order to conduct accelerated tests, it may be desirable under some circumstances to operate the simulator at 10^{3} times the nominal solar intensity, or 3×10^{-8} A cm^{-2}. This requirement, coupled with the desire to irradiate an array of samples of 10 cm diameter, means that the total proton beam current at the target must range from 3×10^{-9} to 3×10^{-6} A. Depending on the exact system used, the attenuation of the proton beam as it passes through the apparatus may be of the order of a factor of three, thus making the total required proton current from the source approximately 10^{-5} A. The total output current from the source is

even higher because only part of the emergent ion beam is composed of protons. Perhaps the most important feature of this discussion is the fact that the proton current must be adjustable over three orders of magnitude; this is difficult to accomplish with some types of ion source.

b. Ion Energy

The bulk of the protons in the solar wind range in energy from 0.5 to 3.0 kV. In the simulator this is the voltage that is imposed between the source and the target (i.e., the net voltage through which the protons are accelerated). In order to provide the necessary experimental flexibility, the apparatus must be designed so that the proton energy is variable, at least over this range. While this is an added complexity that will be discussed in some detail in the section dealing with ion extraction from the source, it is well within the capability of the designer to make the instantaneous ion energy a variable. This should not be confused, however, with the virtually impossible task of providing an ion beam which contains a controllable mixture of all ion energies at a given time. Fortunately, the latter is not required for an accurate similation of solar wind.

A related characteristic is the energy spectrum of the ions inside the ion source. For reasons that will be made clear in the following sections, ion sources typically do not produce ions of a single discrete kinetic energy. Depending on the source, the energy spread may range from a few volts to several hundred electron volts. This energy spread appears as an uncertainty in the final proton energy at the target. While this may not be detrimental to the experiment itself, it does impose severe limitations on the design of the ion beam transport and separation systems. Therefore, an ion source with a small energy spread is desirable.

c. Mass Efficiency

Mass efficiency η_m is used to define the percentage of hydrogen atoms that actually leave the source as protons.

$$\eta_m = 100 \times \frac{\text{proton current}}{\text{ampere equivalent of hydrogen}}$$

where 1 cm^3 $hour^{-1}$ of hydrogen gas at STP = 2.5 equivalent mA of protons. A high mass efficiency is desirable to reduce the gas load from the ion source on the system and to reduce the neutral density in the region immediately downstream of the source. This reduces the creation of charge exchange ions which contaminate the beam (see Section III-B-2).

d. Source Lifetime

The useful lifetime of the source is important for an apparatus in which experimental simulation may be conducted in real time. The arbitrary, but realistic, lifetime goal set for this design was 1000 hours ($\sim$ 6 weeks). In some sources there is a reciprocal relationship between useful lifetime and ion current intensity. This is fortunate because in general an experiment conducted at an intensity of several equivalent suns will not run as long as a real time experiment.

e. Stability

Reasonable stability is required so that the experiment may run unattended for several weeks. In general, it is possible to stabilize any source by properly controlling the input hydrogen flow and the electrical parameters. It may be difficult, however, to maintain stable operation over the thousandfold range of ion beam intensity specified above.

If possible, it is thus desirable to anticipate the current level at which most of the testing will be done and design for this nominal point. If this cannot be done, maximum source stability should be sought at the low beam intensities where long tests will be conducted. As discussed in Section III-A-2, a rastered beam eliminates the need to vary the source intensity.

The above characteristics provide a scale against which the various sources may be compared. Where possible this comparison is made quantitatively in Table IV-2, which follows the discussion of the individual source characteristics.

2. Proton Creation Processes

Regardless of the type of ion source, proton creation is typically a two-step process of dissociating the molecules into hydrogen atoms which then are ionized. This ionization must occur rapidly because atomic hydrogen readily recombines to form the molecule, particularly on the walls of the ion source. Even after the proton is created it is likely to strike the walls of the source, lose its charge, and recombine with another hydrogen atom to form a free molecule, rather than passing through the ion extraction system into the beam. The large number of opportunities to lose the proton or hydrogen atoms explain, at least qualitatively, why proton guns are inherently rather inefficient in both mass and power efficiency.

a. Molecular Dissociation

The most direct method of dissociating hydrogen molecules is by heating. The percentage of atomic hydrogen is plotted as a function of temperature in Fig. IV-1 (Ref. IV-1). Clearly the high temperatures required make it very difficult to implement this technique in a practical ion

source design. A second method is to break up the molecule in a spark discharge. Little quantitative information is available concerning this method, but it is apparent that dissociation will occur only in a localized region and may be difficult to control. The third, most commonly used technique is that of electron impact. The reaction is

$$H_2 + e \rightarrow H + H + e.$$

Because this reaction is closely related to the production of protons by electron impact, it will be discussed in the following section.

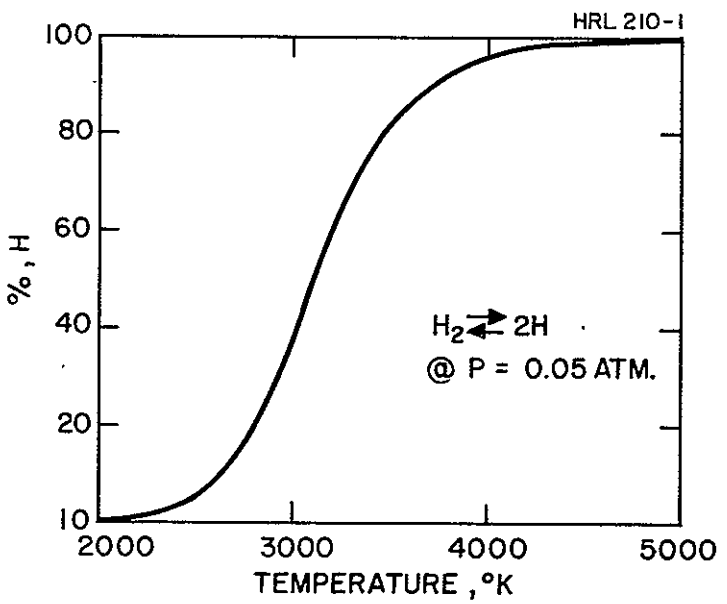

Fig. IV-1. Thermal dissociation of H_2.

b. Ionization

The only practical means of ionizing hydrogen atoms to form protons is by electron impact. A large variety of techniques employing either static or dynamic electric or magnetic fields or combinations of the two have been devised to accomplish this goal. Goodyear and Von Engel (Ref. IV-2) have listed the reactions possible as a result of electron impact on hydrogen, as shown in Table IV-1.

TABLE IV-1

Reactions Due to Electron Impact on Hydrogen

Number	Process	Threshold Energy, eV	Maximum Cross Section (10^{-16} cm^2)	Energy of Max Cross Section, V
1	$H_2+e \rightarrow H + H + e$	11.5	0.6	12
2	$H_2+e \rightarrow H_2^+ + 2e$	15.4	1.1	80
3	$H_2+e \rightarrow H^+ + H + 2e$	18.0	0.005[a]	120[a]
4	$H_2+e \rightarrow H^+ + H^+ + 3e$	46	0.005	120
5	$H_2^+ + e \rightarrow H^+ + H + e$	12.4	3 to 16	16
6	$H_2^+ + e \rightarrow H + H$	0	$\sim$ 100	—
7	$H + e \rightarrow H^+ + 2e$	13.5	0.65	40
8	$H + e \rightarrow H^* + e$	10.2	0.7	25
9	$H^* + e \rightarrow H^+ + 2e$	3.3	15	9
10	$H_2+e \rightarrow H_2^* + e$	10.3	0.2	60
11	$H_2^+ + H_2 \rightarrow H_3^+ + H$	Thermal	Large	—

H^* = an excited state of hydrogen

[a]The value of $\sigma = 0.005$ for process 3 is probably a typographical error. Kieffer (Ref. IV-3) cites two experimental values of $\sigma = 0.058$ for process 3 with the electron energy at the maximum being about 105 eV.

Reaction 1 of Table IV-1 is the dissociation reaction discussed earlier. The atomic hydrogen thus formed may be ionized by a reaction such as 7 to form protons. This mechanism competes with the direct ionization from the molecule shown in reaction 2 (see Fig. IV-2). All of the other reactions listed contribute little to the formation of protons because their cross section is small, the threshold energy is high, or the occurrence of the target species (i.e., molecular ions or excited states) is only a small fraction of the total hydrogen content. Figure IV-3 expresses this same information in a somewhat different manner by illustrating the percentage of total ionization in the beam which these protons represent as a function of electron energy. Reaction 1 of Table IV-1 indicates that the production of free hydrogen atoms will be maximized in a discharge if the mean energy of the impacting electrons is 12 V.

c. Recombination

Obviously, one means of sustaining a high fraction of atomic hydrogen in the ion source is to reduce the rate at which the atoms recombine to the molecular state. This recombination is a radiationless process requiring the presence of a third body. At pressures above 1 Torr appreciable volume recombination may take place by three body collisions; below this pressure, however, wall recombination predominates. If any metal surface exists in the discharge chamber it is readily reduced by the hydrogen, and a surface hydride is formed. On such a surface, it is energetically probable that two hydrogen atoms can approach each other to form a molecule and then escape as a neutral molecule, with any energy difference being communicated to the metal. For materials such as Al_2O_3 and SiO_2, whose oxides are not readily reducible, surface oxygen saturates the valency bonds and incident hydrogen

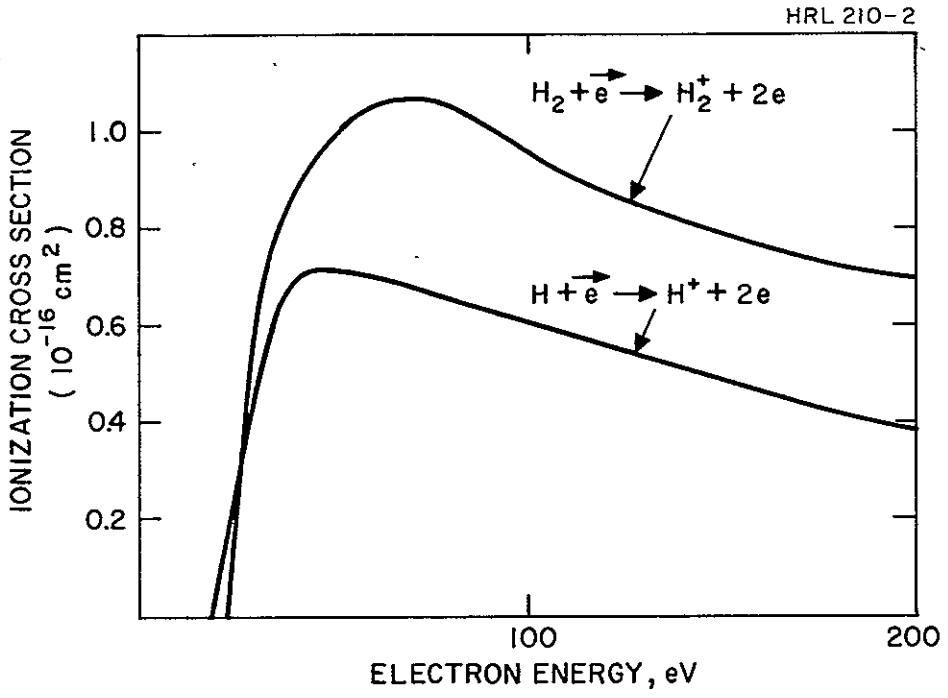

Fig. IV-2. Electron impact ionization cross section.

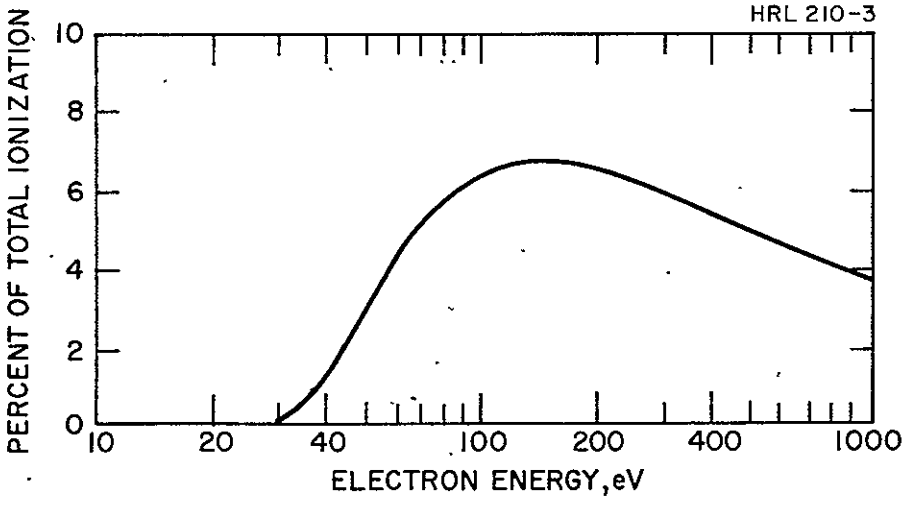

Fig. IV-3. Production of protons with kinetic energy greater than 2.5 eV by electron impact in H_2 expressed as a percentage of the total ionization cross-section.

is not captured. This effect weakens after long exposure to atomic hydrogen and even these materials are reduced to the metallic state at the surface, and recombination occurs.*

Typical reported wall recombination rates for atomic hydrogen are

pyrex	2×10^{-5}
quartz	7×10^{-4}
Al_2O_3	0.33
all metals	1.0
ice	$\sim 0.$

It can be concluded from the above that recombination may be reduced by the proper choice of material for the source walls and good design practice which reduces any sputtering or evaporation of metal onto the source walls. The chemical nature of the material being ionized (hydrogen) will ultimately degrade any material and increase the wall recombination rate.

3. Types of Proton Sources

There are a large number of generic types of ion sources, each with many individual designs, which will produce a proton beam. An excellent review of the basic types was presented by Hoyaux and Dujardin (Ref. IV-4). New materials technology and fabrication techniques have improved the sources since that time, but the basic concepts remain the same. In this section we limit the discussion to established concepts whose performance has been documented in the technical literature. Several sources are now commercially

*For reference, satisfactory operation of an rf source for 1000 hours has been reported.

available and may be purchased complete with the necessary power conditioning to operate with guaranteed specifications. The ready availability of spare parts makes these sources particularly attractive to a user.

All of these sources dissociate and ionize the hydrogen by electron bombardment. They differ radically in power requirements and general operating conditions. Of particular interest for this application are two requirements mentioned earlier which are not always considered for the same applications. The first is a minimum kinetic ion energy spread in the source. This is important to permit satisfactory mass separation at the relatively low beam energies used here. The second is the ability to vary the source output current intensity over a wide range to accommodate the required flux variations.

a. Radio Frequency Ion Sources*

The radio frequency ion source, sometimes called an electrodeless discharge source, has been a standard for many years in high voltage particle accelerators used for nuclear physics experiments. RF power is coupled into a quartz (or other insulating material) tube containing hydrogen gas at a pressure ranging from 10 to 100 μm of mercury. The mean free path of an electron in the source is on the order of 1 cm. Thus, electrons will be accelerated by the imposed electromagnetic field and will participate in the reactions listed in Table IV-1. Under the proper conditions, stable plasma similar to that discussed later will be created, from which an ion beam may be extracted.

*A comprehensive review of the rf ion source was made by Blanc and Deghilh (Ref. IV-5).

Two techniques are possible for coupling the rf energy to the plasma, as shown in Fig. IV-4. Electrostatic coupling is accomplished by inserting a pair of electrodes into the discharge chamber. The electric fields are maintained by the charges on the electrodes. The electric fields are relatively high and the circulating currents are relatively low compared with the magnetic coupling discussed below.

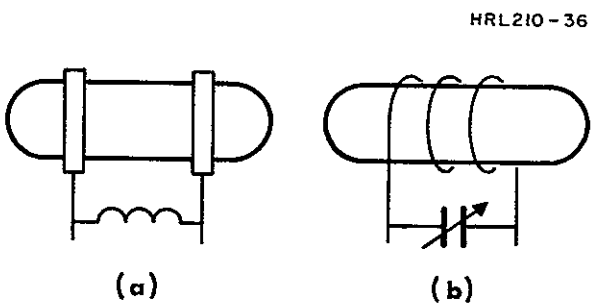

Fig. IV-4.
Modes of coupling power into an rf ion source. (a) Electrostatic. (b) Magnetic.

It is reported that the electrostatic source is easy to start and that it will work over a wider pressure range than an electromagnetically coupled source. At very low source pressures ($\sim 10^{-4}$ Torr) the electrons are produced by secondary emission at the walls rather than by ionization in the gas. The primary disadvantage of this device is that the high electric fields create an ion population with a large energy spread, which should be avoided in the choice of a source. This spread in ion energy can be reduced somewhat by increasing the frequency of the driving signal. One example of this technique

is the source developed by R.N. Hall (Ref. IV-6), which immerses the plasma vessel in the fringing field of an open end coaxial transmission line. The coupling was essentially electrostatic and the frequency used was 450 MHz. At this frequency, ions cannot respond to the applied voltage and the energy is coupled preferentially into the electrons. The exact ion energy was not stated. However, the beam could be brought to "pin point focus at the target," thus indicating a low energy spread.

The second, more common, coupling method is to place the discharge chamber inside a solenoid which is activated with rf power at approximately 10 MHz. The alternating magnetic field generated in the discharge chamber accelerates the electrons. Generally, the induced electric fields are relatively small here and the circulating currents are somewhat larger than in the electrostatic design. Energy spreads ranging from 20 eV (Ref. IV-7) to 65 eV (Ref. IV-8) have typically been reported for this device. The lower electric fields make this device somewhat more difficult to start, particularly at low pressures. Quite frequently an axial magnetic field is used to increase the electron path length and to improve stability. Improved operation at the cyclotron resonance frequency has been reported (Ref. IV-9).

Beam currents up to 1 mA are typically reported for this type of source. Proton fractions up to 90% of the total ion current in the beam have been observed under optimum conditions; 50 to 70% is common for well designed sources. Hydrogen consumption varies according to source design but is typically of the order of 4 cm^3/hour at STP for 1 mA of output beam. However, it may not be possible to scale down the gas flow directly with beam current. Operating frequency varies as well, ranging from 1 to 400 MHz; 10 MHz is common,

and rf power requirements are a few hundred watts. Source lifetimes of 1000 hours at the current levels required for this application are reported (Ref. IV-8).

Of the various sources surveyed, the electromagnetic rf ion source most nearly meets all the requirements. It fully meets the beam requirements and is adequate in terms of mass efficiency and proton yield. If this type of source is to be designed or adapted to this application, care should be taken to assure stable operation over long periods by choosing high quality materials for its construction and designing both the power supplies and the hydrogen feed system with stability as a primary consideration. An effort to extend the stable operating region to the widest possible current density range would also improve its adaptability to this task. A typical rf source is shown in Fig. IV-5.

b. Electron Bombardment Sources

As the name implies, electron bombardment sources ionize by direct impact of electrons on the hydrogen molecule or atom. The distinction here is that in contrast to other types of sources, conditions are such that no plasma is created nor is any arc or discharge struck. A common example of this type of device is a hot filament ion gauge tube in which the number of ions created is linearly related to the pressure over several orders of magnitude. For purposes of discussion, electron bombardment ion sources are divided into three types — low voltage, high voltage or canal ray, and crossed beam.

(1) Low Voltage Source — The low voltage type of source has been used for many years in mass analysis because of its ability to ionize any material that can be vaporized. Typical of the type most useful for the purpose at hand is that described by Redhead (Ref. IV-10). A modified form of

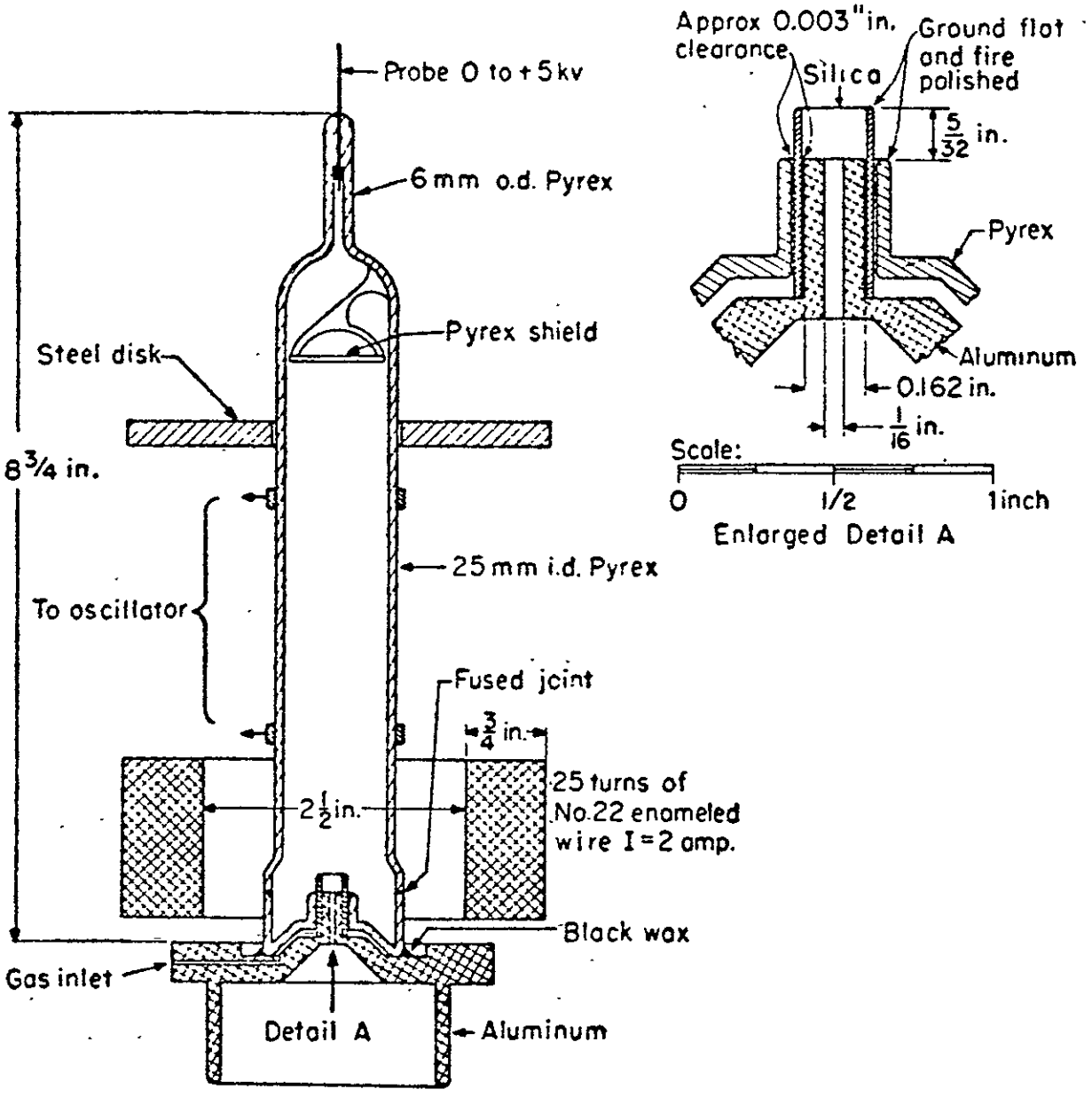

Fig. IV-5. Cross section of ion source and completed assembly of glass vessel and aluminum base. (From C.D. Moak, H. Reese, Jr., and W.M. Good, Nucleonics 9, 18 (1951).)

this source is shown schematically in Fig. IV-6. Hydrogen gas is introduced into the ionization region, where it is bombarded by electrons with the resulting production of protons governed by the equations of Table IV-1 and Fig. IV-2. The axial magnetic field significantly increases the electron path length and hence the source efficiency. The electrons are axially restrained by holding both ends of the discharge chamber at cathode potential, thus making it energetically impossible for electrons to reach them after any energy loss. The repeller electrode is maintained at a positive potential to provide an electrostatic field in the proper direction to sweep positive ions toward the extraction aperture. The magnetic field, which does not appreciably affect the trajectories of the ions, prevents the electrons from being collected on the repeller without having first suffered a collision. The electron cloud forms a potential well which traps ions. Redhead has reported that this type of source is capable of trapping ions in the source for periods as long as 1 sec. This is desirable in a proton source because when a proton collides with the metal wall of the source, it is re-emitted as part of a hydrogen molecule and must be both dissociated and ionized again to be useful.

This type of ion source has several advantages. Primary among these is that it fulfills the two desirable criteria mentioned earlier. It is adjustable in current over several orders of magnitude and produces ions with a relatively small energy spread, ranging down to less than 1 eV for specially designed sources (Ref. IV-11). The primary difficulty with this type of ion source is that the mass efficiency is of the order of 1% or less. Thus, it presents a large gas load to the system when operating at high output currents. A second, and less important, disadvantage is that the source requires a thermionic cathode, which is subject to contamination and has a finite lifetime.

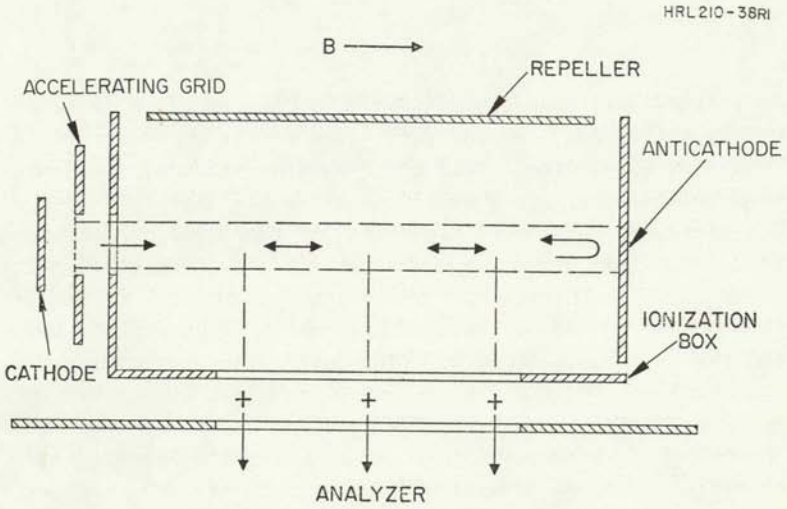

Fig. IV-6(a). Schematic diagram of trapped electron ionization source.

M 6915

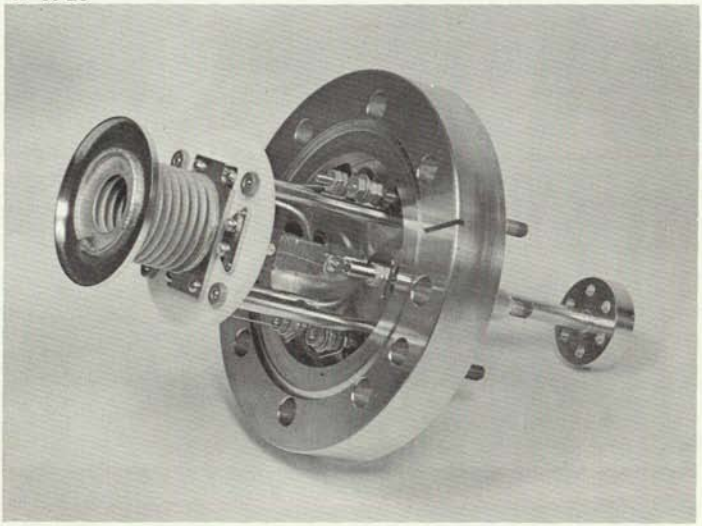

Fig. IV-6(b). Photograph of trapped electron ionization source.

Commercial sources of this type generally are relatively complex because they are designed to ionize a wide variety of materials. A much simpler model designed specifically for this purpose is in use at Hughes Aircraft Company (Ref. IV-12). It is capable of producing a proton current equivalent to 2000 times the nominal solar wind value over a 2.5 cm diameter circle. Input power is about 20 W. The entire vacuum station, including the source chamber and the integrating sphere, is pumped by a single 400 liter/sec ion pump. A single feedback loop that monitors the emitted ion beam current and adjusts the cathode emission to compensate for drift in line voltage or hydrogen flowrate serves to stabilize the beam for periods of several days. This is shown in Fig. IV-6(b).

(2) High Voltage or Canal Ray – This is perhaps the oldest type of ion source, having been used by Thompson in some of his early experiments. The source is basically a diode that operates with a pressure of about 10^{-2} Torr of hydrogen. Protons are created by electron impact as the electrons traverse from cathode to anode. A small hole is drilled in the cathode so that some of the ions which naturally fall toward the cathode pass through the hole and form a beam – hence the name "canal ray." Such sources typically are operated at greater than 20 kV and consume several kilowatts of power.

While such sources have several merits, their overriding disadvantage for our application is that the energy spread of the ions is approximately 1/5 the total source voltage – typically 5 kV. This energy spread is fundamental to this type of source and arises because ions may be created anywhere in the source volume and thus may arrive at the cathode after falling through a potential drop up to the full anode voltage.

(3) Crossed Beam Sources — This type of device has more often been used to detect or analyze an atomic beam (Ref. IV-13), but it could serve as a source of protons as well. Basically a beam of thermal hydrogen atoms or molecules is bombarded by an electron beam or passed through a cloud of electrons trapped in a magnetic field, as discussed above. The probability of ionization is much less than in the closed volume of the low voltage electron bombardment source, but the protons created have a directed energy toward the extraction aperture where the beam is formed. This results in high utilization of the protons that are formed. If the incident hydrogen beam can be dissociated by a spark or by thermal means prior to ionization, the efficiency can be increased even more.

Unfortunately, the relative merits of this system cannot be adequately assessed because no published data have been found that are pertinent to the system described. The closest work appears to be that published 35 years ago by Smith and Scott (Ref. IV-14). Its lack of reported use as a proton source appears to indicate that it is inferior to other designs, probably because of its high gas consumption.

c. Gas Discharge Source

The distinguishing feature of this type of source is that a discharge is struck between cathode and anode and the protons are extracted from the volume of plasma which is created. While a detailed discussion of the plasma is beyond the scope of this report, some of its unique properties are important to an understanding of the source operation.

A plasma is a collection of equal numbers of electrons and ions and is thus macroscopically neutral. Individual electrons and ions travel independent paths, but on the average are attracted to each other by electrostatic forces. The

electrons generally have an approximately Maxwellian energy distribution with a mean energy of 1 to 10 eV (10^4 to 10^5 °K); on the other hand, the ions have a mean energy approximately equal to that associated with the temperature of the ion source walls, (i.e., 300 to 500°K). The electrons, which have low mass, are easily confined by a magnetic field. The protons, which are 1836 times heavier, act more as a gas and are influenced primarily by collisions with the walls and other particles.

Because the charged particles are highly mobile, voltage gradients cannot exist within the plasma except under very unusual circumstances. Thus there are, in general, three distinct regions in the discharge: the main body of the plasma, plus two plasma sheaths, one at the cathode and one at the anode (as shown in Fig. IV-7). Large current densities of electrons may be carried from the cathode across the plasma sheath because of its relatively small dimension (typically 1.0 cm). The ion current arriving at the cathode has been shown by Bohm (Ref. IV-15) to be

$$J_i = n_i e \left(\frac{kT_e}{m_i}\right)^{1/2}$$

where

J_i ≡ ion current density
n_i ≡ ion density in plasma
e ≡ electronic charge
k ≡ Boltzmann constant
T_e ≡ electron temperature
m_i ≡ ion mass.

The ion flow to a nonemitting surface at cathode potential or to the anode is somewhat less due to the absence of the counterflowing electrons which neutralize part of the ion space charge. Ion emission from the plasma surface is beneficial because it provides a mechanism by which ions may be extracted from the plasma, but it is detrimental because ions impinging on the cathode sputter the cathode surface and ultimately destroy

It is obvious that a number of sources can be designed based on the discharge concept. These are summarized here under three classes: capillary arc, and crossed-electric and magnetic field devices working at high and low plasma density.

(1) Capillary Arc — In a capillary arc source the discharge between cathode and anode is physically constricted and made to pass through a capillary tube. This increases the power density in this region and improves the mass efficiency and proton output. The ions have a relatively small energy spread. Even though the characteristics of this source appear attractive, it has not been in general use since the advent of the crossed field sources described below and the rf source described above. The principal reasons appear to be the short lifetime of the thermionic cathode and the tendency for the source to be unstable.

(2) Low Plasma Density Crossed Field Discharge — The crossed field discharge sources are based on the same mechanism of electron confinement described above — an axial magnetic field which confines the electrons radially, coupled with electrostatic barriers at each end of the field lines which reflect the electrons at these points. The fact that the electrons exist in a plasma does not affect this trapping mechanism. Low voltage devices of this nature were first

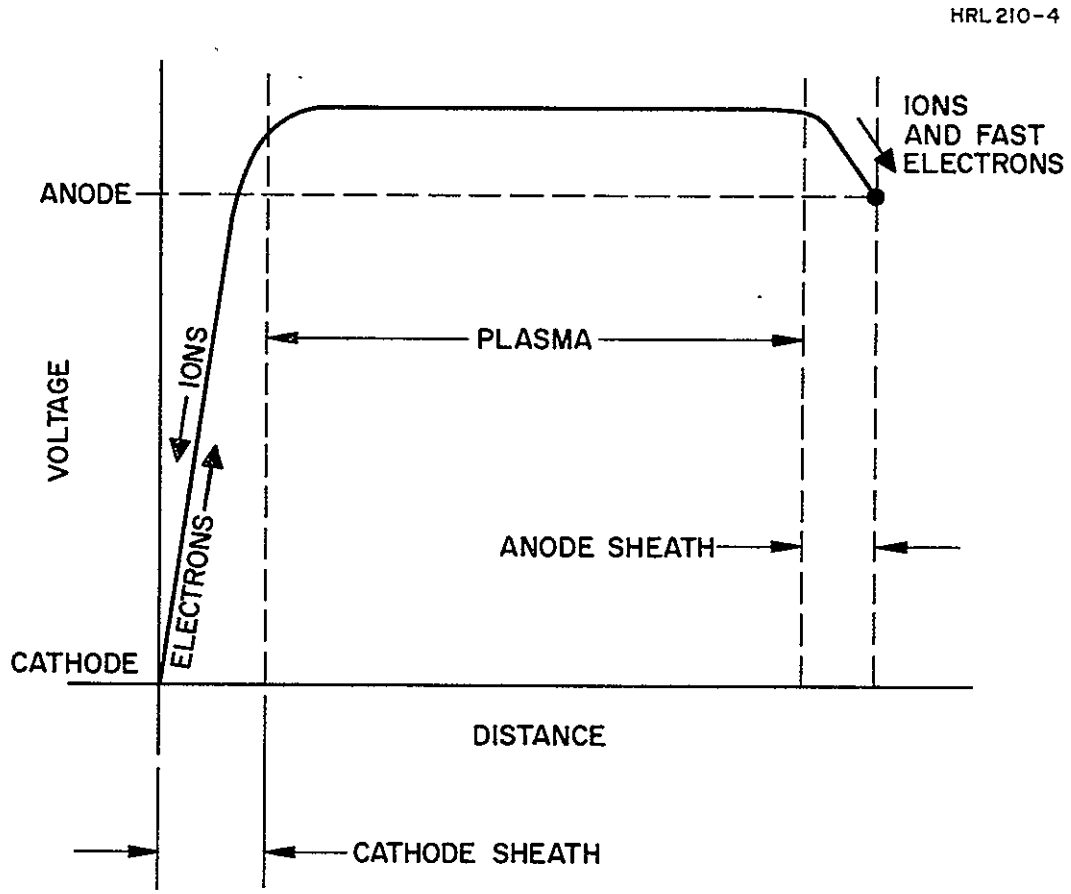

Fig. IV-7. Voltage distribution in a simple plasma discharge.

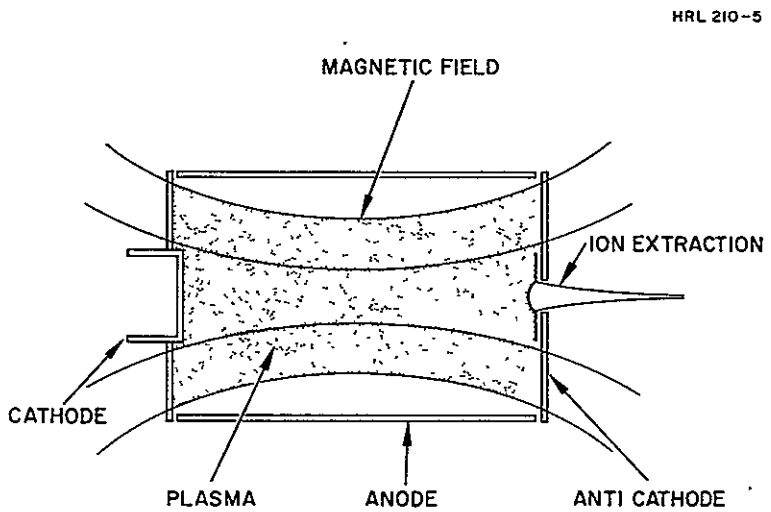

Fig. IV-8.
Low voltage crossed field ion source (Penning source).

described by Finkelstein (Ref. IV-16) and independently by Penning (Ref. IV-17) in about 1940. They have subsequently found wide application in many fields of plasma physics and gas discharge devices. For example, ion engines for space propulsion based on these principles produce mercury ion beams with currents up to 2 A.

A schematic diagram of a typical source is shown in Fig. IV-8. The potential diagram of Fig. IV-7 is appropriate to this type of device. Operating parameters depend on the specific source design; typically, however, the discharge voltage is less than 100 V, the magnetic field is 100 gauss, and the discharge current is 5 to 50 times the extracted ion beam current. The source requires a pressure in the discharge chamber of greater than 10^{-4} Torr for stable operation. Under optimum operating conditions the mass efficiency can approach 100%, although the proton fraction may be quite low as a result of the difficulty of maintaining a dissociated hydrogen gas in a metal container. The ion energy spread is on the order of 10 V, depending primarily on the discharge voltage.

In many ways the characteristics of this source resemble those of the electromagnetic rf source. It will produce medium to high currents with a relatively low ion energy spread. It is inferior to the rf source in the percentage of protons in the output beam. It requires more complicated power supplies, plus a thermionic cathode which has a finite useful lifetime due to sputter damage by ions which fall through the cathode sheath voltage. Should an application arise where a large beam on the order of 1 m diameter is required and where the beam purity is not important, this source would be excellent.

It is also possible to operate a similar device at much lower pressure but a much higher magnetic field and higher discharge voltage (Ref. IV-18). This type of operation does not require a thermionic cathode, but gives only low ion current yield with a high energy spread.

(3) High Plasma Density Crossed Field Discharge — By combining the crossed field discharge concept with a mechanical construction of the discharge, Von Ardenne (Ref. IV-19) designed the duoplasmatron ion source. At present the high current capabilities, stability, and relatively trouble-free operation of this device are being exploited in its use as an ion source for high voltage accelerators. It has also been considered for use as an ion thruster for space vehicles and as a very high intensity electron source for electron bombardment heating.

A typical duoplasmatron ion source is shown in Fig. IV-9. The arc is struck between the cathode and anode by application of 100 to 200 V, depending on the gas pressure. The arc is constricted both by the aperture in the intermediate electrode and by the highly nonuniform magnetic field in the region between the intermediate electrode and the anode. This double compression of the arc produces the desired high plasma density in the anode aperture. As shown in Fig. IV-10, the arc voltage consists of the cathode voltage drop of about 25 V; the double sheath in front of the canal opening on the cathode side, and 2 to 3 double sheaths inside the canal. Each of these sheaths consists of potential jumps of 25 to 30 V. The rest is distributed over the normal plasma voltage gradient. The electrons are accelerated toward the anode and the ions toward the cathode, passing the double layers.

The magnetic lens becomes effective in the final third of the intermediate electrode canal; it detaches the plasma from the canal wall and focuses it at the emission opening. This portion of the discharge is called the anode plasma. Losses of ions to the walls in the anode plasma take place now only between the topmost double layer and the boundary of discontinuity in the canal, as well as at the anode.

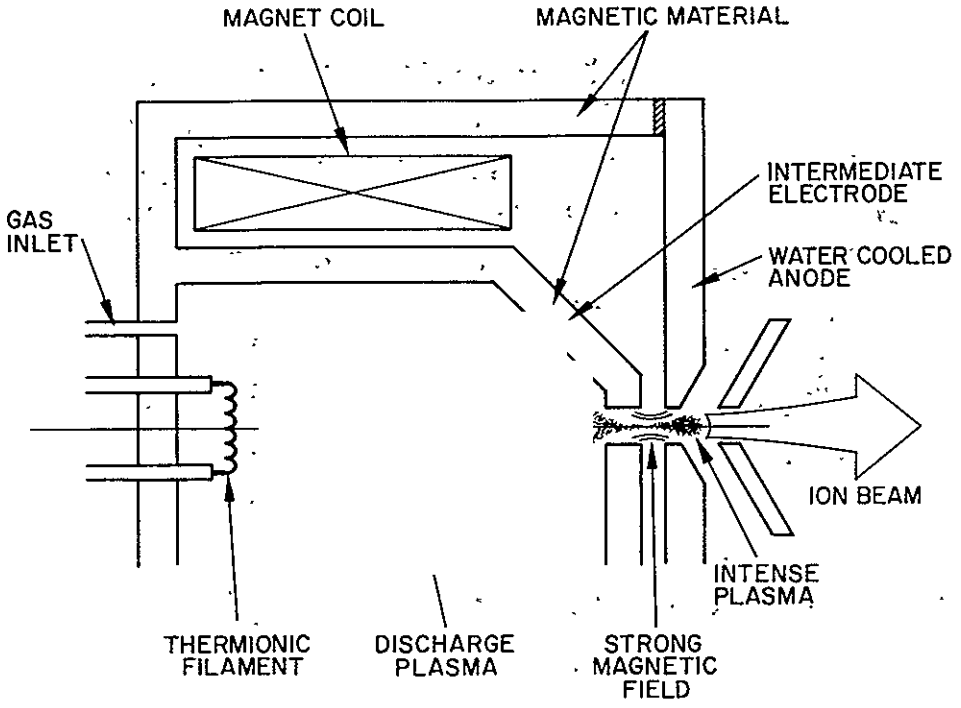

Fig. IV-9. Schematic of duoplasmatron ion source

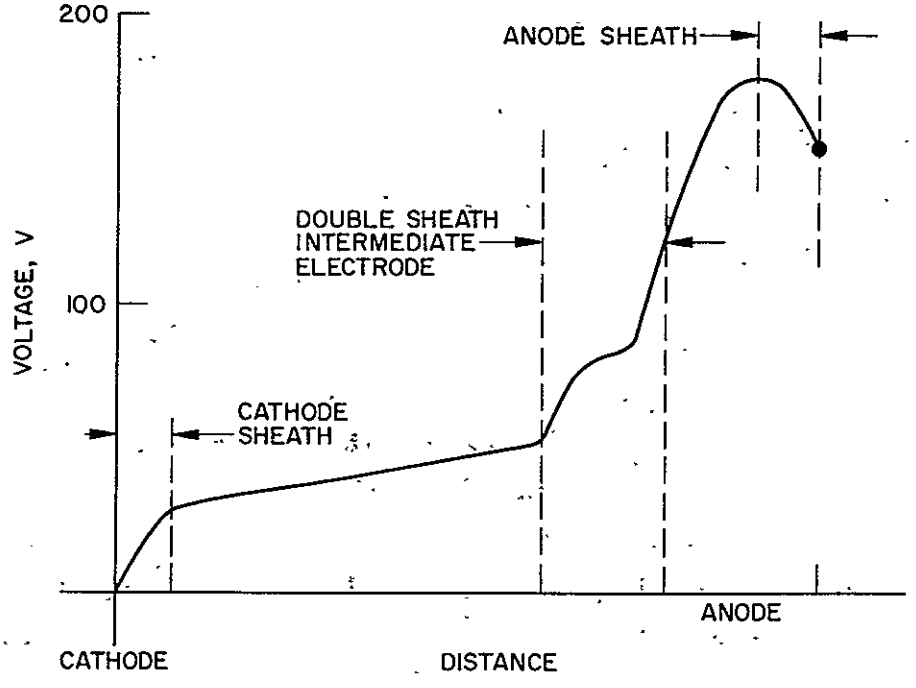

Fig. IV-10. Voltage profile in duoplasmatron ion source.

These losses must be compensated. For this reason, ions must flow out of the anode plasma into the canal as well as upward to the anode. This is possible only if a positive potential hill exists in the plasma between the cathode and the anode. This potential hill can arise only when positive space charge is being produced by heavy ionization. This is precisely what happens; the high energy electrons that have been accelerated through the last double layer, enter a region of high current density and thus of a high degree of ionization by means of magnetic focusing. The potential hill accelerates ions in both axial directions. One part flows into the canal of the intermediate electrode and the other toward the emission aperture. The magnitude of this negative anode drop is not constant. It depends on the gas pressure, discharge current, and above all on the potential of the intermediate electrode. If the intermediate electrode potential is increased in the negative direction to about the potential value on the cathode, the ion losses to the walls increase considerably, while the electron current to the intermediate electrode decreases. The increase in the ion losses to the walls in the upper end of the canal requires an increased ionization in the anode plasma, which in turn results in an increase in the potential hill and in the plasma density.

This source produces the highest current density of any type of ion source. Unfortunately, this is a disadvantage for our application because, as will be shown below, such a high current beam cannot be focused without the application of very high extraction voltage (typically 10 to 100 kV). This is, of course, far higher than desired here. This factor overshadows the other desirable features of the source — its high proton yield, high mass efficiency, and stable operation. As seen by the exploded view of a source of this

type (Fig. IV-11) recently constructed at HRL (Ref. IV-20), the mechanical design is quite complex, making source construction expensive.

4. Selection of Ion Source

A number of the proton sources most useful for this application were discussed above. Table IV-2 summarizes the important characteristics of each. While no one source possesses all of the desirable characteristics, the electromagnetically coupled rf source and the low voltage electron bombardment ion source most nearly fill the requirements. The electron bombardment source is superior in terms of lower ion energy spread and variable current operation. It is a logical choice for small diameter beams or in experiments requiring ion fluxes to the order of 100 solar constants. It is quite possible that further optimization of this design would increase the output current by an order of magnitude and make it generally useful over the entire range specified by this contract.

Based on current technology, however, the rf source is most suited to the system requirements set forth here because it can easily reach the current levels desired, has a nominal lifetime of 1000 hours that is adequate for most experiments, and produces a beam that is rich in protons. With proper care, the two marginal characteristics (the inability to vary the output current level and the ion energy spread of $\sim$ 50 eV) can be accommodated by the design of the ion optical system and the mass separator. No design program has yet been undertaken with the specific goal of improving these characteristics; it is very likely that they also can be improved to make this source more useful.

TABLE IV-2

Proton Sources

Type of Source		Beam Current Range, mA	Proton Yield, %	Gas Consumption, cm^3/hour at STP/ mA/Mass Utilization Efficiency, %	Operating Pressure, μm	Ion Energy Spread, eV	Lifetime, Power Supply, Control, etc.	Advantages	Disadvantages
Radio Frequency	Electromagnetic	0.1 to 20	50 to 90	6 to 20 cm^3 STP/hr	1 to 40	20 to 100	Life to 1000 hours; supplies simple; control average	Long life and high percent of protons	Narrow beam current range
	Electrostatic	less than 0.1			above 10^{-2}	100		Low operating pressure and beam current	Wide energy spread
Electron Bombardment	Low Voltage	wide range	10	$\eta_m \sim 1\%$	10^{-5} and above	few eV	Life 1000 or more hours	Wide range of beam current	Low mass utilization
	High Voltage (Canal Ray)	Up to 1	25 to 60	$\eta_m \sim 10\%$	1000	Large (1/5 arc drop)	Life-long (no filament) high power (kW)		High power and large energy spread
	Crossed Beam	low current	high for dissociated beam	$\eta_m \sim 1\%$	N.A.	low ~ 1	Life limited by thermionic cathode	Low energy spread and wide range of beam current	Low beam current
	Capillary Arc	up to 4	10 to 20	10 to 20 cm^3 STP/hr	1 to 30	few eV	Life 20 to 50 hours due to cathode	Monoenergetic	Short life, complicated electronics, hard to stabilize
Gas Discharge	Crossed Field (EXB) High Density	high > 10	50	$\eta_m \sim 100\%$	10 to 100	few eV	Require several power supplies and possibly cooling water	High mass utilization and high proton yield	Current too high
	Crossed Field (EXB) Low Density	high > 10	5 to 60	η_m = 1 to 100%	1 to 10	10	Life limited by thermionic cathode		Trade η_{mass} for proton yield, cathode life, or energy spread

FOLDOUT FRAME

2

FOLDOUT FRAME

M 5474

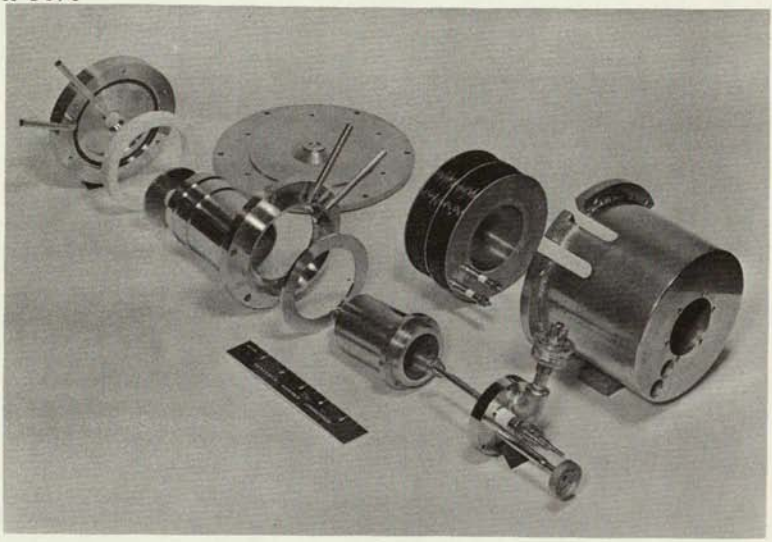

Fig. IV-11. Duoplasmatron ion source components. (Ref. IV-20).

5. Ion Extraction Systems

The foregoing sections have discussed a number of proton sources. To be useful, these protons must be extracted from the source and focused into a beam. The ion extraction system which accomplishes this forms a critical interface between the source and the ion transport system which controls the beam shape en route to the target.

The theory of charged particle focusing has been investigated extensively in the development of electron guns used for many purposes. Because the focal properties of electrostatic lenses are independent of particle mass, the theories derived for electrons are equally valid for protons.* The principal difference is that the currents that may be carried with a given set of lenses and accelerating voltages are much less for protons than for electrons because the particle velocities for a given accelerating voltage vary inversely as the square root of the mass. This reduced velocity also means that the number of charged particles per unit volume in the beam, and hence the space charge forces, are much greater for ion beams than for an electron beam with an equivalent current density and beam voltage. This also may be expressed by saying that at the same beam voltage an electron and proton beam will have the same space charge density when the proton current is 1/43 of the electron current since $\sqrt{m_e/m_H} = 1/43$.

a. Extraction of Protons from a Plasma, Compared with an Ion Cloud

The ion sources discussed above provide protons in two distinctly different environments — a plasma and an ion cloud. The first occurs in all high density sources (such as the rf source and the various E x B sources) and the second

*This is not true for magnetic focusing (which is not of importance here).

in the low voltage electron bombardment source, particularly when operating at low pressure. The difference is as follows: when extracted from a plasma the protons effectively come from a surface; when extracted from a charged cloud they come from a volume or at least a surface of finite thickness. These concepts are illustrated in Figs. IV-12 and IV-13.

Once the electrode shapes are chosen and the voltages are applied, solution of Laplace's and Poisson's equations describes the electric field and charge distributions in the beam. The particle trajectories may be calculated from this information because the particle trajectories and velocities determine the charge distribution. The calculation is an iterative one; when done in detail, it taxes the capacities of even the largest digital computers. A further complication is added by the effect on the ion creation process of the motion of the plasma sheath or the extraction of ions from the ion cloud. Only recently have techniques become available to model this phenomenon (Ref. IV-21), which requires further iterations to achieve a totally self-consistent solution.

When extracting from an ion cloud as shown in Fig. IV-13, it is apparent that once the equipotentials are established the trajectory and final energy of an ion originating from any point are known. Clearly, in order to maintain a small energy spread in the emergent beam, only equipotentials covering a small voltage range should bulge into the source volume. It is also clear that the repeller electrode which pushes ions into the region from which they are extracted will increase the source output. The difficulty in any such model is that the spatial and energy distributions inside the source generally are not known in detail.

Ion extraction from a plasma surface as shown in Fig. IV-12 has been studied by a number of authors interested in producing high intensity ion beams (Ref. IV-22) and those

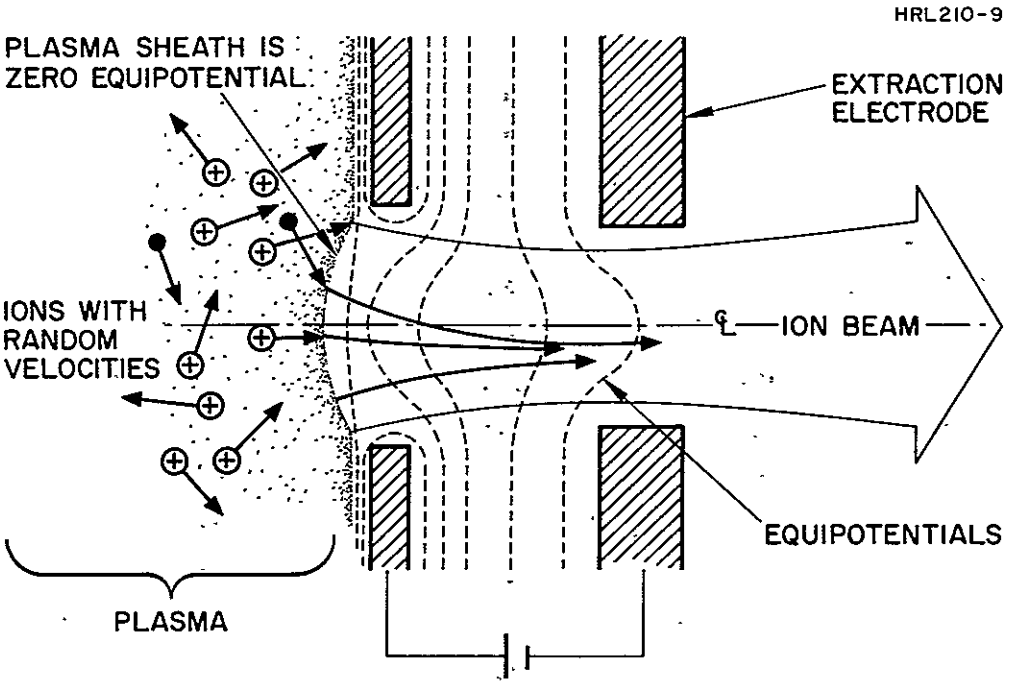

Fig. IV-12. Ion extraction from a plasma.

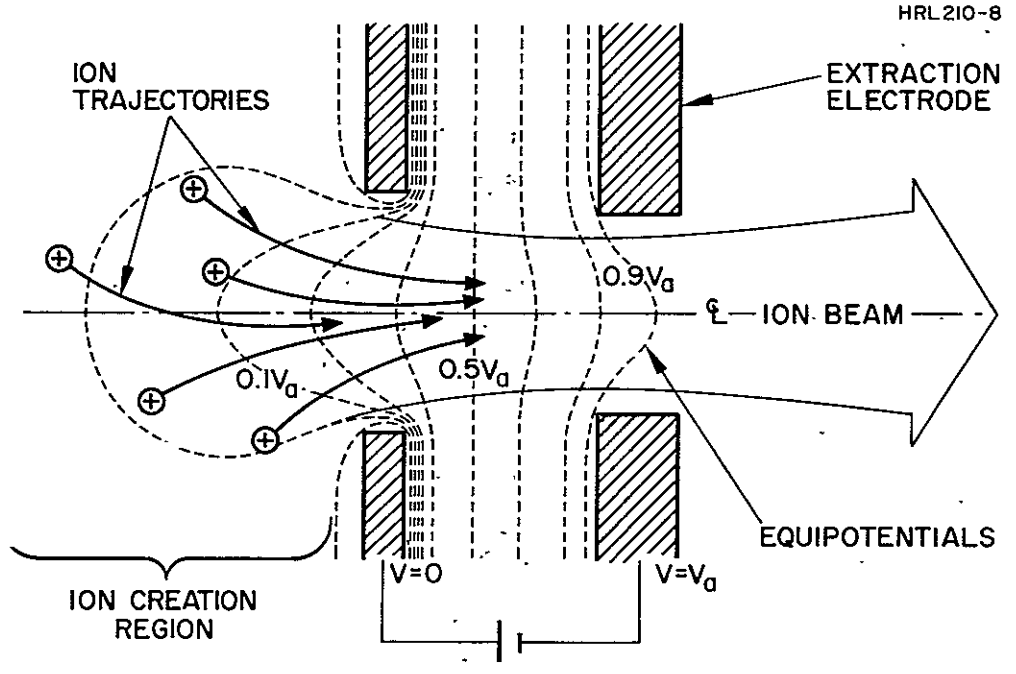

Fig. IV-13. Ion extraction from an ion cloud.

interested in designing long life, efficient ion thrusters for space propulsion (Refs. III-23, III-24). Hyman (Ref. III-23) has provided a functional model based on the criteria that (1) the plasma surface is an equipotential, (2) there is zero field gradient on either side of the plasma surface, and (3) all ions which arrive at the surface of the plasma must pass through it and be carried away in the beam. These concepts have been used by Kramer and King (Ref. IV-24) to calculate the divergence of the ion beam as a function of ion beam current, applied voltage, and electrode shape.

Designers generally have attempted to control the position of the plasma sheath by the shape of the electrodes and the applied voltages. An attempt has been made (Ref. IV-25) to provide independent control by stretching a fine mesh across the extraction aperture to provide an attachment point for the sheath. Although not stated there, the mesh openings should be less than the Debye distance* in the plasma to adequately define the plasma surface. By this means the plasma surface has been fixed and the beam stabilized over a range of current and voltage values. In particular reference is made to removing some of the instabilities that occur in an rf source operated at high efficiencies. It is not made clear, however, what effect the introduction of the metallic grid into the discharge chamber of the rf source had on the proton yield (due to increased recombination of the atomic hydrogen or protons) or on source lifetime (due to deposition of sputtered grid material on the source walls).

*Debye distance = $\lambda = (\varepsilon_o kT_e/n_e e^2)^{1/2} \sim 0.01$ cm for typical plasma source where ε_o = permittivity of space = 8.85×10^{-12} farad m^{-1}.

b. Ion Gun Perveance

A useful concept for describing the performance of an ion gun is its perveance, which is defined by the equation

$$I_i = GV_T^{3/2} \qquad \text{(IV-1)}$$

where

$I_i \equiv$ ion beam current
$V_T \equiv$ total extraction voltage
$G \equiv$ perveance.

The perveance is a quantity calculated by the techniques discussed above (Ref. IV-24). It depends only on the relative dimensions of the electrodes. Thus, an ion gun of given extraction geometry operating at a given voltage will focus a fixed current, regardless of the aperture size (i.e., the current density will increase as the aperture dimensions decrease).

As discussed earlier, the source must provide a maximum of approximately 10 μA of protons. Assuming that the protons represent only 40% of the total ion beam, a total current of 25 μA must be extracted from the source. The current densi at a source with extraction area of 10^{-2} cm^2 will be

$$J_{source} = \frac{25 \times 10^{-6} \text{ A}}{10^{-2} \text{ cm}} = 2.5 \text{ mA cm}^{-2}.$$

The perveance of the ion extraction system must simultaneously handle all the charged species at one time. Assuming that the beam is 40% H_1^+, 50% H_2^+, and 10% H_3^+, the required perveance $(I/V^{3/2})$ for the different species is, at 500 V,

$$G_{H^+} = \frac{10^{-5}}{1.12 \times 10^4} = 9 \times 10^{-10} \text{ AV}^{-3/2}$$

$$G_{H_2^+} = \frac{1.25 \times 10^{-5}}{1.12 \times 10^4} = 1.1 \times 10^{-9} \text{ AV}^{-3/2}$$

$$G_{H_3^+} = \frac{2.5 \times 10^{-6}}{1.12 \times 10^4} = 2.2 \times 10^{-10} \text{ AV}^{-3/2}$$

Because the perveance of a given geometry varies inversely as the square root of the mass of the charged particle being accelerated, the equivalent proton perveance required for the extraction system is

$$G_{H^+} = 0.9 \times 10^{-9} \times 1 = 0.90 \times 10^{-9} \text{ AV}^{-3/2}$$

proton equivalent $G_{H_2^+} = 1.1 \times 10^{-9} \times \sqrt{2} = 1.56 \times 10^{-9} \text{ AV}^{-3/2}$

proton equivalent $G_{H_3} = 2.2 \times 10^{-10} \times \sqrt{3} = 0.38 \times 10^{-9} \text{ AV}^{-3/2}$

proton perveance required

at 500 V = $G_{H^+} = 2.84 \times 10^{-9} \text{ AV}^{-3/2}$

at 2000 V = $G_{H^+} = 0.36 \times 10^{-9} \text{ AV}^{-3/2}$.

A typical ion extraction system is shown in Fig. IV-14. This particular system has a calculated perveance of 0.4×10^{-9} $AV^{-3/2}$ and thus closely matches that required for the 2000 V extraction. This particular system also has an emittance diagram similar to that used for the ion optical system calculations.

The above defines the rate at which charged particles may be removed from the plasma surface without violating the space charge conditions necessary for proper focusing. Based on the conditions stated in the previous section for the formation of a stable plasma sheath position, the rate at which ions are removed must exactly equal the rate at which ions arrive. For a Maxwellian velocity distribution Bohm (Ref. IV-15) has shown that the ions approaching the sheath must have at least a kinetic energy equal to $1/2(kT_e/e)$ so that $\bar{v}_i = \sqrt{kT_e/m_e}$

$$ne\bar{v}_i A = n_i A_a e \sqrt{\frac{kT_e}{m_H}} = GV_T^{3/2} \qquad \text{(IV-2)}$$

where

$\bar{v}_i$ = mean ion velocity
n_i ≡ ion density ions/cm^3
V_T ≡ total extraction voltage.
A_a ≡ extraction aperture area
e ≡ electronic charge
k ≡ Boltzmann constant
T_e ≡ electron temperature ∿10 eV
m_H ≡ mass of hydrogen atom.

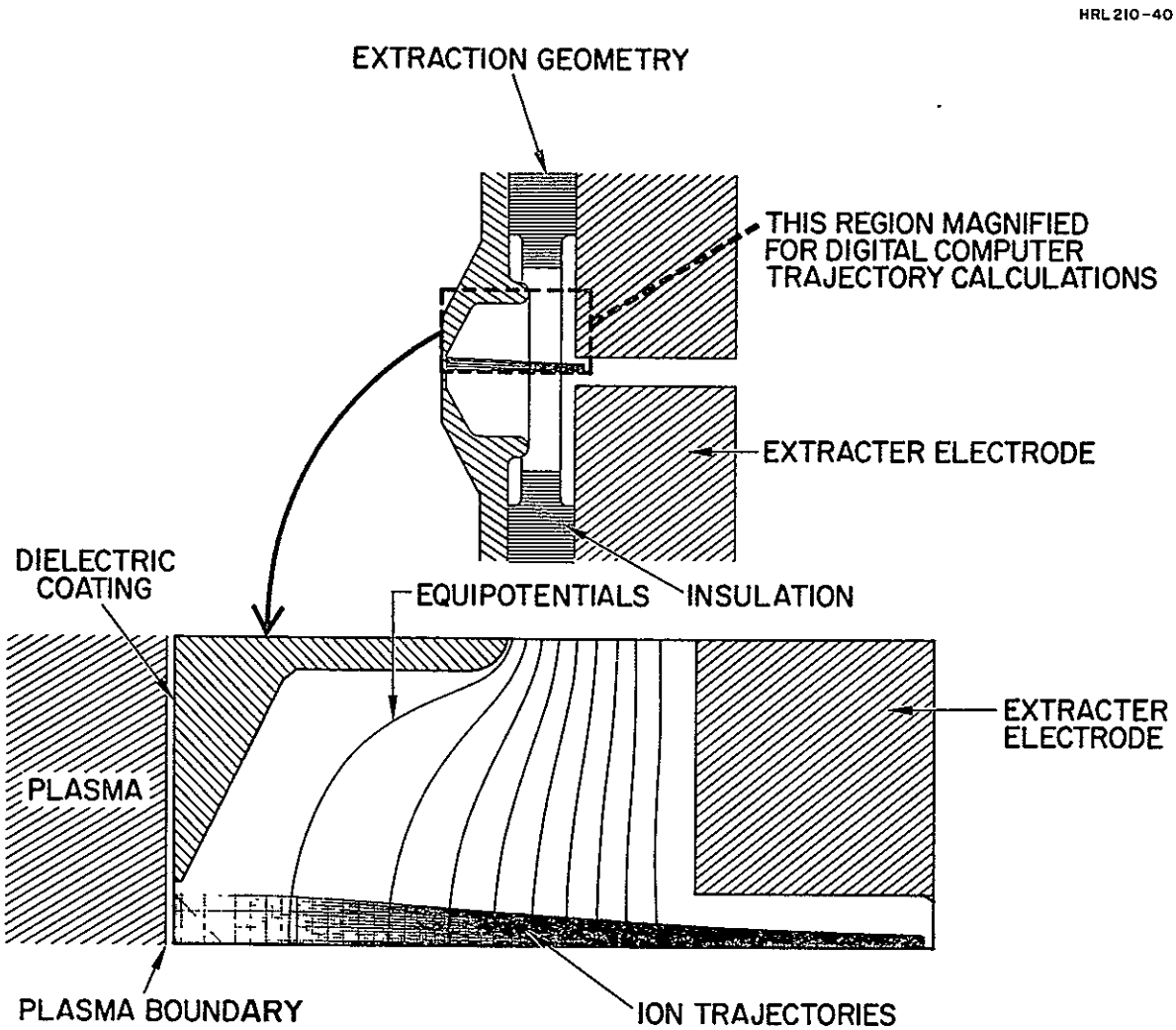

Fig. IV-14. Digital computer simulation of ion extraction from a plasma sheath.

Equation (IV-2) may be rearranged to yield

$$G = \frac{n_i A_a e}{V_T^{3/2}} \left(\frac{kT_e}{m_H}\right)^{1/2} .$$

Using this relationship it is possible to calculate the perveance of the ion gun required to extract a focused beam from a particular plasma source. Care must be taken to allow for the space charge of all charged particles in the extraction region. A nomograph for one set of conditions pertinent to our design is shown in Fig. IV-15.

c. Ion Source Emittance Diagram

It is necessary to describe quantitatively the output from the ion source and its extraction system in order to provide an input to the trajectory calculations for the beam transport system. This is typically done by means of an emittance diagram (Fig. IV-16) which defines the angle with respect to the beam axis at which the ion is traveling as a function of radius. In general, the emittance diagram is an area such that as shown in "A" of Fig. IV-16, for an ion source with a large random energy distribution in the beam or for an ion extraction system which produces a beam with nonlaminar ion trajectories. This represents an aberration which never can be corrected by any ion optical system and which is also very difficult to treat analytically because of the infinite number of combinations of radial position (r) and divergence angle (r') which the ion trajectories may have. It is possible, however, to design an ion gun as shown in Fig. IV-17 so that the ions appear to come from a virtual point source (see Fig. IV-14); this gives an emittance diagram of the type B shown in Fig. IV-16, which is a line rather than an area and may be represented as a simple function $r' = Kr$

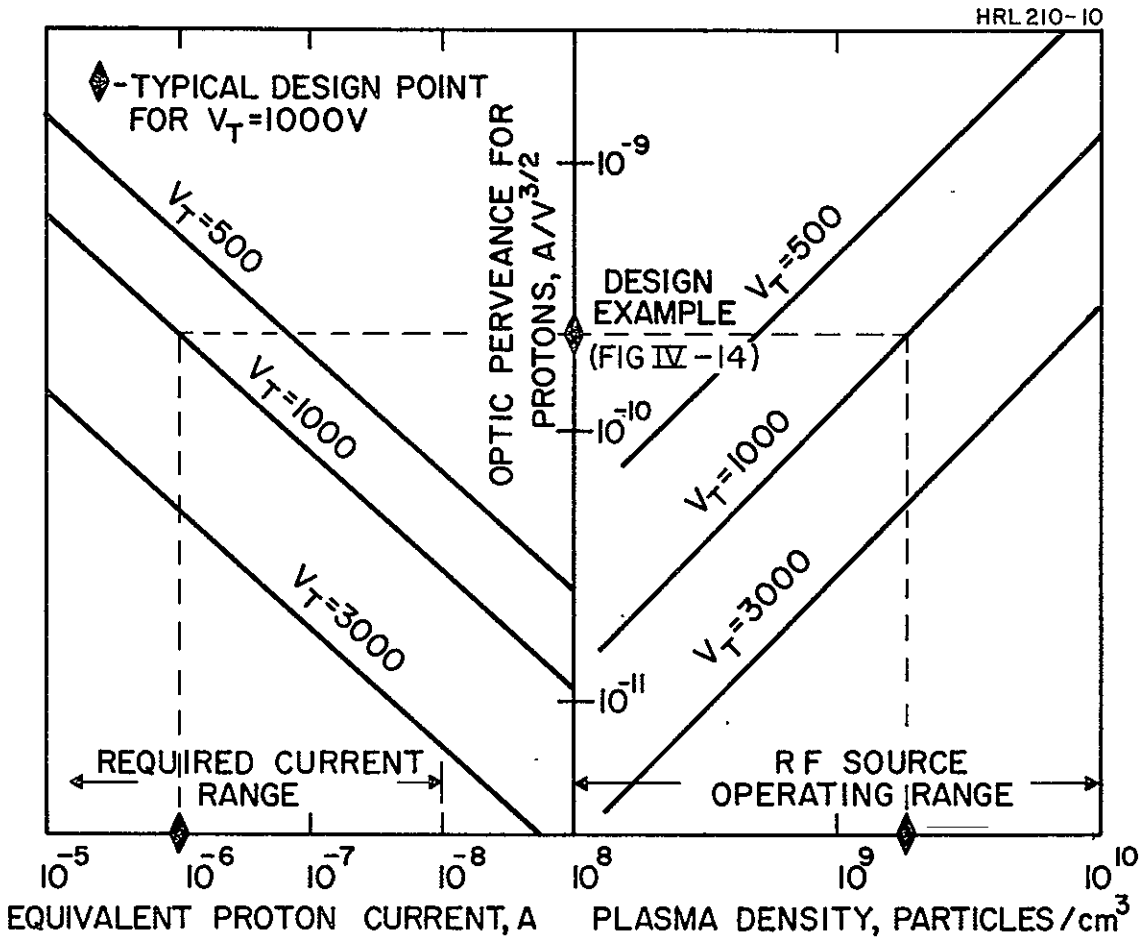

Fig. IV-15. Nomograph relating perveance, proton current and plasma density.

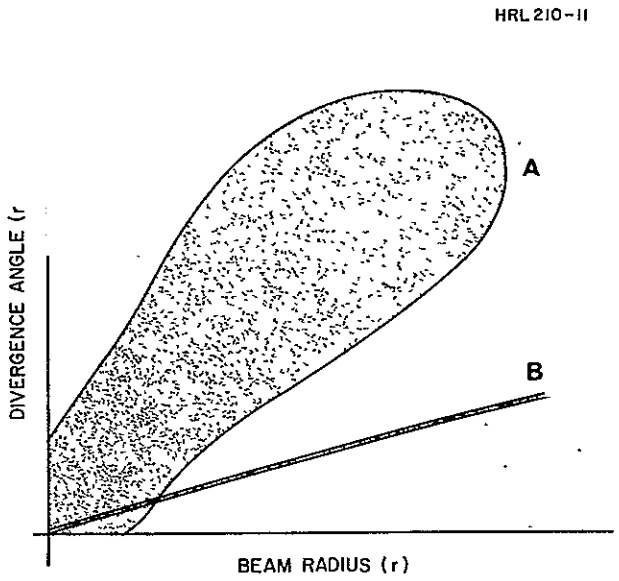

Fig. IV-16.
Emittance diagrams.

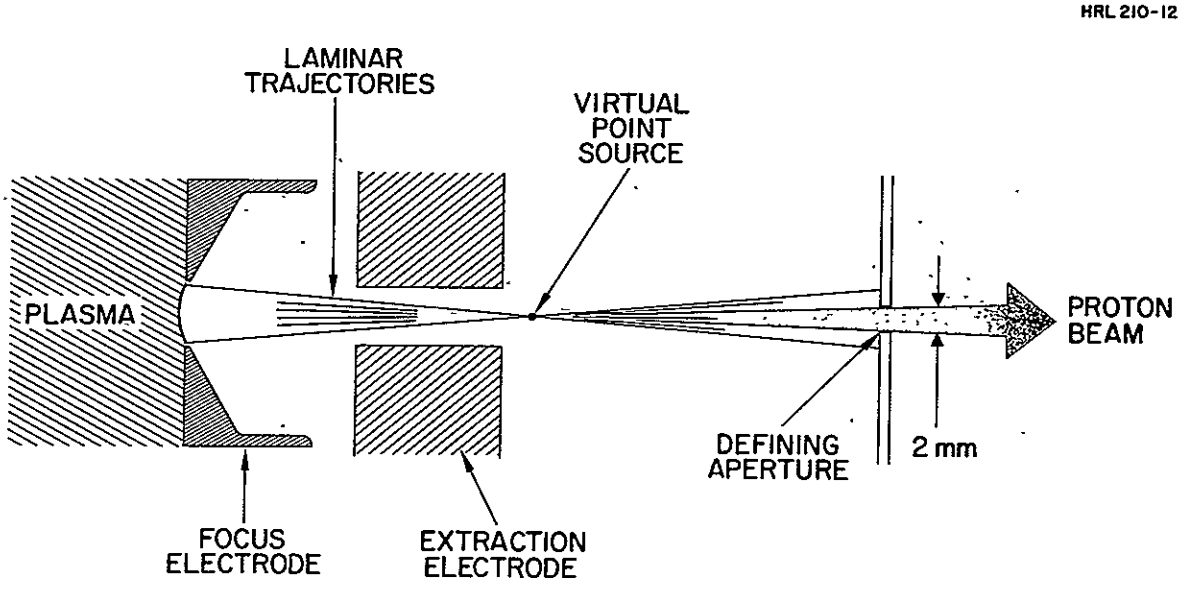

Fig. IV-17. Ion source used for trajectory calculations.

where K is a constant. This provides an ideal definition of the interface between proton source and beam transport system. Figure IV-18 shows the computer calculation of the emittance diagram of the proton source shown in Fig. IV-14 calculated just inside the extractor canal. The nearly laminar flow indicated from the diagram allows us to assume that these ions come from a point source downstream from the extractor canal, as shown in Fig. IV-17.

d. Accel-Decel Operation of Ion Extraction Systems

This simple, but important concept is often overlooked by those designing ion transport systems. An accel-decel system is illustrated schematically in Fig. IV-19. The ions are extracted with a total voltage V_T greater than the desired beam voltage V_B, and then decelerated. This accomplishes two things. First, as illustrated in Fig. IV-19, it prevents electrons from the beam or target from entering the source and damaging components or disturbing the control system which often operates on total emitted current. Second, it separates the extraction voltage from the beam voltage and permits a higher beam current to be extracted than would be possible at the beam voltage alone (see eq. (IV-1)). It also permits adjustment of the beam voltage without disturbing the position of the plasma sheath because V_T may be held constant as V_B is varied.

B. MASS SEPARATORS

1. Introduction

All of the ion sources discussed in Section IV-A produce an ion beam output which is a mixture of protons, H_2^+, H_3^+, and many other ions. The sources may also produce a high flux of fast neutral particles by charge exchange and a number of

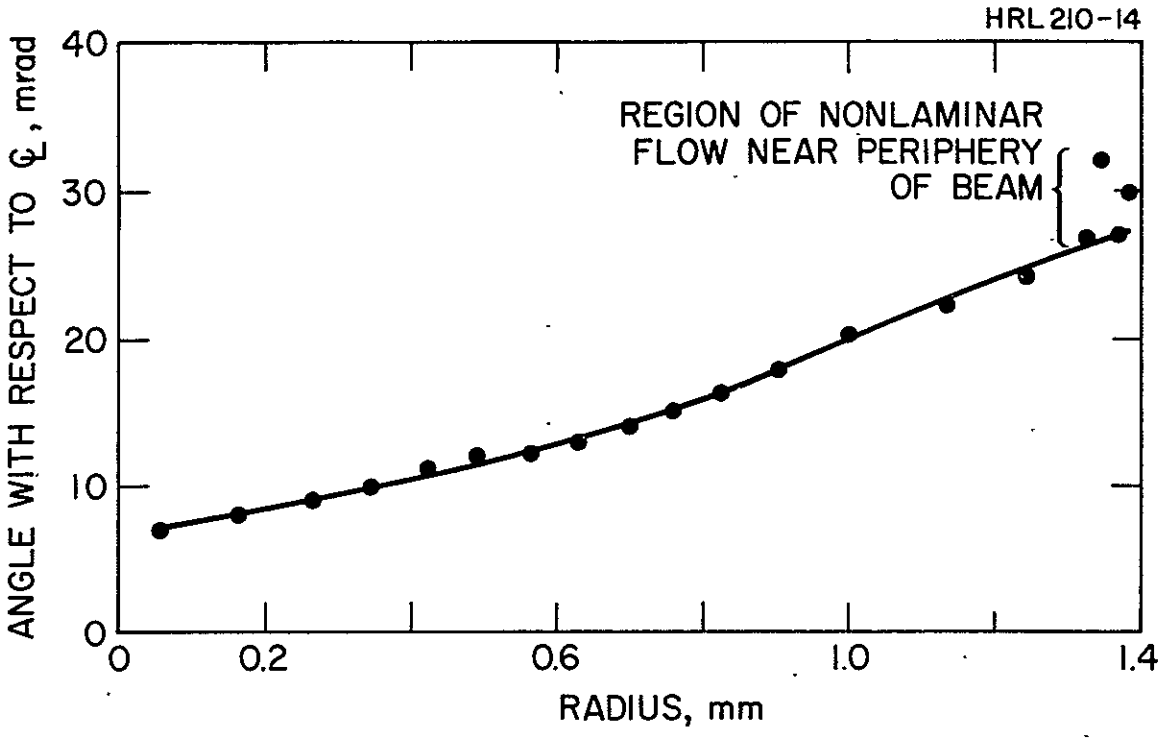

Fig. IV-18. Calculated perveance for ion gun shown in Fig. IV-17.

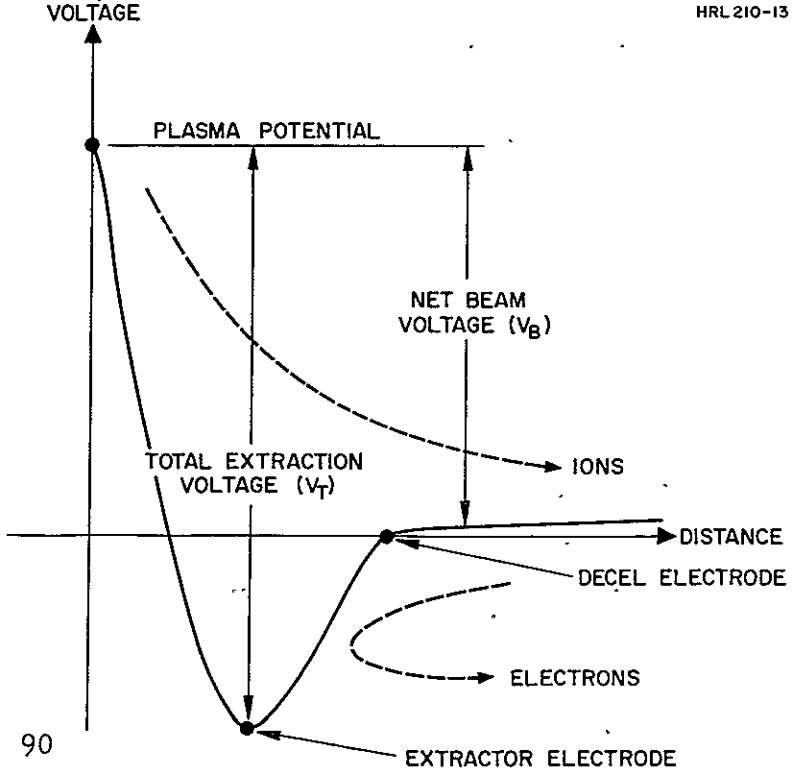

Fig. IV-19. Accel-decel extraction system.

ultraviolet photons which may degrade the test sample and complicate the current measurement by creating photoelectrons in the Faraday cup which monitors the beam. The mass separator, which is located between the proton source and the target, must purify the beam which passes through it so that only the protons will strike the target.

The physical separation of the protons from the rest of the beam can be accomplished in two basically different manners. An appreciation of the two concepts plays an important role in choosing the most desirable type of mass separator. In both techniques the starting point is a beam which is a mixture of protons, other positive ions, fast and slow neutral particles from the source, photons from the discharge within the source, plus any material which may be sputtered from the ion extraction system or focusing lenses. The first method is to design a separator which selects only the protons from this beam. The trajectories of the protons are controlled so that they alone reach the target, which is shielded from the source so that none of the contaminants may reach it by line of sight. The magnetic sector magnet is an example of such a device. The second system concept is to provide a series of filters to prevent the unwanted particles from reaching the target while permitting the desirable proton beam to pass. The difficulty here is first to identify all of the contaminants which may exist in the beam and then to devise filters which will selectively stop the contaminants but transmit the protons. This is particularly difficult in the case of photons and fast neutrals. The rf separator is an example of this type of system. As will be shown, a separator which deflects the proton beam is clearly superior for this application.

In order to provide a basis for comparing the various separators, the following characteristics are considered important:

1. Is the beam pure (no photons or fast neutrals transmitted)?
2. Is a large fraction of protons transmitted?
3. Is the transmitted beam continuous or pulsed?
4. Does the separator introduce aberrations into the beam?
5. Is the separator stable over a period of 1000 hours?
6. Is the separator easy to adjust and use?
7. Does the separator have excessive size, weight, or power requirements?
8. Does the separator accommodate a full range of ion velocities?

All types of separators involve an interaction between their electric and/or magnetic fields and the charge on the proton. They do not measure mass directly, but only the momentum or velocity of the particles which are presumed to have a uniform energy because they all originate from a single source at a fixed potential. If the source itself produces protons with a range of energies, this may cause the separator to defocus or otherwise disperse the beam. In other words, an energy dispersion in the original beam may appear as a spatial dispersion in the proton beam after it has traversed the separator. This is particularly important at low accelerating voltages. For example, a 50 eV energy dispersion in the beam is 10% of the total beam energy at 500 V (which is the lowest beam voltage considered here). For this reason, a low energy spread was made a requirement in selection of a suitable ion source.

Another important criterion in the selection of a separator is the size of the beam which it must accept. In general the design of any separator which deflects the proton beam increases in difficulty as the beam increases in size. This results primarily from the difficulties of maintaining the uniformity of the electric and magnetic fields in the separator over large areas. The larger gaps have greater fringing fields, and in the case of magnetic fields require much more power. Therefore, considerable effort was devoted to designing an ion optical system which transported a small beam through the mass separator and then expanded it to cover the target. Had this not been possible, the choice of optimum mass separator might well have been different.

Types of Mass Separators

Four general types of mass separators are described in this section.

a. Radio frequency — which utilizes resonance between particle inertia and an alternating electromagnetic field.
b. Homogeneous magnetic field — in which the ions are spatially separated due to their different radii of curvature in a magnetic field.
c. The crossed field or E x B — where perpendicular static electric and magnetic fields cause different trajectories for different masses.
d. Magnetic lens — which utilizes a current loop to form an ion lens that projects images of different masses at different points.

a. Radio Frequency

The basic concept of a linear rf mass spectrometer was first described by Bennett (Ref. IV-26). The operation has been analyzed by a number of authors, particularly Redhead and Crowell (Ref. IV-27), who list all the critical performance parameters for both sinusoidal and square wave operation.

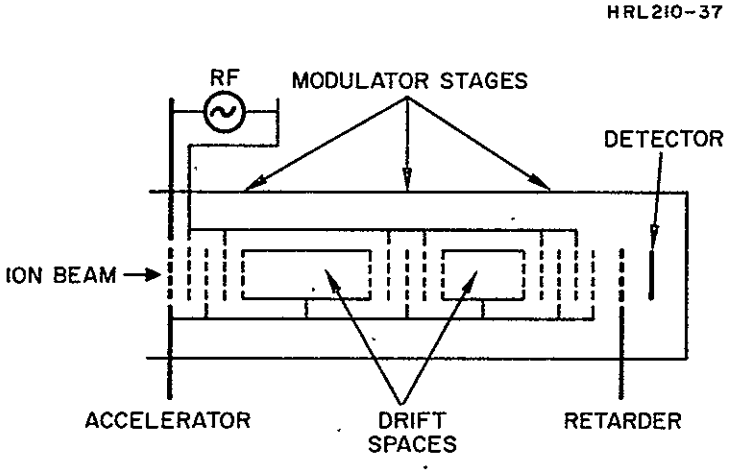

Fig. IV-20. Radio-frequency mass analyzer schematic.

Basically a monoenergetic beam of ions is accelerated into an rf electrode system consisting of a series of plane parallel equidistant grids (see Fig. IV-20). Alternate grids are grounded and the other grids have applied to them an rf voltage which is small compared with the initial accelerating voltage. If the transit time of an ion between the two grids is approximately 0.4 of the rf period, the ion will remain in synchronism with the rf field. There is one time during each cycle when an ion may enter the rf field and gain more

energy than any other. By judicious choice of drift spaces between several rf sections, the energy gain of this particular ion may be enhanced. The ions emerging from the rf sections encounter a dc retarding potential barrier which stops all but the most energetic ions. Thus, only the synchronous ion is able to reach the target. The mass of this ion is

$$M_i = 0.266 \frac{V}{\ell_g^2 f_o^2} . \qquad \text{(IV-3)}$$

where

$M_i \equiv$ ion mass, atomic units
$V \equiv$ particle accelerating voltage, volts
$\ell_g \equiv$ grid separation, centimeters
$f_o \equiv$ oscillator frequency, megahertz.

Other properties of this device are calculated in detail by Redhead and Crowell (Ref. IV-27). They show that higher resolution may be obtained by using square waves rather than a sinusoidal rf signal; however, the former is much more sensitive to grid spacing than sinusoidal operation.

The experimental performance for a system of this design has been reported recently (Ref. IV-28). This device has 13 grids, three rf stages, and two drift spaces. The complete system is 25 cm long and operates at 10 MHz. Assuming that each grid is 95% transparent but that the individual wires are randomly oriented with respect to those of the other grids, approximately 50% of the particles from the source will impinge on the grids. The effect of the separator on the remaining beam which traverses the separator may be established from data presented in Ref. IV-28 and is summarized in Table IV-3 and Fig. IV-21.

TABLE IV-3

Performance of RF Spectrometer[a]

Condition	Current to target, A		H^+ as Percent of beam	Percent of H^+ Transmitted
	H_1^+	H_2^+		
Source only	1.4×10^{-10}	1.2×10^{-10}	54	100
RF on	$4.4 \times 10^{-}$	5.0×10^{-11}	47	32
Retardation 100 V	1.5×10^{-11}	1.4×10^{-12}	91	11
Retardation 110 V	1.2×10^{-11}	5×10^{-13}	96	8.5

[a]From Ref. IV-28.

Figure IV-21 illustrates that while the beam may be purified to greater than 95% by this technique, it can be done so only at the expense of reducing the transmission to less than 10%. This in itself may be quite tolerable if a source with a sufficiently high output current is used. The difficulty arises because the photon output from the source and the beam of fast charge exchange neutrals created at the source aperture are not attenuated by the electric fields. Thus they are increased in relation to the proton beam by at least an order of magnitude using this type of separator. The effects of these contaminants may thus easily be greater than those of the proton beam for many operating conditions. A further complication is that the impurity beam may not be uniform over the target area and is very difficult to measure accurately.

Therefore, even though this system has many advantages in terms of minimum energy dispersion, astigmatism, cost, and size, it is suggested that serious consideration be given to the problems of beam contamination before it can be used for any simulation. It should also be noted that the output

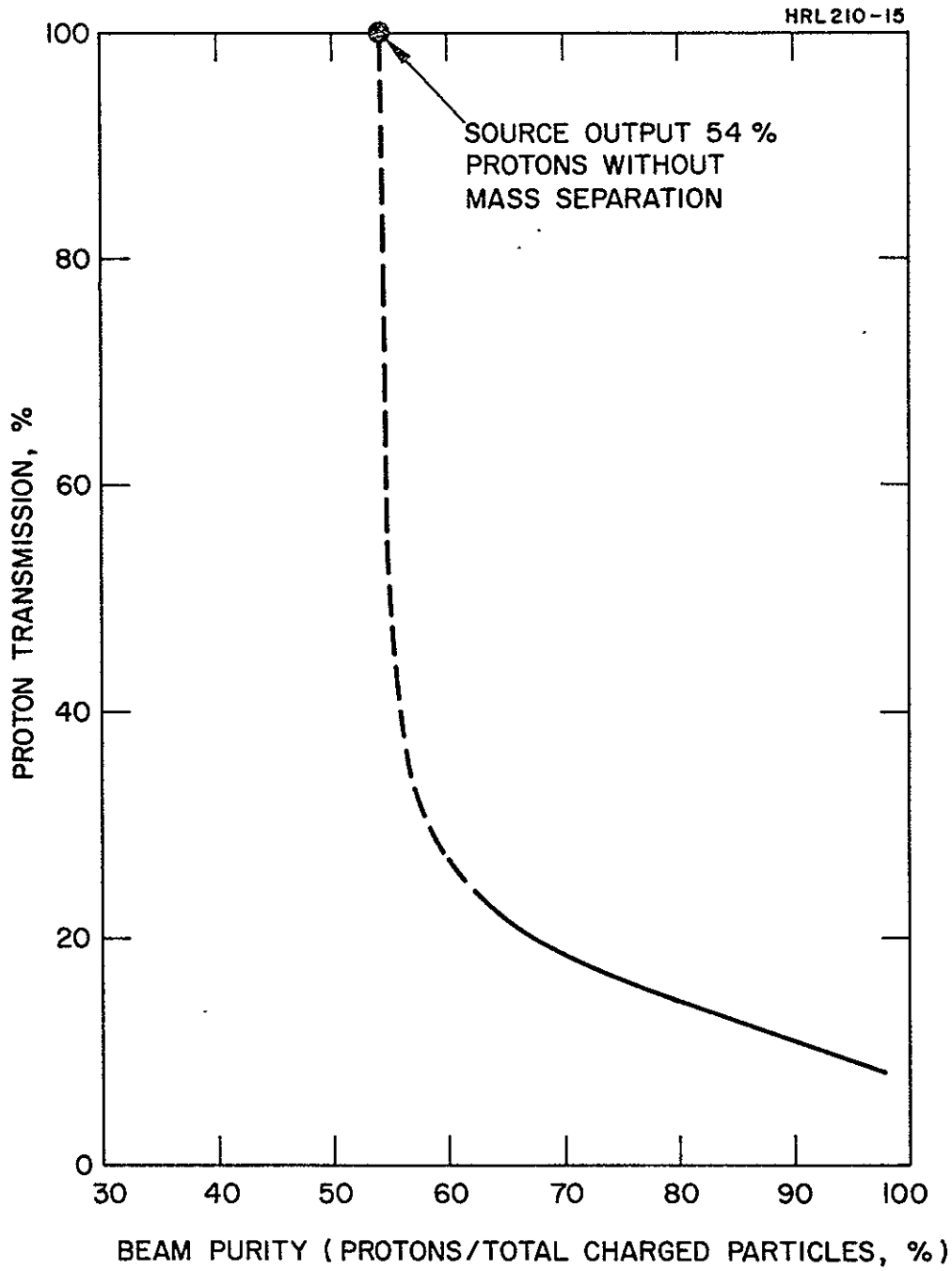

Fig. IV-21. Proton transmission as a function of beam purity for a typical rf source (Ref. IV-28).

from this separator is pulsating at the driving rf frequency (nominally 10 MHz). As discussed in Appendix A, this is not expected to present a difficulty in accurately simulating solar wind damage to thermal control coatings.

b. Magnetic Separator

This is a "conventional" type of mass separator which operates on the principal that the trajectory of a charged particle will be deflected by a magnetic field. The basic equations are those for the kinetic energy of the particle

$$\text{kinetic energy} = eV = \frac{mv^2}{2} \qquad \text{(IV-4)}$$

and the force exerted on a particle in a magnetic field

$$\text{force} = evB = \frac{mv^2}{r_i} \qquad \text{(IV-5)}$$

or

$$r_i = \frac{mv}{eB} = \frac{\text{linear momentum}}{eB}$$

which may be solved to yield

$$\left(\frac{2mV}{eB^2}\right)^{1/2} \qquad \text{(IV-6)}$$

$$r_{H^+} = [144.5\ (V^{1/2})(B^{-1})] \text{ for protons} \qquad \text{(IV-6a)}$$

where

$r_i \equiv$ radius of curvature of the path of the ion i, centimeters

$B \equiv$ magnetic field, gaus

As shown in Fig. IV-22, particles which originate from a single point, but which have different momentum (either mass or velocity) will have different radii of curvature in the magnetic field.

A great deal of developmental work has been devoted to understanding and improving this type of mass spectrometer. Much of this sophistication is not required to achieve the relatively simple task of separating mass one from masses two and three at low energy. An excellent review of the design details of this type of separator has been compiled by Inghram and Hayden (Ref. IV-29). Only those facts pertinent to the current design will be reviewed here.

Of primary importance to the over-all system performance are two parameters of the separator design. The first is the angle through which the beam of interest (protons) is deflected. It is directly related to the strength of the magnetic field and the path length in the field. The second factor is the dispersion of the various masses at the target. This defines the physical separation of the various mass species at the focal plane of the separator.

For simple systems the radius of the proton beam curvature is made coincident with the apex of the magnetic sector, and the entrance and exit angles (ε_1 and ε_2) are made zero. This makes the deflection angle, Φ equal to the sector angle, θ. (see Fig. IV-23). The linear deflection of the beam may then be readily calculated. The radial contour of the magnet gap and the entrance and exit angles (ε_1 and ε_2) are often chosen to be nonzero to improve the focusing properties of the separator (Ref. IV-30). In some designs the pole faces on the entrance and exit sides are themselves curved. Both conditions obviously affect the total deflection of the beam. The main criterion of importance here is that the proton beam be physically removed from the undeflected neutral beam; this is a very loose boundary condition and is easily fulfilled.

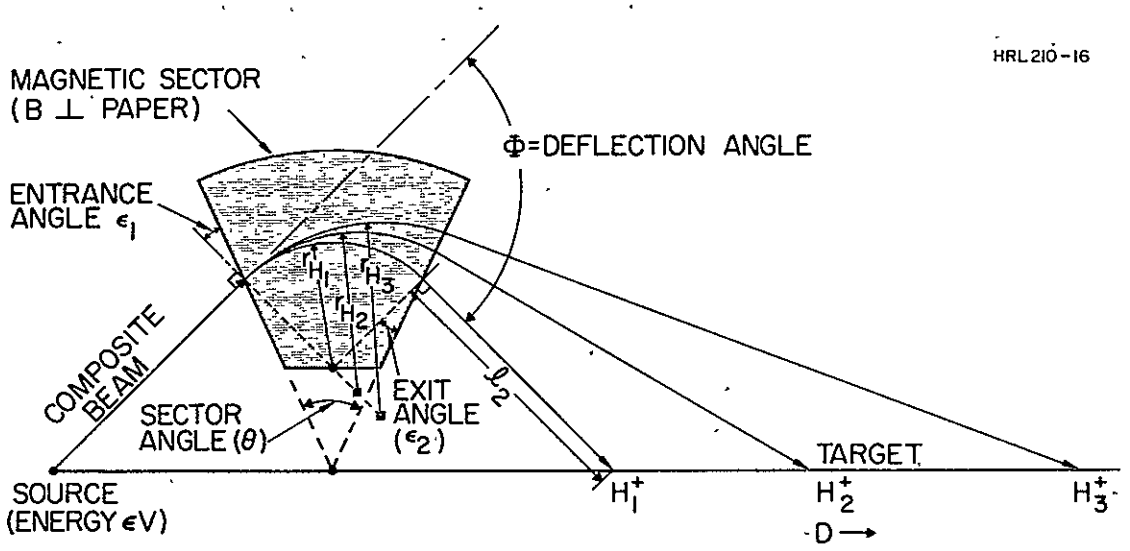

Fig. IV-22. Magnetic sector used as a mass separator.

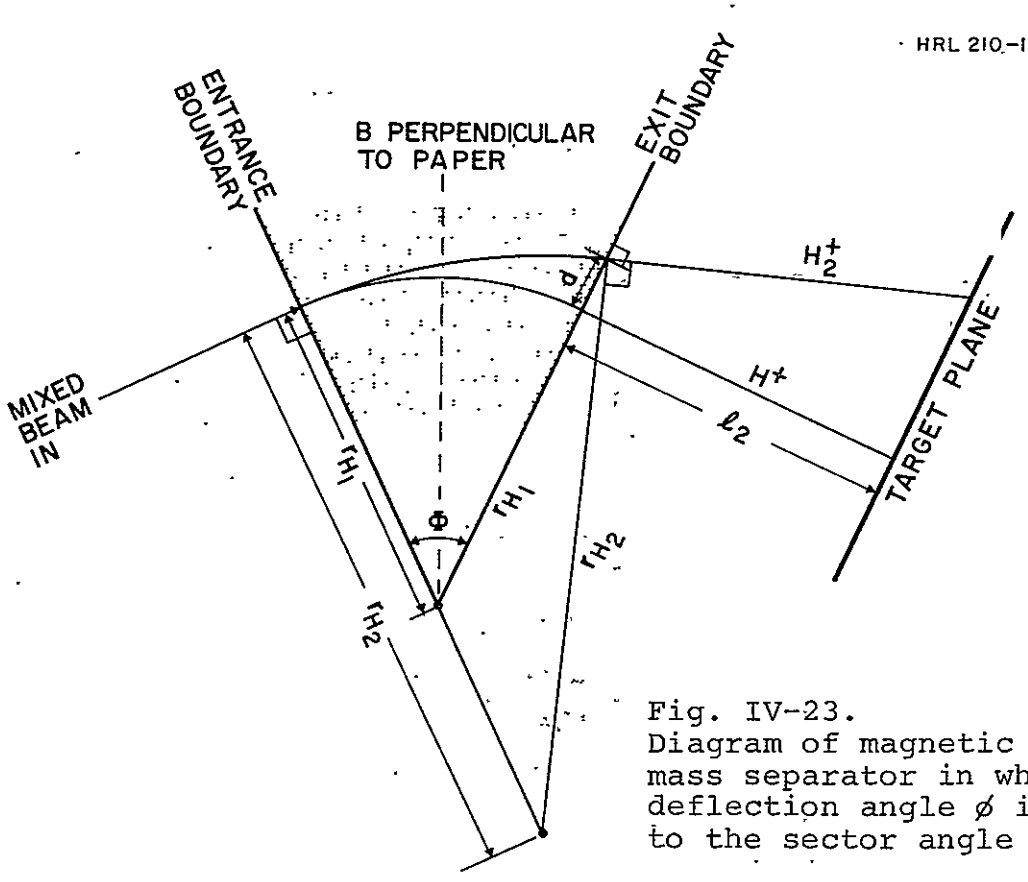

Fig. IV-23.
Diagram of magnetic sector mass separator in which the deflection angle ø is equal to the sector angle θ.

The dispersion may be derived from the fact that the lateral distance between images formed by particles of different momenta emitted from the same object point is proportional to the momentum difference which is in turn proportional to the radius of curvature of the trajectories. Hence the dispersion is:

$$D = K \frac{\Delta p}{p} = k \frac{\Delta r_i}{r_i} . \qquad \text{(IV-7)}$$

An approximate expression for the constant in the dispersion relation is

$$K = r_{H_1} (1 - \cos \phi) + \ell_2 [\sin \phi + (1 - \cos \phi) \tan \varepsilon_2] \qquad \text{(IV-8)}$$

where

ϕ	$\equiv$	deflection angle of the ion
r_{H_1}	$\equiv$	radius of proton trajectory
ℓ_2	$\equiv$	object distance
ε_2	$\equiv$	exit angle (may be zero or adjusted to reduce astigmatism).

As an example, for $r_{H_1} = 15$ cm, $\ell_2 = 30$ cm, $\theta = 60°$, and $\varepsilon_2 = 0$, we have

$$D = 33.5 \frac{\Delta p}{p} . \qquad \text{(IV-9)}$$

For a fixed energy, the momentum of H_2^+ is 1.4 times that of H^+; therefore, $\Delta p/p = 0.4$, making the dispersion between the H_1^+ and H_2^+ beams 14 cm.

Because the dispersion depends on the ratio of two momentum values, a spatial separation will occur as a result of a difference in velocity (i.e., energy) of the similar ions as well as a difference in mass. Thus any energy spread in

the initial beam will affect the size of the beam as it traverses the separator. The particular case of a separator with r_{H_1} = 15 cm separating protons and H_2^+ with an energy spectrum of 1000 ± 25 V (i.e., a 50 V energy spread) is shown in Fig. IV-24. The displacements are measured 20 cm from the exit plane. Figure IV-24 also illustrates the accuracy of the approximate formula as compared with an exact numerical calculation.

In order to preserve the minimum beam size, the dispersion through the separator should be minimized. A curve such as that of Fig. IV-24, may thus be used to establish the minimum sector angle for the separator which will spatially separate the proton beam from the H_2^+ beam. This minimum angle will also minimize the beam size.

Thus far we have discussed only the mass separating properties of this concept. Because the separator also acts as an element in the beam transport system (Ref. IV-31), some consideration of its focal properties is important as well. Three design philosophies are possible:

1. direction focusing — focusing of ions homogeneous as to mass and velocity but of different initial direction
2. velocity focusing — focusing of ions homogeneous as to mass and direction but with different initial velocity
3. double focusing — focusing of ions homogeneous in mass but of varying velocity and direction.

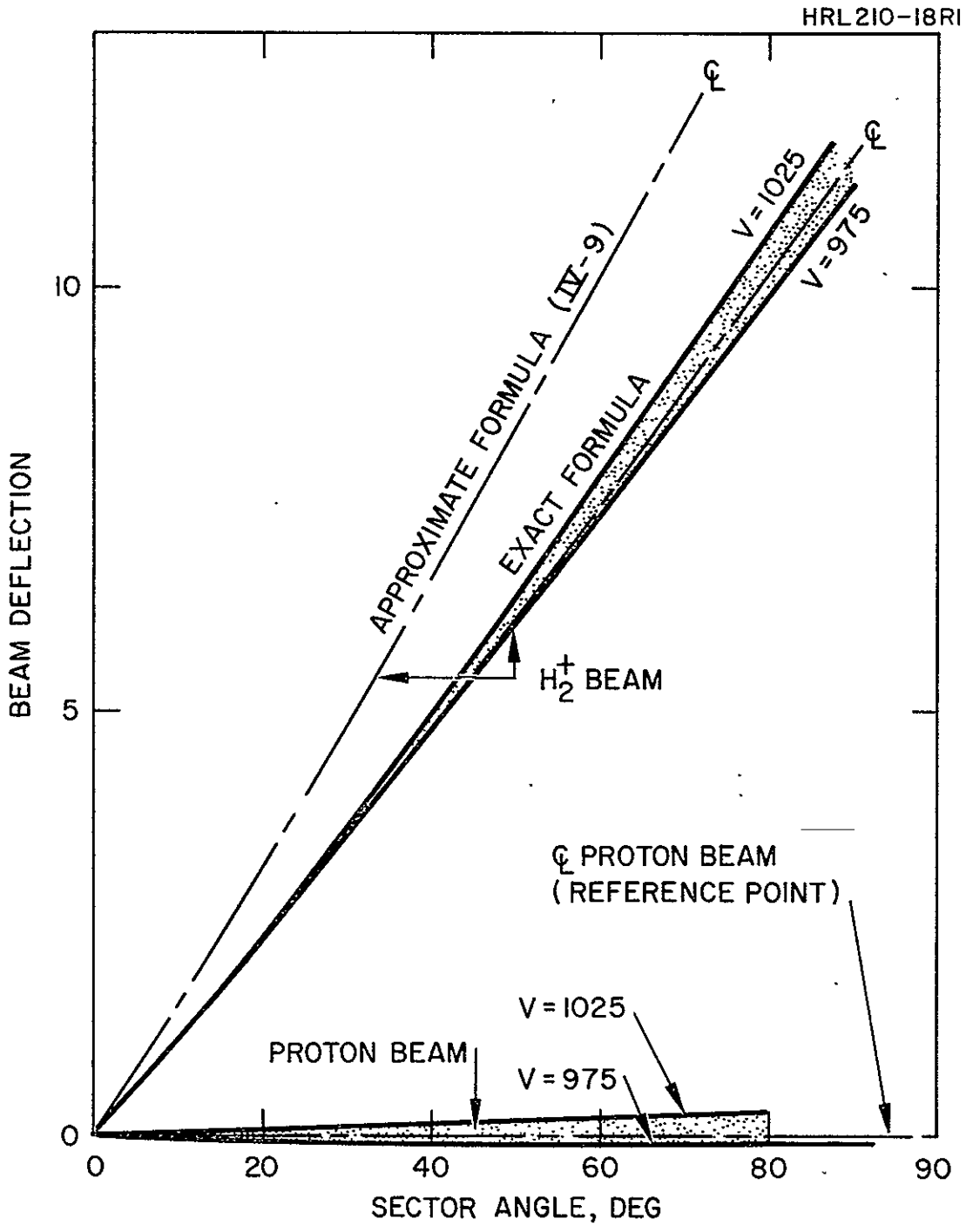

Fig. IV-24. Beam deflection measured 20 cm from exit plane as a function of sector angle for magnetic separator for r_{H_1} = 15 cm, V = 1000 ± 25.

For this application, item 2 is most important, particularly if the ion source has an appreciable spread in ion creation energy. Direction focusing is less important because of the lenses at the source and object positions adjacent to the separator. A general treatment of this subject is beyond the scope of this report. References IV-29 and IV-31, plus the work of Sternheimer (Ref. IV-30), serve as general references for this area.

An additional term encountered is "first order focusing," which means that aberrations which are a first order function of mass are, by design, made equal to zero by adjusting the shape of the magnetic pole faces, the entrance and exit angles, and the radial variation in magnetic field strength. Higher order focusing is possible but generally reserved for use with large beams or where extremely high resolution is required. Prior to construction of an actual separator, the exact ion trajectories for the chosen design would be computed as in Section IV-C to validate the design.

In summary, the magnetic sector mass separator is well suited for this task, provided that the beam is kept small in diameter until after separation and then expanded or scanned to cover the target area (see Section V). The power requirements increase rapidly as the beam size and hence the magnet gap increase. The magnetic fringing fields also become very difficult to adjust at large gap spacings, thus introducing unwanted aberrations in the final beam. This type of separator accomplishes the two necessary functions of bending the proton beam to physically remove it from the efflux of photons and neutrals from the ion source (which travel line of sight), and of dispersing the charge particles of various masses so that a pure proton beam results. Care must be taken in the design to reduce the ion optical aberrations and to minimize the dispersion due to the energy distribution in the ion source.

c. Crossed Field Separators

Consider a system in which the magnetic field B, the electric field $\mathcal{E}$, and the velocity of a charged particle are all mutually perpendicular. If the signs are properly chosen it is clear that by adjusting the magnitudes of the electric and magnetic field strengths, the electric and magnetic forces on the particle may be made equal and opposite and the particle trajectory will be unchanged. This is illustrated for mass m_1 in Fig. IV-25. Particles with the same kinetic energies but a different mass m_2 will follow a curved trajectory. The properties of this type of separator have been discussed by Bleakney and Hipple (Ref. IV-32) and later by Ogilvie and Kittredge (Ref. III-33). For the purpose of this report, the simplified analysis of Wahlin (Ref. IV-34) more clearly illustrates the important processes.

As before, the velocity of an ion which has been accelerated through a voltage V is

$$v = \left(\frac{2eV}{m}\right)^{1/2} \qquad \text{(IV-10)}$$

An ion with a mass m_1 and velocity v_1 will not be deflected when moving through the velocity filter shown in Fig. IV-25 if

$$Bev = e\mathcal{E} \qquad \text{(IV-11)}$$

or

$$B\left(\frac{2eV}{m_1}\right)^{1/2} = \mathcal{E}. \qquad \text{(IV-12)}$$

Ions of a different mass m_2 experience a force

$$\frac{m_2 v_2^2}{r_i} = ev_2B - e\mathcal{E} \qquad \text{(IV-13)}$$

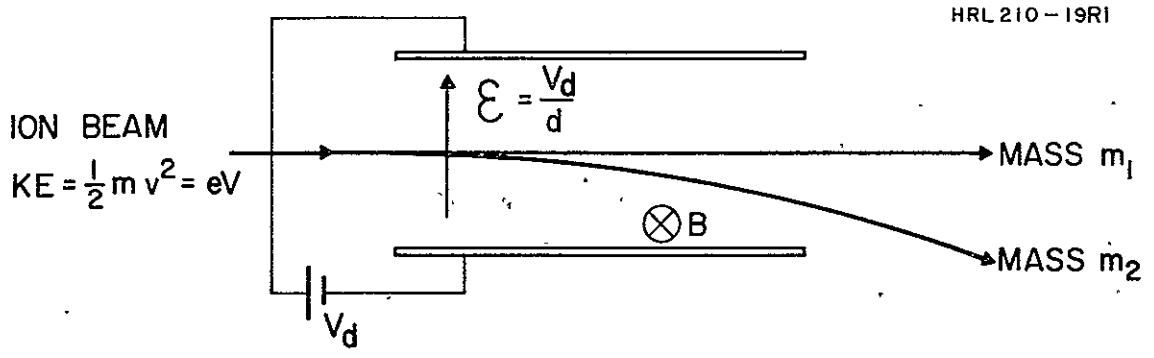

Fig. IV-25. Schematic of E x B mass separator.

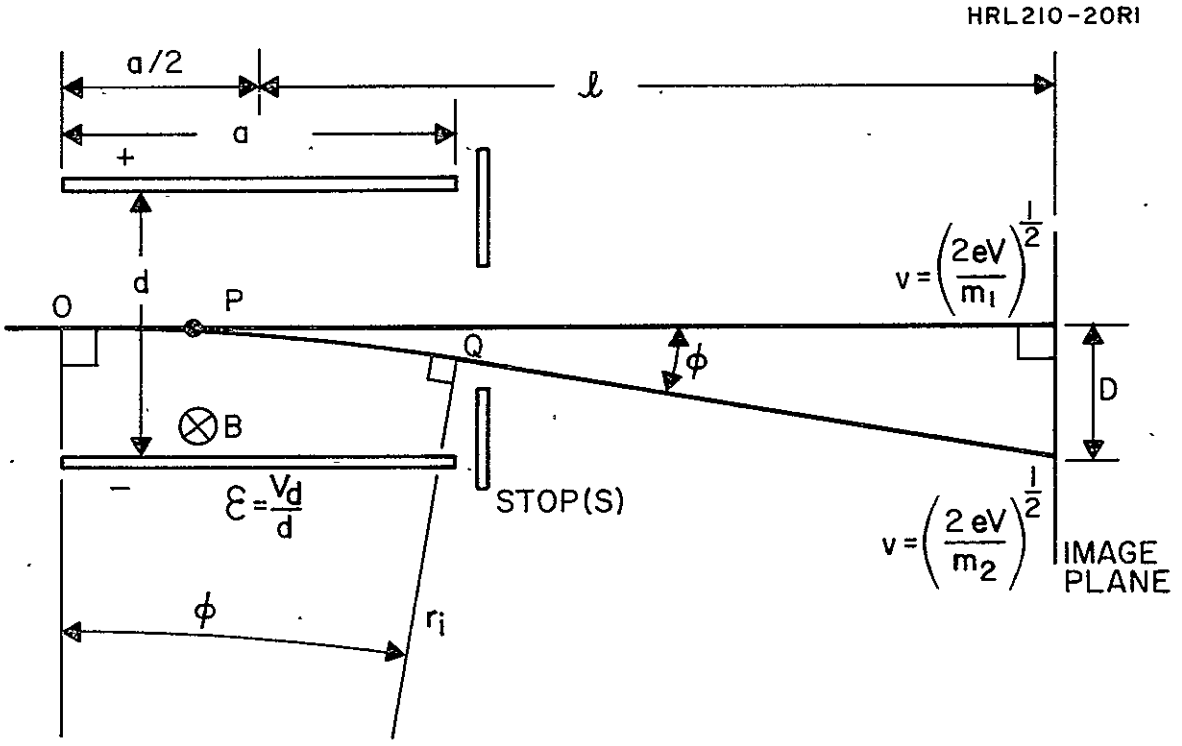

Fig. IV-26. Diagram used to derive eq. (IV-16).

or

$$\frac{m_2 v_2^2}{r_i} = e\mathcal{E}\left[\left(\frac{m_1}{m_2}\right)^{1/2} - 1\right] \qquad \text{(IV-14)}$$

by direct substitution from (IV-11) and (IV-12).

Therefore, the ions of mass m_2 are deflected in a circular path with radius

$$= \frac{2V}{\mathcal{E}\left[\left(\frac{m_1}{m_2}\right)^{1/2} - 1\right]} \qquad \text{(IV-15)}$$

This equation is a good approximation for small deflection angles.

If r_i is known, the dispersion may be calculated geometrically from Fig. IV-26. Because the deflected beam is perpendicular to the radius of curvature at both the entrance point (0) and the exit point (Q), the deflection angle and the arc traversed by the particle in traveling from 0 to Q are both equal to Φ. For small angles where Φ can be approximated by a/r_i, the dispersion

$$D = \frac{\ell a}{r_i} = \frac{\ell a \mathcal{E}}{2V}\left[\left(\frac{m_1}{m_2}\right)^{1/2} - 1\right] \qquad \text{(IV-16)}$$

where a is the length of the filter and ℓ is the distance to the image plane. The condition for no deflection of a selected mass number comes directly from (IV-12)

$$m_1 = 2 \cdot V \cdot \left(\frac{B}{\mathcal{E}}\right)^2$$

For the application here we desire that the proton beam be deflected out of the main beam of photons and neutral effluent from the source. Thus we let the protons be represented

by m_2 in Fig. IV-26 and choose Φ large enough that a stop at the exit from the separator prevents line of sight transmission from the source along the proton beam. D must also be large enough to separate the protons from the charged particles with masses two and three.

It is possible to choose a unique ratio of $\mathcal{E}/B$ which provides adequate deflection of the proton beam and which provides cancellation of first order aberrations as well. From (IV-13) and (IV-16),

$$D = \ell a B \left[\frac{e}{2Vm}\right]^{1/2} - \frac{\ell a \mathcal{E}}{2V}.$$

Therefore, the first order dispersion (dD/dV) is zero for $\mathcal{E}/B = (qV/2m)^{1/2}$. By choosing the fields with this criterion the dual requirements of a net deflection and zero first order aberrations may be achieved.

This type of separator will serve equally as well as the simple magnetic sector in many cases. The extra variable of the electric field strength $\mathcal{E}$ provides the opportunity to design the system to achieve first order focusing. A primary difficulty arises in the design of the electrostatic field shaping pole pieces to generate a uniform field. This design is difficult because the magnetic poles, which are immediately adjacent must be made of metal and thus perturb the electric field shapes. Available commercial designs generally employ segmented shims with adjustable voltages on each to shape the electric fringing fields. These require a complicated empirical adjustment. It was this uncertainty in design that led to the choice of the magnetic sector over the crossed field separator in the example design in Section V. Current studies at HRL under another program indicate that it should be possible to shape the electric poles to accomplish this desired field without shims. This has not yet been verified experimentally.

d. Magnetic Lens

The fact that the focal properties of a magnetic lens are a function of the mass of the charged particles which pass through it may be used to purify the proton beam. The resultant system is somewhat crude compared with the magnetic sector or the crossed field separators, but it is also much less expensive and therefore may be useful in some unique applications.

In its most elementary form a magnetic lens is simply a current loop through which the beam of charged particles passes (Ref. IV-35). The equation of the focal length of the magnetic lens is

$$f = 1.80 \times 10^5 \frac{MVr_c}{(NI)^2} \qquad \text{(IV-17)}$$

where

$f \equiv$ focal length, centimeters
$r_c \equiv$ coil radius, centimeters
$NI \equiv$ coil ampere turns
$M \equiv$ particle mass, amu
$V \equiv$ particle potential, volts.

This type of lens is widely used in electron optics (particularly in electron microscopes) because of its low aberration. It has found little use in ion optics because, as shown in (IV-17), the magnetic field required for a given focal length increases with both the mass and the energy of the incident particle. Thus, the application here which involves low velocity ions of the lightest possible mass is rather unique.

As shown in Fig. IV-27, a magnetic lens may be used to selectively focus only the protons from a divergent monoenergetic beam. The heavier particles may be stopped as shown in the figure. This concept is practical only because the particles to be separated differ in mass by a factor of two, thus making the focal length for H_2^+ double that of the protons. The factor by which the H_2^+ component of the beam is reduced is nominally equal to the ratio of the area of the H_2^+ beam in the plane of the aperture to the aperture area itself. Assuming that the coil radius r_c is just large enough to accommodate the beam at distance ℓ_1 from the source, it may be shown that the percent of H_2^+ transmitted (for 100% H_1^+ transmission) is given by

$$\frac{1}{\beta} = (2x-1)^2 \left[(x-1)^{-1} + \left(\frac{r_c}{r_a} - \frac{1}{x-1}\right)\left(1 - \frac{x-1}{2x-1}\right)\right]^2 \qquad \text{(IV-18)}$$

where

$x = \ell_1/2f_H$

$\beta = H_2^+$ (after separator/H_2^+ (before separator)

$f_H \equiv$ proton focal length (i.e., M = 1 in (IV-17)

$r_c \equiv$ coil (and beam) radius

$r_a \equiv$ aperture radius.

This function is plotted in Fig. IV-28. The number of ampere turns in a simple coil required for a specific set of typical conditions is shown in Fig. IV-28. Note that a significant reduction in ampere turns may be achieved by designing the magnetic lens with shaped pole pieces and a ferromagnetic yoke.

From the above discussion it is clear that attenuation of the H_2^+ beam by a factor of 10 to 100 is quite practical for typical conditions. Considering that the H_2^+ content in the beam may originally be of the order of only 10% to 20%, this represents an adequate purification for normal purposes.

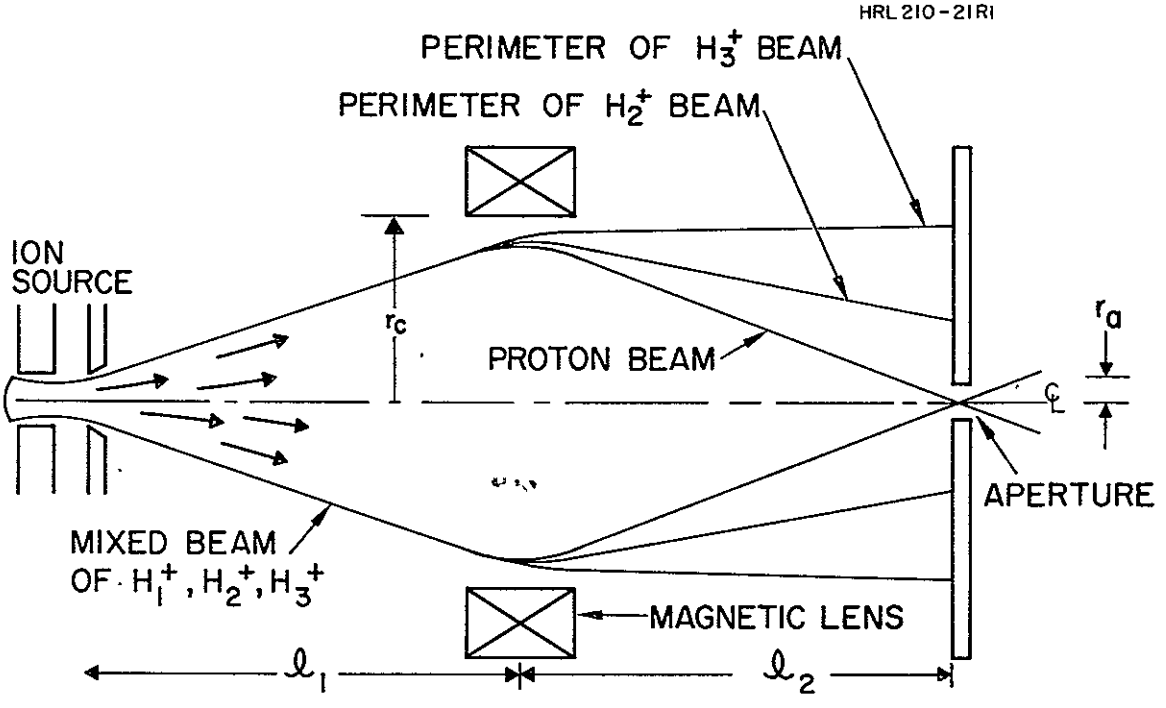

Fig. IV-27. Schematic of magnetic lens mass separator.

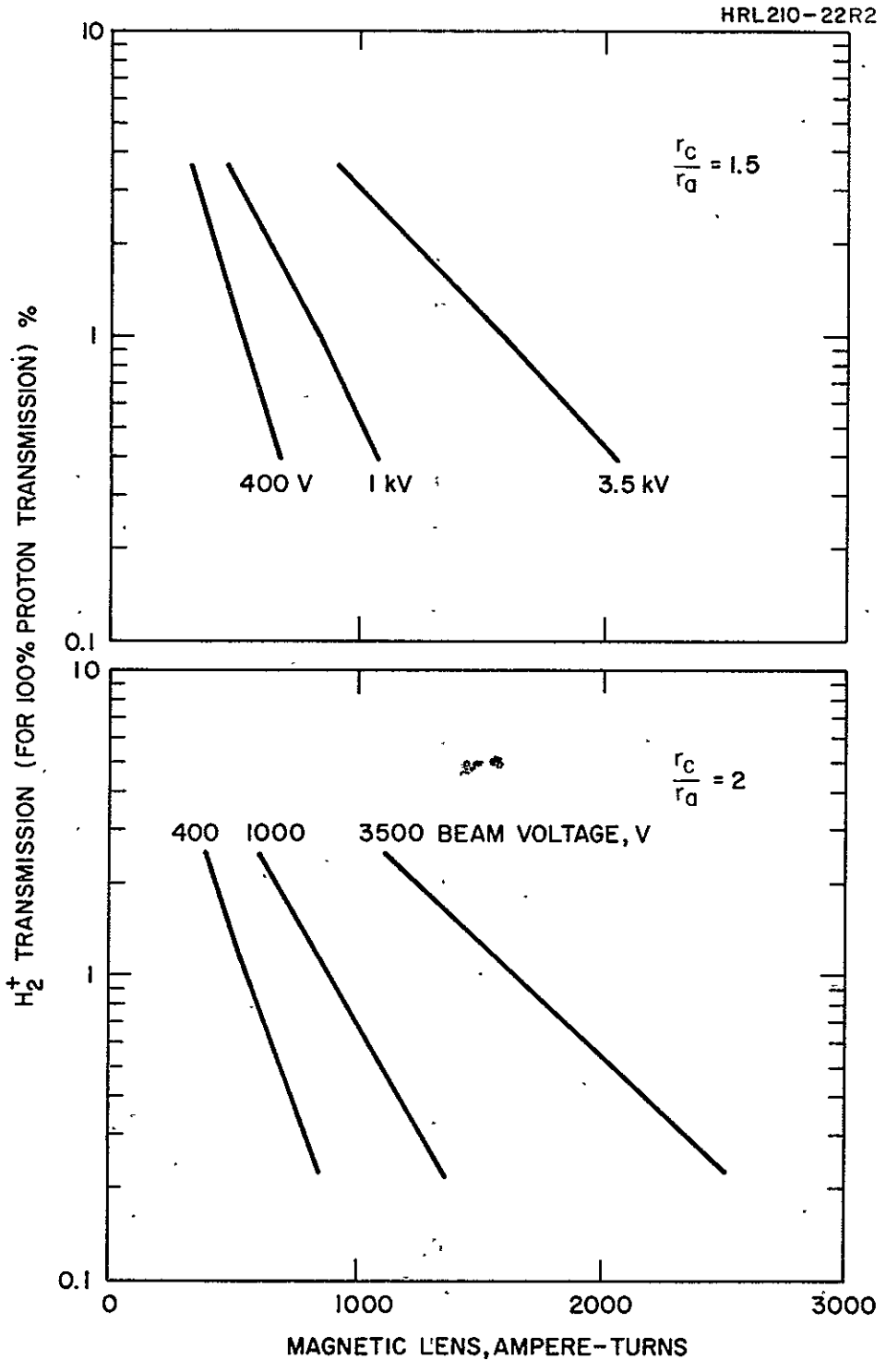

Fig. IV-28. Attenuation of H_2^+ with magnetic lens separator.

There is a disadvantage of this system, however. As shown in Fig. IV-27, neutral particles and photons from the source can reach the target. This can be eliminated by placing a small stop on-axis to block the solid angle subtended by the aperture at the source. This will depress the axial current density at the target and produce a somewhat "hollow" beam. The extent of this depression must be determined experimentally. It might mean that the axial sample position was not usable, or it might serve simply to flatten the beam profile, which is normally peaked in the center. It is possible to reduce the current density at the target by simply defocusing the proton beam so that some protons will be stopped by the aperture plate as well. A computer analysis of the trajectories has demonstrated that for the energy range required here, approximately a factor of three attenuation is possible before the beam shrinks to less than 10 cm diameter at the target. An additional lens presumably could extend this range.

While many features of this system appear attractive, a primary disadvantage for this survey is that no report of its implementation has been found in the literature.

3. Selection of the Mass Separator

The properties of the four types of mass separators discussed above are summarized in Table IV-4. Of the four, only the rf separator is clearly rejected because it does not prevent uncharged particles and photons from striking the target. The magnetic lens is a relatively simple but untried system. The remaining two — the sector and crossed field separators — are similar in many respects. The crossed field separator contains aberrations from nonuniformities in both the electric and magnetic fields, while only a magnetic field

is present in the sector. In particular, it is difficult to generate a uniform electric field when the magnetic and electric pole pieces of the crossed field separator must of necessity be in close proximity. This problem has recently been solved analytically and appears manageable for low energy applications such as that required for the present program.

The sector magnet was chosen over the crossed field device for the system design here principally because it requires one less power supply and is a well understood, proven device. Techniques have been derived to produce very sophisticated instruments of this type if they are required. Special attention should be devoted to the defocusing of the beam due to energy dispersion in the source. Careful design of both source and separator can keep this well within tolerable limits.

C. BEAM TRANSPORT SYSTEM

1. Introduction

The beam transport system must accept the ion beam from the source, focus it through the mass separator, and expand it to 10 cm diameter at the target plane. It must also be capable of providing adjustment of beam intensity by a factor of 1000. Finally, it must perform satisfactorily over the full range of proton energies from 0.5 to 3.0 kV. Two general concepts are possible. The first is to extract from the source a small, relatively high current density beam which is expanded in size only after it has passed through the mass separator. This considerably simplifies the design of the einzel lens because all the beam ions pass through the lens near the axis where aberrations are small and the paraxial ray equation is valid. The mass separator is simplified as

TABLE IV-4

Mass Separators

Type	Transmission, %	Beam Purity %	Transmits Charge Exchange	Beam Size	AC or DC Transmission	Focusing Aberrations	Size, Power Weight, etc.	Advantages	Disadvantages
Radio Frequency	8.5 @ 96 10.5 @ 91 12.5 @ 87 14 @ 80		Yes	Any	AC at mega-hertz Duty Cycle 10%	No focusing or aberrations	Light Small Short Requires ac and dc power	• Handles large beam • Small size • Low total power • Easy intensity adjustment	• < 100% purity • Low transmission of protons • Transmits fast charge exchange neutrals • Must trade beam purity for transmission • Photons from source strike target
Magnetic Sector	Approaches 100	100	No	Small to Medium	DC	Can focus Has aberrations	Heaviest Single power supply	• Pure beam • High transmission • Compatible with scanned beam	• High power for large beam • Energy dispersion
Crossed Electric and Magnetic Fields	Approaches 100	100	No	Any (small easier)	DC	Has aberrations Can focus	Small Light Requires two power supplies	• Pure beam • Will take large beam	• Two power supplies • Electric and magnetic aberrations
Magnetic Lens	> 80	95	No	Small	DC	Small aberrations Center dark spot Does focus	Small Short Light Single power supply	• Simplest system • Compatible with scanned beam • Intensity adjustment possible	• Center dark spot • < 100% purity

FOLDOUT FRAME 1

FOLDOUT FRAME 2

well because the magnet gap widths can be minimized. The single small aperture in the source serves to minimize the effluent hydrogen gas and the pumping speed necessary to maintain satisfactory chamber pressure. Finally, the small beam permits a series of apertures to be installed between the source and the main vacuum chamber, to reduce the diffusion of hydrogen from the source into the chamber. A separate pump is provided near the source.

The second approach is to extract a large beam from the source and transport this broad beam through the mass separator to the target. This virtually eliminates the need for an ion optical system, but entails a number of other difficulties which are obvious from the preceding paragraph. The only mass separator which readily accommodates a broad beam is the rf separator, although large aperture crossed field and even magnetic sector separators are possible at the low beam energies used here. This latter type of system has been described by Lebduska (Ref. IV-28). Only the first type of system (i.e., small beam) will be treated here.

2. Computer Simulation of Ion Trajectories

As the name implies, each element in the ion optical system may be treated mathematically by techniques used in conventional geometrical optics. For instance the einzel lenses have an equivalent thick lens analogy, and a sector magnet is equivalent to a cylindrical lens bounded on the entrance and exit sides by thin lenses. The focal properties of the lenses are a complicated function of the geometry, beam voltage, and lens voltage for each.

It has been shown (Ref. IV-36) that where the paraxial ray equation is applicable this problem may be readily treated by a matrix technique which is easily adaptable to computer calculation. Assuming circular symmetry, the trajectory of a particle may be defined at any time by its radial distance r from the axis of the ion optical system (which is the z axis) and radial momentum represented by the column vector

$$\begin{pmatrix} r \\ r'\sqrt{V} \end{pmatrix}$$

where $r' = dr/dz$. The effect of each ion optical element on the trajectory is represented by a two by two matrix so that

$$\begin{pmatrix} r \\ r'\sqrt{V} \end{pmatrix}_{out} = \begin{pmatrix} a_{11} & a_{12} \\ a_{21} & a_{22} \end{pmatrix} \begin{pmatrix} r \\ r'\sqrt{V} \end{pmatrix}_{in}$$

where the a's are functions of the dimensions and voltages of the ion optical system. The total transfer matrix for the entire system is thus a product of n matrices, where n is the number of ion optical elements in the system. It is clear that this formulation is ideal for computer calculation.

In practice the transfer matrix for each type of element in the system is first written analytically and then stored in the computer in functional form. Next a program is written which first assembles the series of matrices in the proper sequence to represent the sequence of elements in the system. Next the physical dimensions of the elements, the particle voltage, and the focusing voltage for each lens are put into the matrices and the multiplication is carried out in the computer to calculate the trajectory of the particle. The

coordinates of the particle at each point are printed out and the entire trajectory is drawn automatically by a Calcomp plotter tied to the computer output.

Using this technique, individual variables may be checked rapidly and the performance of the system verified under a number of operating conditions. Of the order of 80 such parametric investigations were made during this program.

A block diagram of the final system is shown in Fig. IV-35. In the computer simulation the individual components are treated as discussed below.

a. Source

For all of the systems studied we have characterized the source by the emittance diagram shown in Fig. IV-29). Thus under this assumption the ions appear to originate from a point source 7.7 cm upstream of the aperture (assumed to be 2 mm in diameter), as shown in Fig. IV-30. Figure IV-29 was derived from a computer study of an extraction system described in Section IV-A-1-b and shown in Fig. IV-14.

b. Drift Space

All the lens elements are separated by unipotential drift spaces characterized by the following matrix:

$$\begin{pmatrix} r_{out} \\ r'_{out}\sqrt{V} \end{pmatrix} = \begin{pmatrix} 1 & \ell_d/\sqrt{V} \\ 0 & 1 \end{pmatrix} \begin{pmatrix} r_{in} \\ r'_{in}\sqrt{V} \end{pmatrix}$$

where ℓ_d is the length of the drift space. This matrix expresses the fact that a ray passing through a drift-space has the same exit and entrance angles and leaves with a change in length given by the length of the drift space times the entrance slope. Physically a drift space is a field free region.

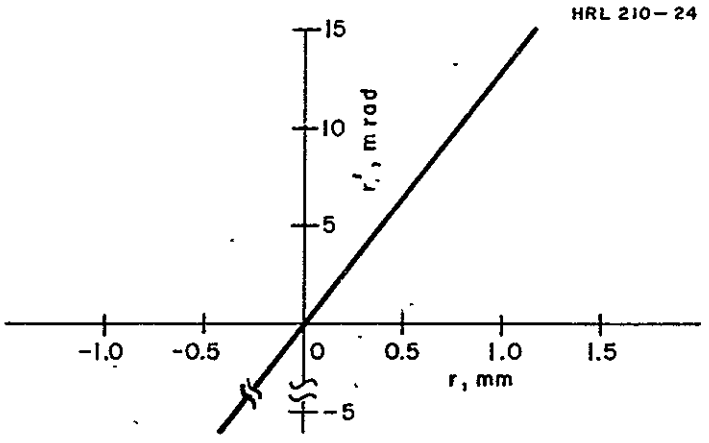

Fig. IV-29. Ion source emittance diagram.

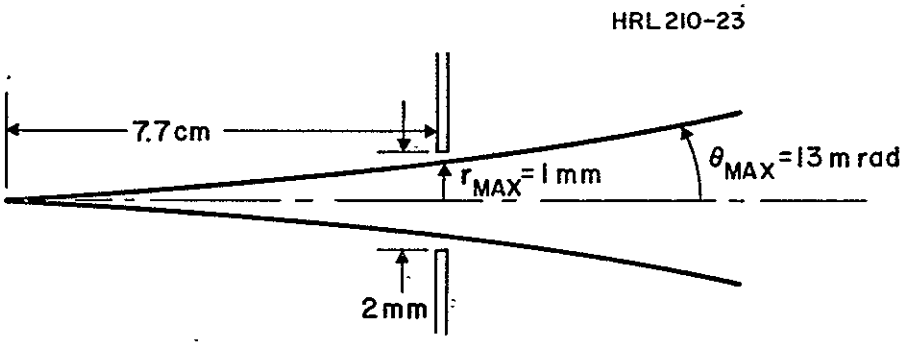

Fig. IV-30. Dimensions of ion beam emanating from source.

c. Accelerator

The accelerator is the first lens element following the source and is used to decelerate the beam so that the beam potential at the exit of the accelerator is at system ground potential. Thus, the extraction-accelerator system is an accel-decel system which prevents the back-bombardment of the source by secondary electrons created downstream of the accelerator. A potential diagram showing the variation of the potentials to change the beam energy at the target is shown in Fig. IV-31. With this arrangement the target and all the lens elements (except the central element of the einzel lens) downstream of the accelerator are always at ground potential. The beam energy is changed by adjusting both the source and extractor voltages and keeping the plasma-extraction voltage at either 3500 V or 1750 V, depending on the target energy range required. The accelerator chosen for this study consists of two apertured plates separated by a distance d. By application of the Davission-Calbick thin-lens equation (Ref. IV-37) both the exit and entrance apertures, it may be shown that this lens element has the following matrix representation (V_1 and V_2 are the potentials on the entrance and exit plates, respectively):

$$M_{Acc} = \begin{pmatrix} \dfrac{3\sqrt{V_1} - \sqrt{V_2}}{2\sqrt{V_1}} & \dfrac{2d}{\sqrt{V_1} + \sqrt{V_2}} \\ \dfrac{3(V_2 - V_1)[\sqrt{V_1} - \sqrt{V_2}}{8d\ V_1 V_2} & \dfrac{3\sqrt{V_2} - \sqrt{V_1}}{2\sqrt{V_2}} \end{pmatrix}$$

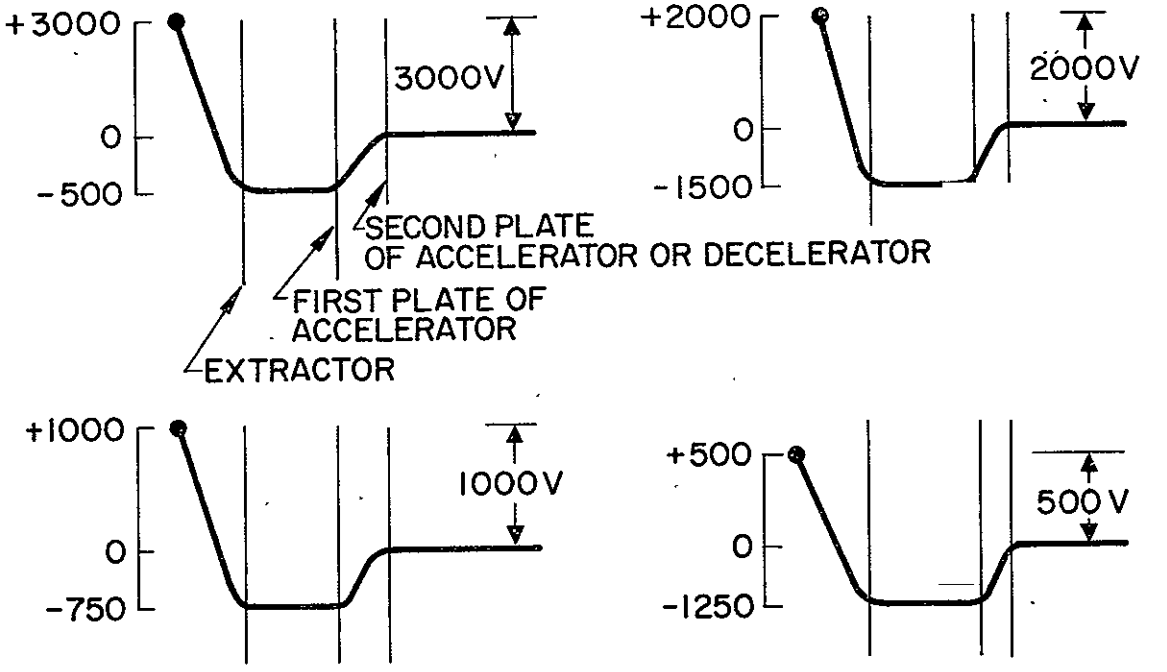

Fig. IV-31. Accel-decel modes of ion extraction system operation.

d. Mass Separator

The advantages and disadvantages of four basic types of mass separators are compared in Section IV-B. The sector magnet chosen for this system has a radius of curvature r_{H_1} of 15 cm and a deflection angle of 20°. The design is stigmatic or double focusing so that the same amount of focusing is present in both the horizontal and vertical planes. One way this can be accomplished is by using a tapered pole piece design (see Fig. IV-32) (Ref. IV-38) where the normalized field gradient in the median plane varies as

$$B_z = B_o\left(\frac{r}{r_{H_1}}\right)^{-1/2}$$

where $B_o = B_z$ at $r = r_{H_1}$. For this case Ref. IV-38 shows that the transfer matrix for a 20° sector is

$$M_{sect} \begin{pmatrix} \cos\frac{\pi}{9}\frac{1}{\sqrt{2}} & \frac{r_{H_1}\sqrt{2}}{\sqrt{V}}\sin\frac{\pi}{9}\frac{1}{\sqrt{2}} \\ \frac{-\sqrt{V}}{r_{H_1}}\sin\frac{\pi}{9}\frac{1}{\sqrt{2}} & \cos\frac{\pi}{9}\frac{1}{\sqrt{2}} \end{pmatrix}$$

e. Electrostatic Lenses

Only electrostatic lenses are considered here because they consume no power and are independent of the mass of the particle being focused. The most versatile type is the einzel lens which is composed of three apertures, or cylinders, as shown in Fig. IV-33. The two end elements are connected together electrically so that the beam leaves the lens with the same kinetic energy with which it entered. The central element is biased to retard the beam (i.e.,

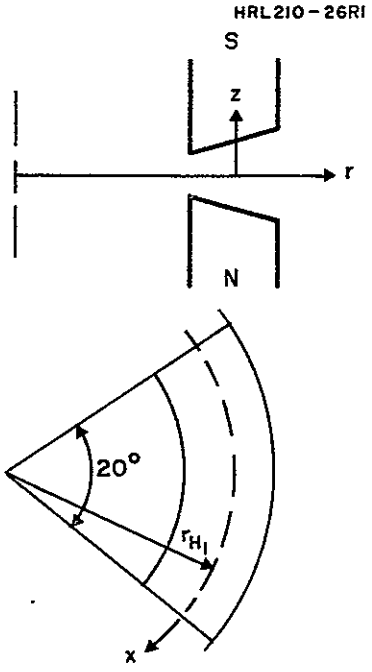

Fig. IV-32.
Detail of magnetic sector used in trajectory calculations.

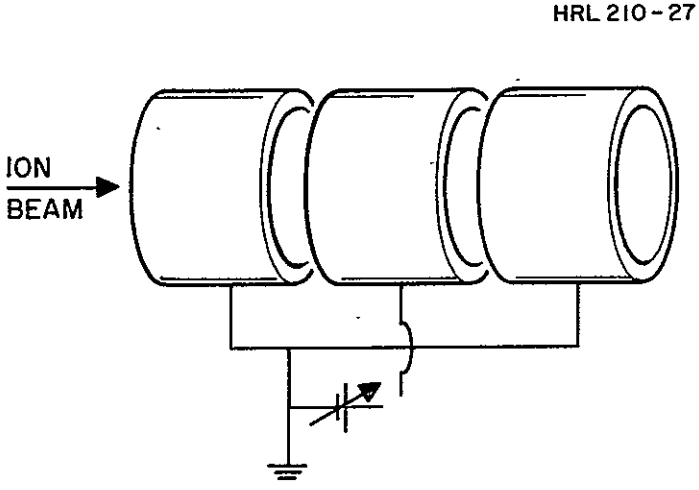

Fig. IV-33.
Einzel or unipotential lens.

biased positively for positive ions). The focal length of the lens is a direct function of the ratio of the voltage on this central element to the beam voltage. While such lenses are simple in concept, they introduce sizable aberrations if the beam diameter is greater than 1/3 of the lens aperture diameter.

Three einzel lens are used in the beam transport system for focusing purposes. The first, in conjunction with the weak focusing properties of the mass separator, focuses the beam through the aperture following the mass separator. This aperture also provides the pressure differential needed between the target and source chambers. The second lens produces a magnified image of the aperture, resulting in a 10 cm diameter image at the target. The third lens (optional) provides the slight collimation needed to produce an exactly parallel beam at the target. Without this optional einzel lens the long distance from the second einzel lens to the target produces a maximum angle of $\tan^{-1}$ (5/100) ≈ 2.7 deg. The geometry of these lenses, along with the experimentally measured focal length taken from Ref. IV-39, is shown in Fig. IV-34. The transfer matrix for a lens with focal length f, object distance ℓ_o, and image distance ℓ_i is given by

$$M_{Ein} = \begin{pmatrix} 1 - \frac{\ell_o}{f} & \frac{\ell_i \left(1 - \frac{\ell_o}{f}\right) + \ell_o}{V} \\ -\frac{\sqrt{V}}{f} & 1 - \frac{\ell_i}{f} \end{pmatrix}$$

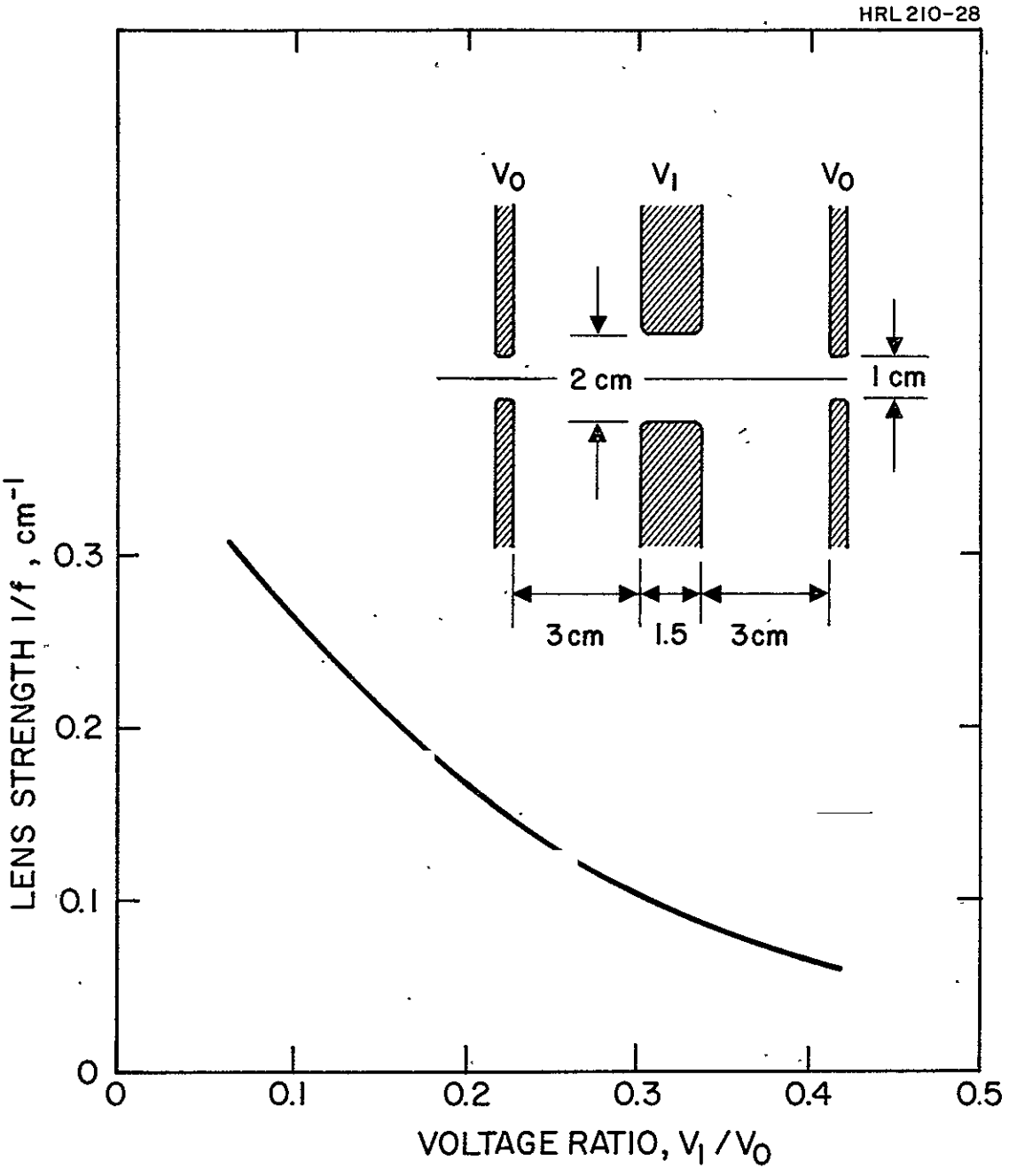

Fig. IV-34. Einzel lens strength as a function of voltage ratio (from Ref. IV-39).

For the above einzel lens it was found that the focal length corresponding to the lens strength of Fig. IV-34 could be closely approximated by

$$f = \exp\left[1.03 + (V_1/V_o)\ 3.22 + 2.85\ (V_i/V_o)\right].$$

This expression for the focal length was programmed into the expression for the transfer matrix so that the einzel lens voltage ratio could be used on an input variable to the computer program.

3. Design of Beam Transport System

A sketch of the final system is shown in Fig. IV-35. In this sketch the ion beam diameter has been drawn in a much larger size than its true proportions in order to make clear the ion optics effects. The focusing properties under various operating conditions are illustrated with the Calcomp computer plots described above. For all the trajectory plots described below, only rays leaving the source with positive angles are plotted, since the system is axially symmetric. In addition, for clarity, only the outer beam edge trajectory is shown in most cases. The operation of these ion optical elements is now described qualitatively and illustrated with trajectory plots: The diverging rays from the source are given a slight convergence by the lens action of the accelerator, which has a strength proportional to the decelerating voltage applied. The focusing voltage on the first einzel lens is then adjusted so that the rays enter the mass separator with the proper height and slope so that only the protons pass through the mass separator and are focused through the aperture with the proper entrance condition for the second einzel lens. Figure IV-36 shows the effect on the outer beam

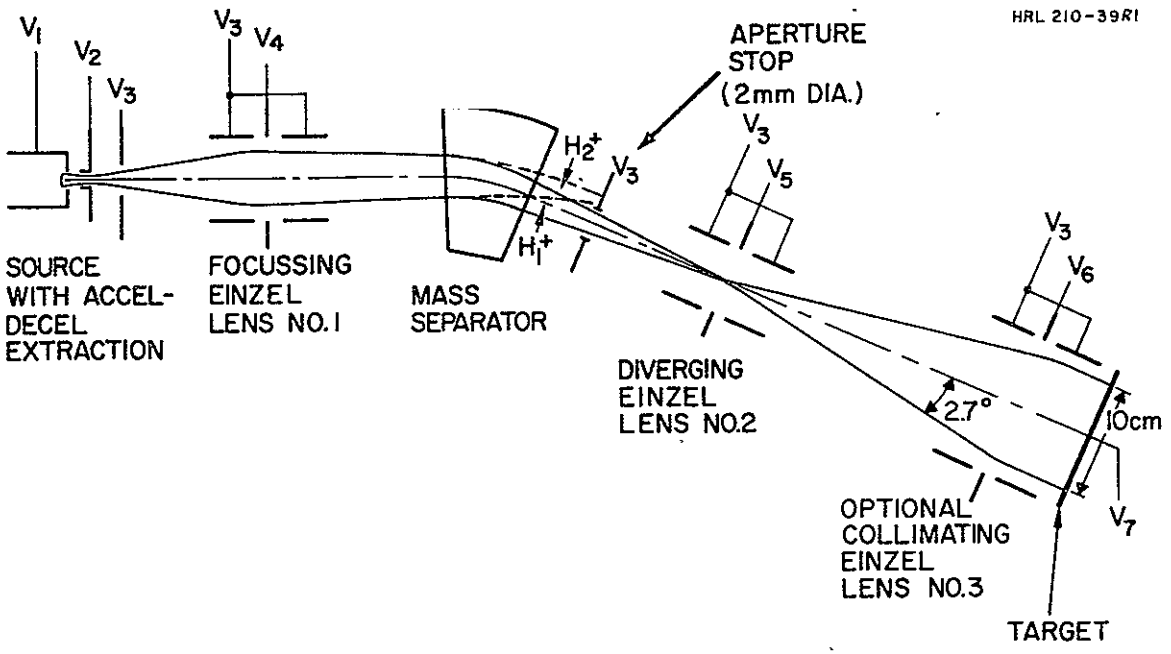

TYPICAL OPERATION[a]

Proton Energy	V_1	V_2	V_3	V_4	V_5	V_6	V_7
One Equivalent Sun							
500 V	500	-1250	0	400	465	375	0
1000 V	1000	- 750	0	800	930	750	0
3000 V	3000	- 500	0	2400	2825	2250	0
100 Equivalent Suns[b]							
500 V	500	-1250	0	310	460	375	0
1000 V	1000	- 750	0	605	920	750	0
3000 V	3000	- 500	0	1855	2800	2250	0

[a]All voltages measured with respect to ground (target at ground).

[b]Source provides additional factor of 10 intensity variation.

Fig. IV-35. Schematic of complete system.

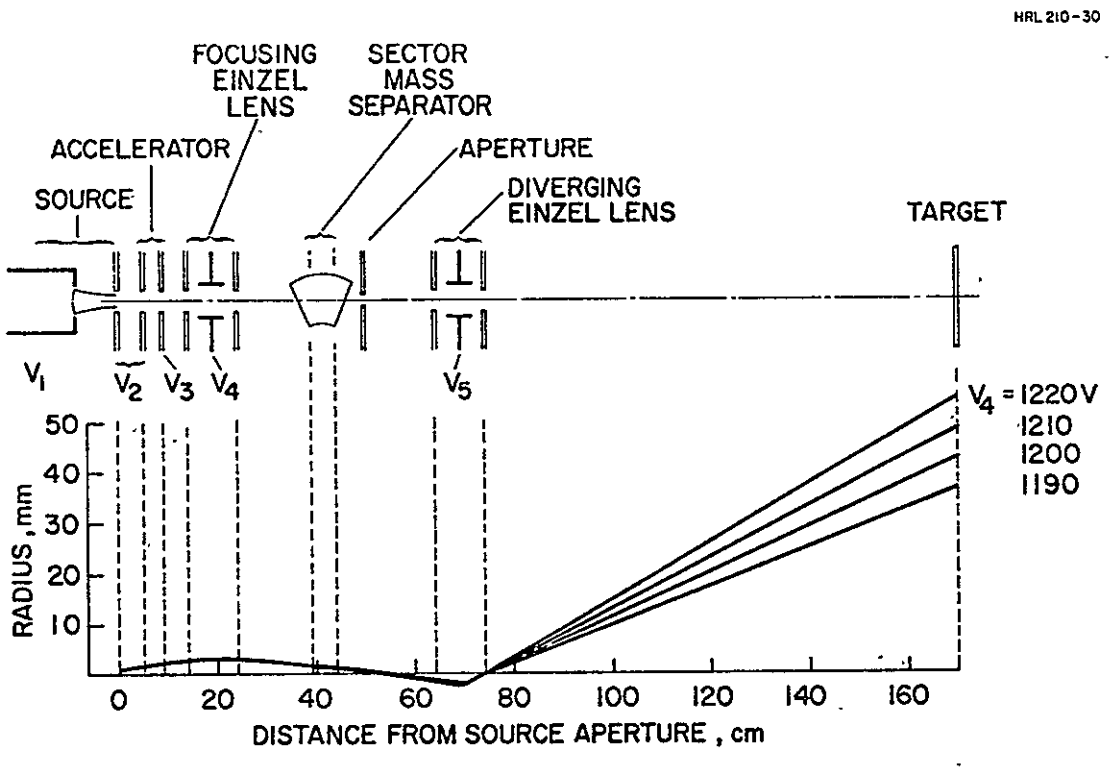

Fig. IV-36.
Computer generated trajectories showing effect of changing the focus einzel lens focusing voltage V_4 for constant extraction voltage of 3500 V and beam voltage of 2000 V with constant diverging einzel focusing voltage of V_5 = 1840V.

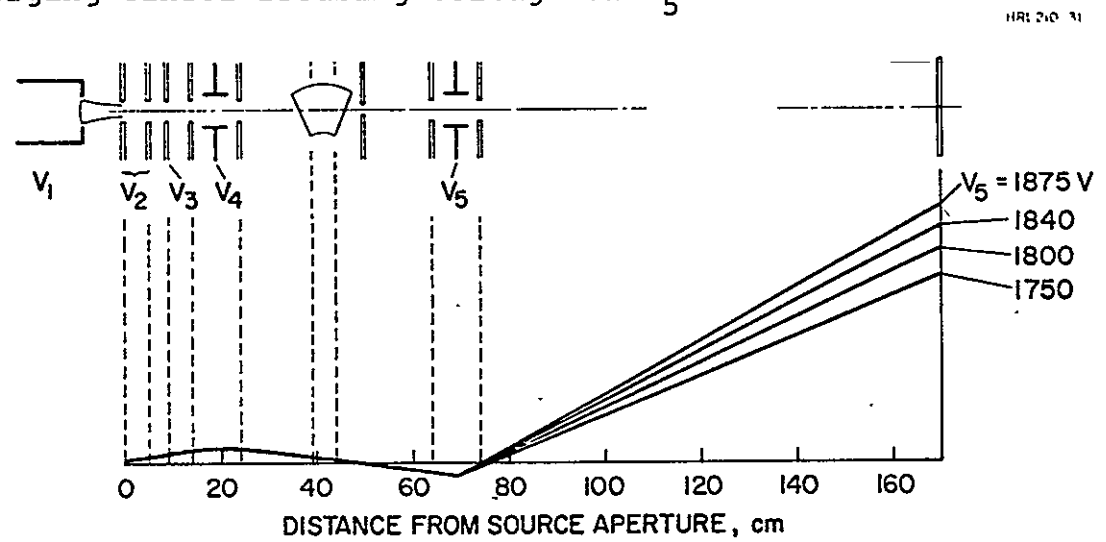

Fig. IV-37.
Computer generated trajectories showing effect of changing the diverging einzel focusing voltage V_5 for constant extraction voltage of 3500 V and beam voltage of 200 V.. Focusing einzel voltage = 1210 V = constant.

edge trajectory when the first einzel lens focusing voltage V_4 is varied from 1190 to 1220 V with all other voltages held constant. When this lens is too weakly excited the rays enter the second einzel lens too close to the axis, resulting in a target beam diameter of only 7.4 cm for the V_4 = 1190 V case. We also see that the outer beam edge is almost striking the edge of the aperture, so that any further reduction of this lens strength would increase the interception on the aperture. As the lens strength is increased to V_4 = 1210 V, the beam diameter at the target is the required 10 cm. Further increase in lens strength above this optimum value produces a larger target diameter until interception again starts trimming the beam edge at the aperture.

The operation of the second einzel lens which forms the final image at the target is shown in Fig. IV-37 as a function of lens strength for constant entrance conditions.

The diverging rays entering this lens are overfocused to form a magnified image at the target. For the case shown in Fig. IV-37, the target diameter increases from a diameter of 7.6 cm at V_5 = 1750 V to 10 cm at V_5 = 1840 V.

4. Beam Energy

For all the cases considered above the total source extraction voltage ($V_1 + |V_2|$) was either 1750 or 3500 V. This results because better source ion optical characteristics are obtained if the source does not have to be designed to operate over a wide range of total extraction voltages. With the accel-decel arrangement the beam energy is numerically equal to the positive voltage V_1, applied to the source and the decel voltage is numerically equal to the voltage across the accelerator plates ($V_1 + |V_2|$). The decel voltage prevents any secondary electrons created past the accelerator from bombarding the source. Figure IV-38 shows the focusing

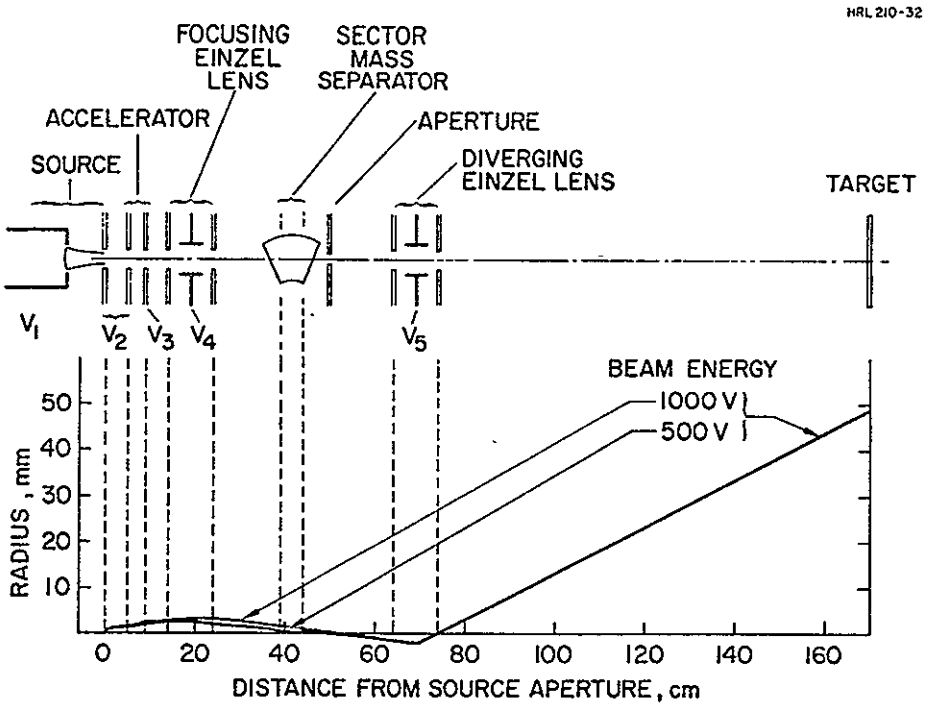

Fig. IV-38.
Computer generated trajectories for constant extraction voltage of 1750 V with target energies of 1000 and 500 V.

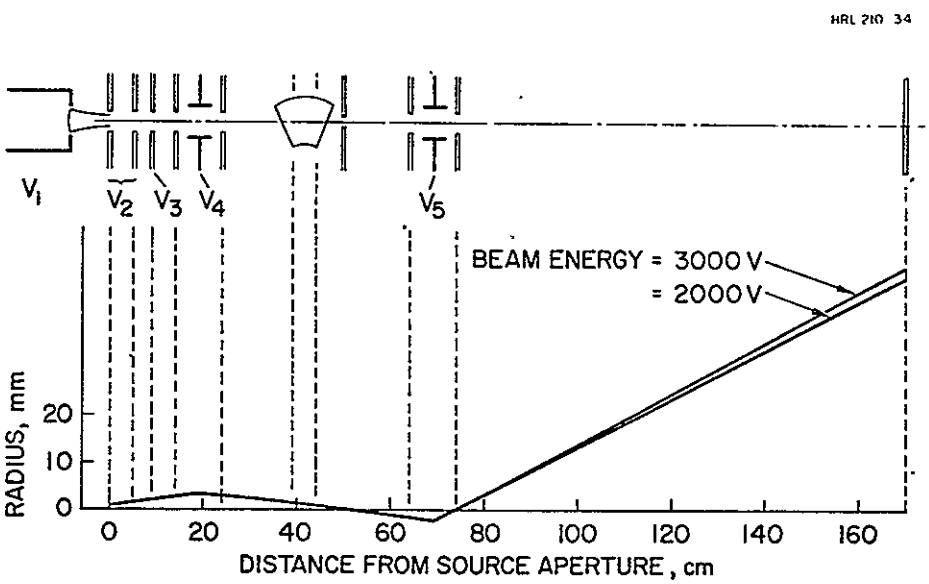

Fig. IV-39.
Computer generated trajectories for constant extraction voltage of 3500 V with target energies of 1000 and 500 V.

voltages required and the computer generated trajectories for beam energies of 500 and 1000 V for a source extraction voltage of 1750 V. Similarly, beam energies of 2000 V and 3000 V with a source extraction voltage of 3500 V are shown in Fig. IV-39. For all these cases the nominal beam diameter is 10 cm, as required.

5. Beam Intensity

a. Uniformity

The uniformity of the beam at the target is determined by the current density profile at the source, the aberrations in the ion extraction system and each of the elements of the ion optical system, and the accuracy of the alignment of the various elements. Thus it is virtually impossible to treat this parameter purely analytically. If an actual system were to be built from the design discussed here, the performance of the actual components (source, extractor, lenses, separator, etc.) at each interface must be measured experimentally and minor adjustments made to compensate for the aberration as required.

This can be accomplished only if good design practices have been followed. These have already been discussed in the sections dealing with the individual components:

1. source — low energy spread, radial uniformity of plasma density
2. ion extraction system — design for laminar ion flow with the correct divergence angle
3. einzel lens — design so that beam is much smaller than lens aperture and passes accurately along lens axis

4. Mass separator

a. magnetic sector – choose shape of magnet gap and entrance and exit conditions to reduce astigmatism, keep beam small through separator so all ions see similar conditions.

b. ExB – choose entrance and exit conditions and ratio of E/B to reduce first order aberrations.

Figure IV-40 shows that under the assumption of zero lens aberrations and a source emittance diagram of the type calculated in Fig. IV-16, no nonuniformities arise in the beam intensity as it traverses the system.

b. Intensity Variation

The total system must be able to change the target current by three orders of magnitude. Because it is not possible to operate the rf source over such a wide dynamic range, it is necessary that the beam transport system provide approximately a factor of 100 intensity variation, which together with a variation of source current by a factor of $\sim$ 10 provides the total dynamic range required. The source current will be varied by changing the neutral H_2 flow and/or the rf excitation power. The variation provided by the beam transport system is accomplished by flooding an aperture and allowing only a small fraction of the current to pass through the aperture. This is illustrated in Fig. IV-41, where the effect of changing the first einzel focusing voltage is shown. This figure shows that the beam size at the aperture varies from a radius of less than 0.1 cm to greater than 1.1 cm at the first einzel focusing voltage is varied from 800 to 300 V. With this arrangement only the rays leaving the source very

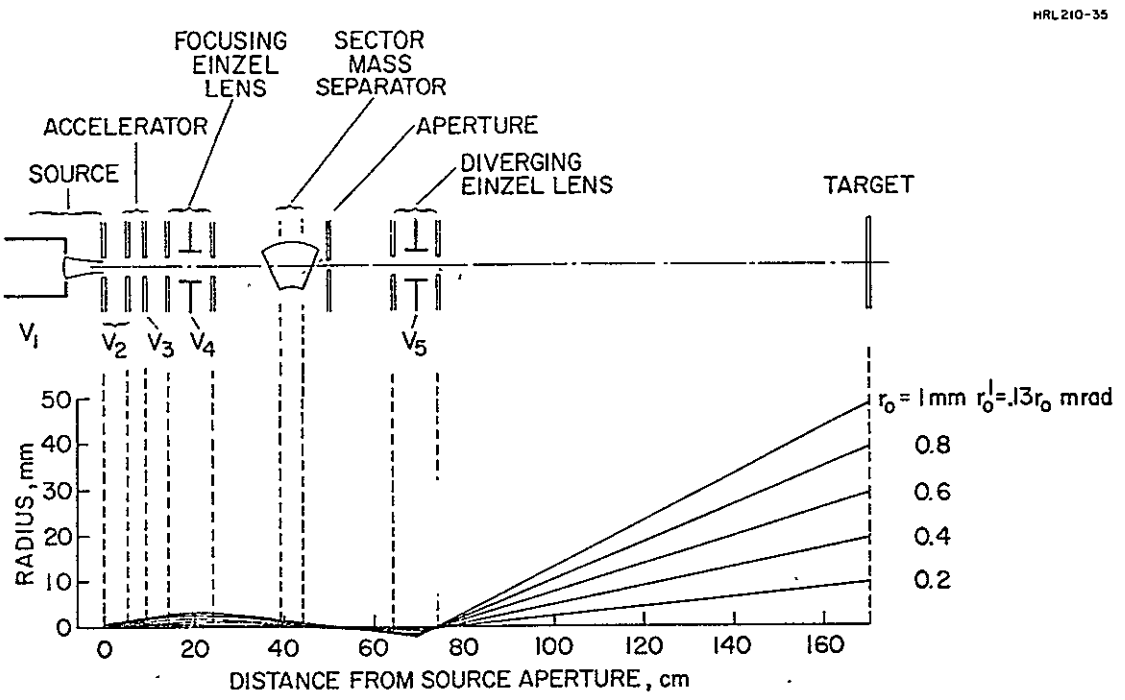

Fig. IV-40. Computer generated trajectories showing effect of initial height and slope for extraction voltage of 3500 V and beam voltage of 2000 V.

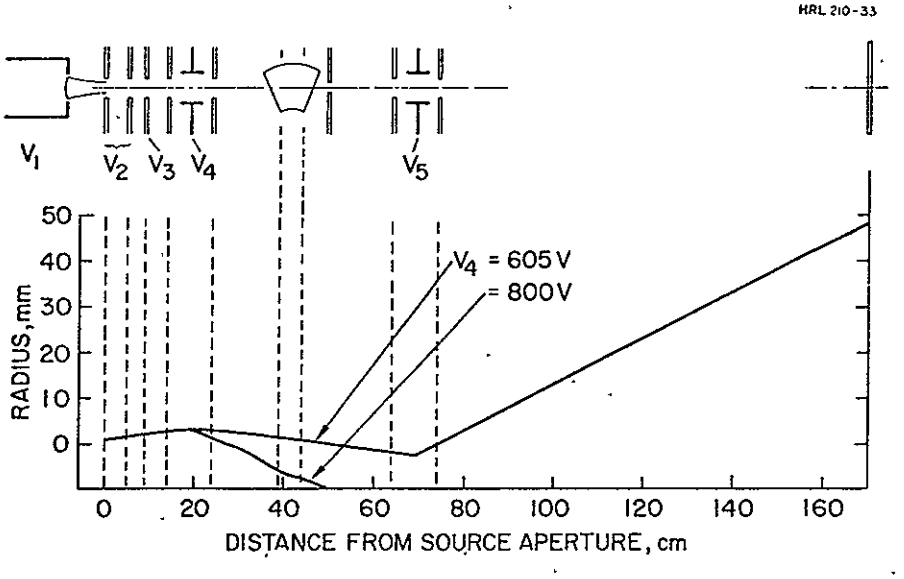

Fig. IV-41.
Computer generated trajectories showing how beam size at aperture varies with first Einzel focusing voltage for extraction voltage of 1750 V and beam voltage of 1000 V.

close to, and making very small angles with, the axis pass through the aperture, so that the resulting beam intensity at the target is reduced by a factor of approximately a 100 $((1/0.1)^2)$. This is about the maximum intensity ratio possible with this method because the image size at the target is limited by the maximum magnification (minimum focal length) of the lens.

6. Beam Rastering System

a. Advantages

The system illustrated in Fig. IV-35 is based on the requirement that the simulation requires a large dc proton beam which covers all of the target area uniformly. As discussed in Appendix A.
the simulation would not be impaired if the protons arrived at the target as a series of discrete pulses at rf frequencies. If it can be demonstrated experimentally that this is indeed true, a system employing a small diameter proton beam which is swept over the target surface in a pattern similar to the electron beam in a TV raster has many advantages. The system shown in Fig. IV-35 is easily converted to this design by changing the operating voltage of diverging einzel lens No. 2 to focus the beam to a spot on the target and introducing two pairs of orthogonal electrostatic deflecting plates in place of optional collimating einzel lens No. 3.

The advantages of a rastered system are

1. By sweeping a small beam over the large target area, the beam nonuniformities are smeared out and the coverage may be made as uniform as desired, even if some lens aberrations exist.

2. By programming the rate at which the beam is swept, the dose rate to each individual sample may be controlled (as a function of exposure time if desired).
3. The dose rate may be attenuated over several orders of magnitude while the source operates at the single fixed point where it performs best. This is achieved by deflecting the small beam off the target area entirely for some fraction of each raster period. This not only extends the operating range of the system, but simplifies the design of the ion source and its control system.
4. The accuracy of the dose measurement is improved by this technique because the total proton beam (which may be measured accurately) is projected onto each area of the target for a time which also can be measured accurately. The result is a far more accurate measure of dose than sampling a small fraction of the beam and relying on a prior measurement of beam homogeneity. It is also much easier to design a dynamic control system for this system than for one that samples a fraction ($\sim$ 1%) of the beam current (i.e., $\sim 10^{-11}$ A).

b. Design of the Deflection System

The design of an electrostatic deflection system is relatively straightforward. For the present design the distance ℓ from the downstream deflection system to the target is fixed at approximately 80 cm. With this distance fixed the two parameters which determine the deflection sensitivity are the deflection length b and the plate separation a (see Fig. IV-42). Qualitatively a small plate separation increases deflection sensitivity but increases deflection aberrations

produced by fringing fields, while a large length decreases deflection defocusing effects but increases deflection length and plate capacitance and hence deflection power. The relation between the deflection angle and normalized deflection voltage V_D/V_o, where V_D is the deflection voltage and V_o is the beam voltage, is given by Spangenberg (Ref. IV-40),

$$\tan \theta = \frac{y_s}{\ell} \frac{bV_d}{2aV_o} \qquad \text{(IV-19)}$$

where, with reference to Fig. IV-42

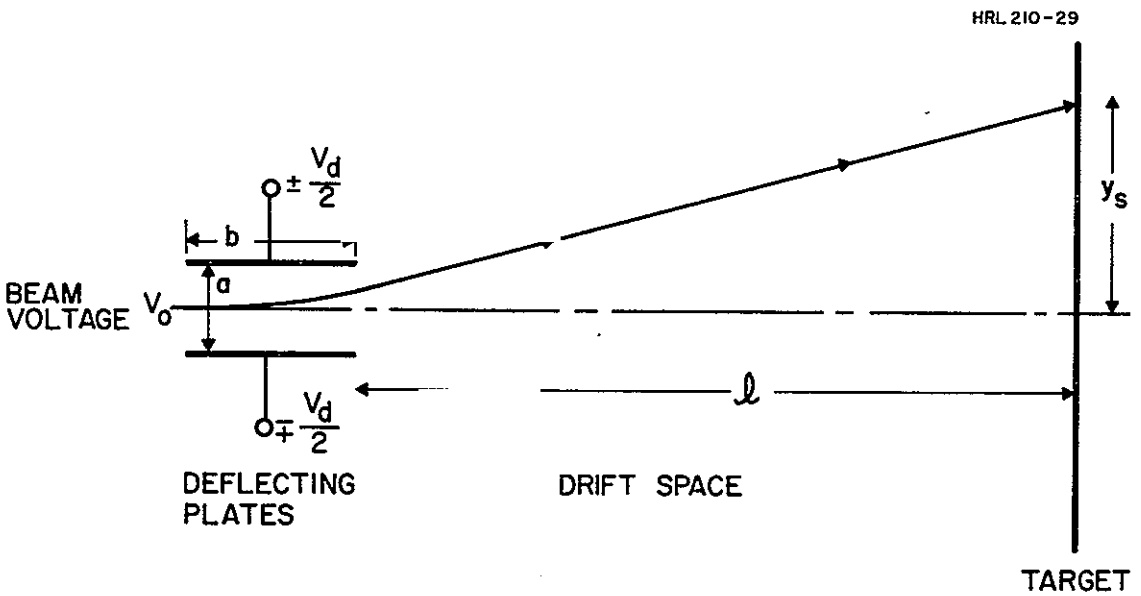

Fig. IV-42. Schematic of E x B separator.

For the present system we will choose a deflection sensitivity such that the maximum peak-to-peak deflection voltage is 300 V (which is 10% of the maximum beam voltage of 3000 V). Therefore, since $\tan \theta = 5/80 = 0.0625$, the plate length for a plate spacing of 2 cm is given by using (IV-19)

$$b = \frac{2 \tan \theta}{(V_D/V_o)} a \qquad \text{(IV-20)}$$

$$b = 2 \left(\frac{0.0625}{0.05}\right) 2 = 5 \text{ cm} \qquad \text{(IV-21)}$$

e. Estimation of Maximum Sweep Frequency

The maximum sweep frequency may be estimated as follows. The transit time τ, which is the time a proton spends in the deflection system, is related to the deflection plate length b and proton velocity v by

$$\tau = \frac{b}{v} \qquad \text{(IV-22)}$$

For protons the velocity is

$$v = \sqrt{\frac{2eV_o}{m}} = 1.38 \times 10^6 \sqrt{V_o} \text{ cm/sec.} \qquad \text{(IV-23)}$$

Now let the period associated with the sweep frequency f_s be t_s where

$$\frac{1}{f_s} ; \qquad \text{(IV-24)}$$

then it is apparent that $\tau << t_s$ for satisfactory operation. If this relation is not satisfied, the deflection voltage V_d will change significantly while the proton passes between the deflection plates and the system will not function properly. While it is true that sophisticated deflection systems have been developed for high speed oscilloscopes which permit $\tau = t_s$, a practical limit to be used in the following calculations is $t_s = 10\ \tau$. Thus with the above criteria the maximum sweep frequency is related to the transit time as

$$f_s \leq \frac{1}{10\ \tau} ,$$

which can be written using (IV-22) and (IV-23) as

$$f_s \leq \frac{1.38 \times 10^5 \sqrt{V_o}}{b}$$

This equation shows that because we cannot change the fixed beam voltage, the only adjustable parameter is the deflection length, which was chosen previously to be 5 cm by deflection sensitivity considerations. For example, if we decreased the deflection sensitivity from $V_D/V_o = 0.10$ to 0.20 the length could be halved, raising f_s by a factor of two but at the expense of increased deflection defocusing effects. For a beam voltage of 1000 V, using $b = 5$ cm the maximum sweep frequency is $f_s \leq 8.8 \times 10^5 \text{ sec}^{-1} \sim 1$ MHz. The target is two-dimensional, however. Thus, if the beam is 0.5 cm in diameter it must traverse a 10 cm target 20 times to cover the whole area, and the real frequency at which any spot on the target will be irradiated is 0.05 f_s, or 50 kHz.

Generalizing the above for the dimensions used as the example, the frequency at which any point on the target is irradiated is

$$100 \left(\frac{V_o}{1000} \right)^{1/2} d_b \qquad \text{(IV-25)}$$

where

$f_t \equiv$ frequency at which a point on target is irradiated, kilohertz

$V_o \equiv$ accelerating voltage, volts

$d_b \equiv$ beam at target, centimeters.

Other choices of dimensions will give a slightly different constant, but the functional form will remain the same as long as d_b is small relative to the target diameter. As the beam diameter approaches the target diameter, the deflecting voltage may be reduced so that in the limit a broad uniform beam with no deflection is required.

SECTION V

DESIGN ANALYSIS OF AN OPTIMIZED SOLAR WIND SIMULATOR SYSTEM

This analysis of the optimized solar wind simulator system is based on the preceding discussion of the solar wind characteristics, the simulator requirements, and the analysis of the proton beam formation apparatus. The outline drawing of the simulator system presented in Fig. V-1 shows the major components of the system. The first two are the ion source and the ion optics system, which includes the mass separator. Together these produce the proton beam. The neutralizer system is an important yet inconspicuous element of the simulator. The sample chamber is the largest component. Within it are the sample mounting plate, the detectors (ion, electron, photon) for monitoring and controlling the sources, and the sample transfer mechanism. The integrating sphere is attached to the sample chamber.

The design analysis is organized in terms of these components. The proton beam apparatus (i.e., the ion source, the ion optics, and the mass separator) is presented as a summary of the detailed analysis given in the previous sections of this report. The neutralizer is discussed in Section V-C. The discussion of the sample chamber is organized into two elements. The first is concerned with the details of the sample mounting and transfer mechanisms. The second involves the ion and electron measurement instrumentation. Vacuum pumps are used in several of the components of the system. As a result, the vacuum design is analyzed in a separate section of this final report.

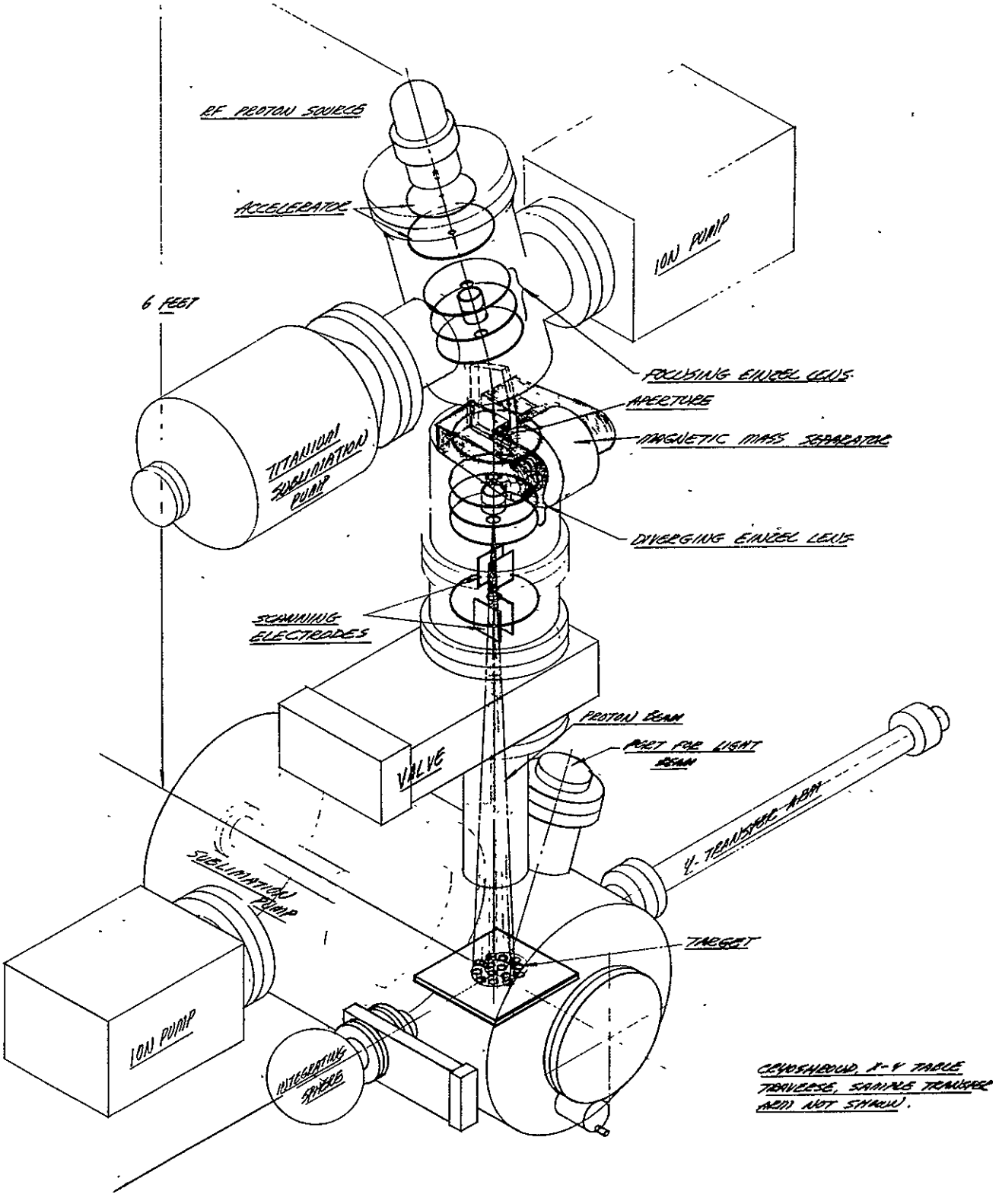

Fig. V-1. Solar wind simulator.

An important aspect of this analysis was the consideration of how the individual components would interact with each other and result in the selection and design of components providing a good compromise of the various features. An example of this is the case of the ion source exit aperture. It must be designed to provide the necessary ion beam trajectories in order to match the requirements of the ion optics and mass separation system. At the same time, however, the ion source aperture geometry should be designed to limit the amount of gas that enters the rest of the system. This requirement thus provides a restraint on design of the exit aperture which is an important point because a system such as this can be designed in a number of ways that use different components or modifications of the same components. With careful design and fabrication all will perform satisfactorily. Thus the design presented in this section is one of these configurations.

ION SOURCE

The rf ion source was selected because when operating at the desired maximum ion beam current, it places the smallest hydrogen gas load on the system's vacuum pumps. Construction of this type of source is relatively simple and inexpensive. Also several corporations manufacture the rf source which, with modifications to the ion extraction system, could be used to obtain the ion trajectories that were calculated to provide the necessary emittance (see Fig. IV-14). It is important to add a servo control system to control the hydrogen input flowrate so that the ion source has a stable operation.

In the event that it is unnecessary or impossible (due to reciprocity failure) to operate at levels of about 100 times the solar wind, the use of the electron bombardment

source may be advantageous. It is easier to vary the beam intensity with this source than with the rf source. The major problems are that the electron bombardment source is much less efficient with respect to the hydrogen gas usage and it requires a thermionic emitter which could be contaminated by the outgassing of the samples and the integrating sphere coating.

B. MASS SEPARATOR AND ION OPTICS SYSTEM

A sector type magnet was chosen to separate the protons from the rest of the beam. It fulfills the two basic requirments — separation of the proton beam from both the charged and uncharged (i.e., photons, charge exchange neutrals) contaminants from the source without seriously defocusing the beam. Section IV-B discusses the tradeoff between adequate separation of charged species and beam defocusing due to energy dispersion which must be made in choosing the separator angle. As shown in Fig. V-2 a 20° sector separates the protons from the H_2^+ beam by 0.6 cm at the aperture stop located 4 cm downstream of the exit plane of the separator. The increase in diameter of the 1 mm diameter, 1000 V beam due to a 50 eV energy spread when passing through this 20° separator is less than 0.5 mm. Thus, a 2 mm aperture will pass all of the proton beam and block other charged species. This separator will nominally operate at a magnetic field of 300 gauss and consume less than 200 W. It should not require water cooling. The final design of a separator such as this which is to be actually constructed should involve careful consideration of the shape of the magnet pole entrance and exit surfaces and of the magnetic gap itself to minimize aberrations. It is not possible to treat such factors in a parametric way so that they would be meaningful here.

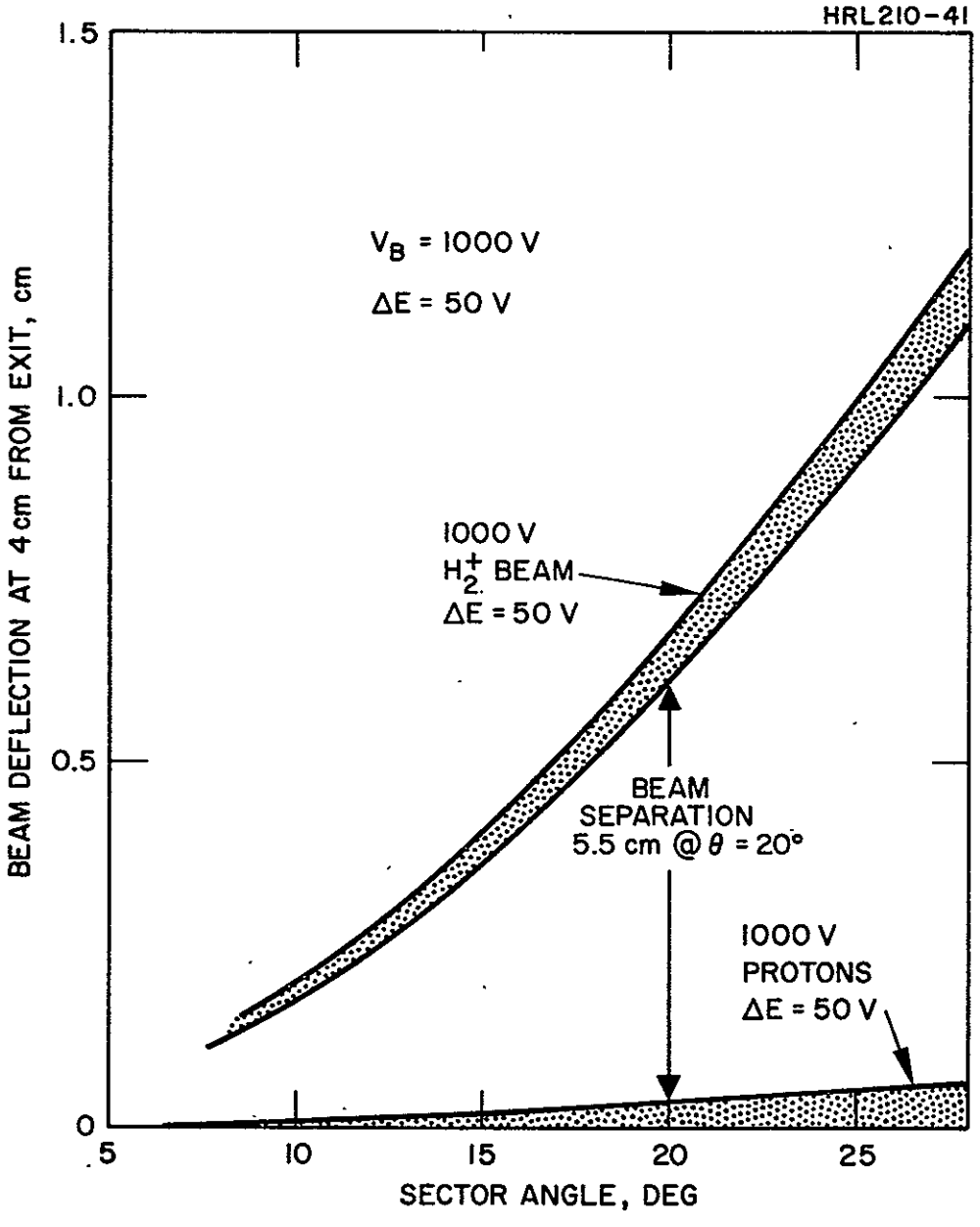

Fig. V-2. Separation of proton and H_2^+ beams at apertures 4 cm from exit of separator.

An possible alternative choice of separator is the crossed electric and magnetic field or E x B separator operated to deflect the proton beam through an angle of 5° or more. The principal drawback to this device appears to be the difficulty of designing the electric field pole pieces to achieve the desired uniform electric fields without a number of trimming electrodes. It appears that current studies in this area will soon eliminate the problem, making this a very attractive device. The advantages of an E x B separator is that first order aberrations may be reduced by a proper selection of the ratio E/B.

The beam extraction system is designed so that the only source is at high voltage, and all pumps, lenses and, of course, the samples are at ground potential. The beam is kept small until it reaches the last lens, to reduce aberrations in the lenses and separator and to reduce the size of components. The small beam can be scanned over the sample thus giving advantages such as uniformity, intensity control, and sample size. The small size of the beam also means that it is possible to isolate the source chamber from the main chamber with a small orifice without affecting the beam. Thus, the two chambers may be pumped separately and the large gas load from the source removed without interacting with the target. In addition, the orifice is used to adjust the ion beam intensity. The use of such an orifice places a major constraint on the design of the vacuum system because the system should be free of gases which can be decomposed to form a dielectric film over the surface of the orifice. If such a film forms, it can develop a surface charge which causes the orifice to act as an electrostatic lens that will perturb the ion beam. As a result, the vacuum system is limited to the use of sputter ion and titanium sublimation pumps.

It is of interest to briefly consider the function of each element of the ion optical system in turn.

1. The ion extraction system focuses the ions from the source into a beam with a divergence angle compatible with the rest of the ion optical system. It is operated in the accel/decel mode (see Section IV-A) to prevent electron backstreaming and to permit adjustment of the beam voltage without affecting the field gradient at the surface of the plasma in the source from which the ions are extracted. The single small aperture provides adequate current while still acting as an effective flow impedance to reduce neutral hydrogen efflux from the discharge chamber.

2. The first einzel lens focuses the ion beam through the separator onto the aperture 4 cm from the exit plane of the magnetic sector. By adjusting the beam size at this aperture the intensity of the beam which arrives at the target may be adjusted by a factor of 100.

3. The magnetic mass separator and the orifice separate the proton beam from the other ions, the hydrogen gas, the Lyman alpha photons, and the fast neutrals due to charge exchange.

4. The second einzel lens controls the size of the beam at the target. It is capable of expanding the beam that passes through the aperture to 10 cm diameter at the target plane or maintaining the beam size at 0.1 cm so that it may be scanned over the target.

5. The above four elements will provide a 10 cm diameter beam at the target in which no proton trajectory has an angle of more than 3° with respect to the normal from the target plane. If a more parallel beam is desired, an additional einzel lens (not shown in Fig. V-3) may be inserted to collimate the beam. Because this lens must accommodate a 10 cm diameter beam, the aberrations will be appreciable and it is not recommended that it be used in this system.

6. As shown in the insert in Fig. V-3), a set of deflection plates may be inserted between the second lens and the target to raster the beam.

C. NEUTRALIZER

The importance of neutralizing the positive charge of the proton beam when it is irradiating dielectric samples was discussed in Section III-B-1. The neutralizer consists of an electron source that produces a maximum of 3×10^{-6} A of 20 to 40 eV electrons. This can be accomplished using a directly heated filament source or an indirectly heated cathode in an accel-decel configuration. As the neutralizer is mounted inside the sample chamber, the neutralizer-to-target distance will be less than 20 cm. The space charge limited flow of current to the target for a 20 V potential and a 20 cm distance is

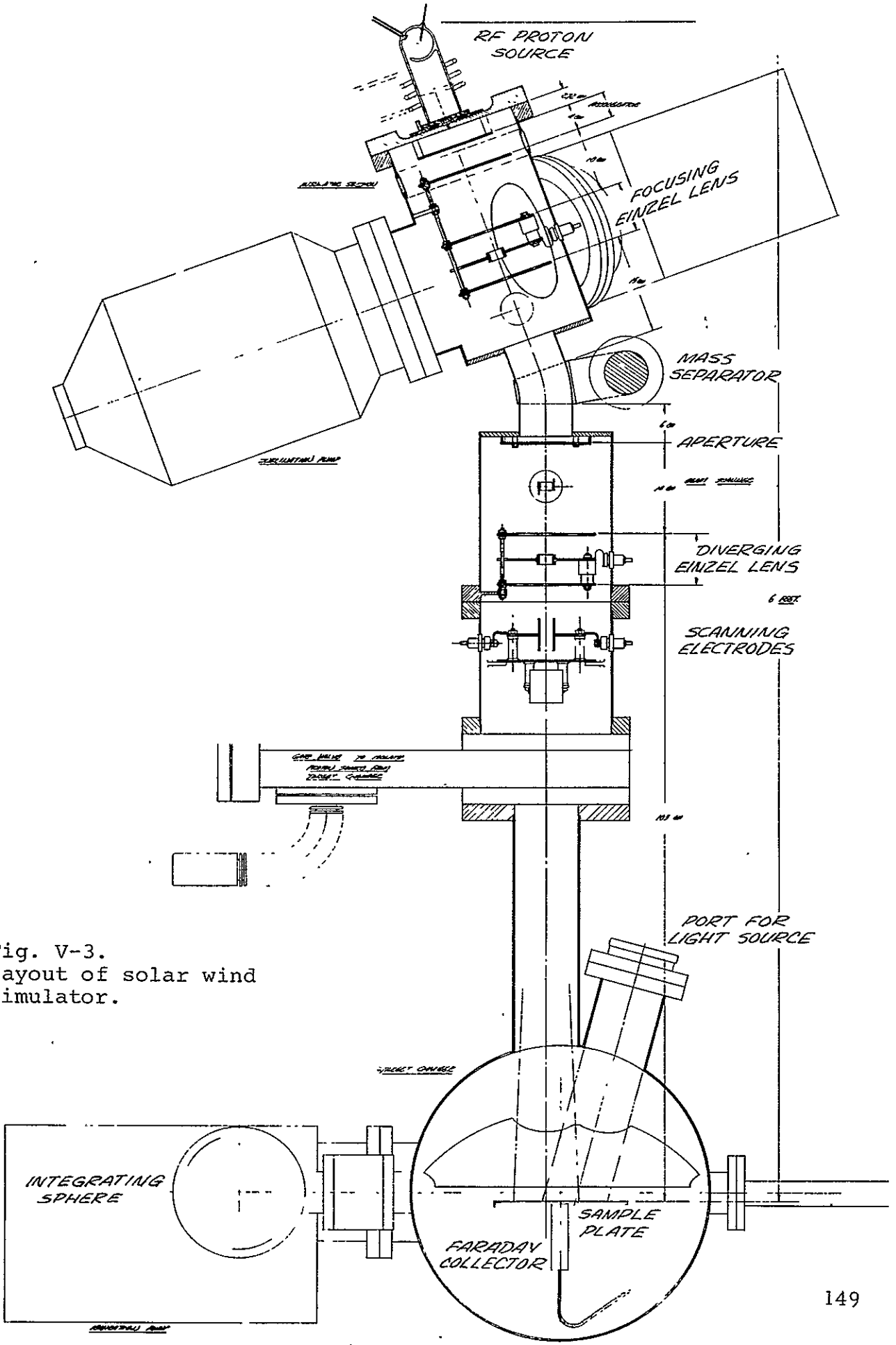

Fig. V-3.
Layout of solar wind simulator.

$$J_e = \frac{2.33 \times 10^{-6} \ (20)^{3/2}}{(20)^2}$$

$$= 5.2 \times 10^{-7} \ A\text{-}cm^{-2} \ .$$

This value is larger than the 3×10^{-8} $A\text{-}cm^{-2}$ value required to neutralize the maximum 1000 equivalent sun dose rate.

D. SAMPLE CHAMBER

The sample chamber contains the cryogenic shroud, the transfer arms, and the sample mounting plate, which in addition to supporting the samples also supports the proton, electron, and photon detection and measurement apparatus. The discussion of the sample chamber components is sufficiently detailed to explain the manner in which they operate. However, because the major emphasis of the program was to develop the solar wind simulator, these components were not analyzed to the same extent as were the ion source and the ion optics. The discussion is divided into an analysis of the sample holder and the cryo shroud, and of the measurement equipment.

1. Sample Mounting Plate

The sample mounting plate is a constant temperature plate to which the samples are mechanically attached. It is held at a constant temperature by the circulation of a fluid from an exterior constant temperature reservoir. The unit is designed to be in a horizontal position so as to be able to accept powder samples. The axis of the proton beam is normal to the sample surface while the light beam is at a 15° angle.

The mounting plate is supported on ground rods with ball bearing bushings used to allow easy travel along the rods. Bellows sealed rotary motion devices are used to move the plate in the x-y plane. The travel makes possible the sample transfer and the probing of the proton and photon beams. The sample transfer operates in the following manner. The plate is positioned above the z-axis transfer arm (see Fig. V-4). The arm is extended to engage the sample holder, and the rotary motion then is used to unlock the sample. The sample is carried upward by moving the z-axis transfer arm and the sample is transferred to the y-axis sample transport arm. The y-axis transfer arm moves the sample into the integrating sphere.

Good thermal contact between the sample and the sample mounting plate is essential to prevent annealing of the damage sites. This requires locking the sample holders to the sample mounting plate by a screw thread or a bayonet mount. The sample holder is a copper slug which is coated with the sample of thermal control coating. The sample (as it sits on the sample holder) is positioned about 0.2 cm above the surface of the mounting plate. This is to prevent any material sputtered from the plate from striking the sample surface.

Two types of sample configurations are considered. In one case, all of the irradiated samples are mounted in a 10 cm diameter circle. These samples are simultaneously proton and photon irradiated. Several control samples are placed outside the edge of the beam. In the second configuration three samples are exposed to protons only, three receive protons and photons, three receive only photons, and the remaining are controls.

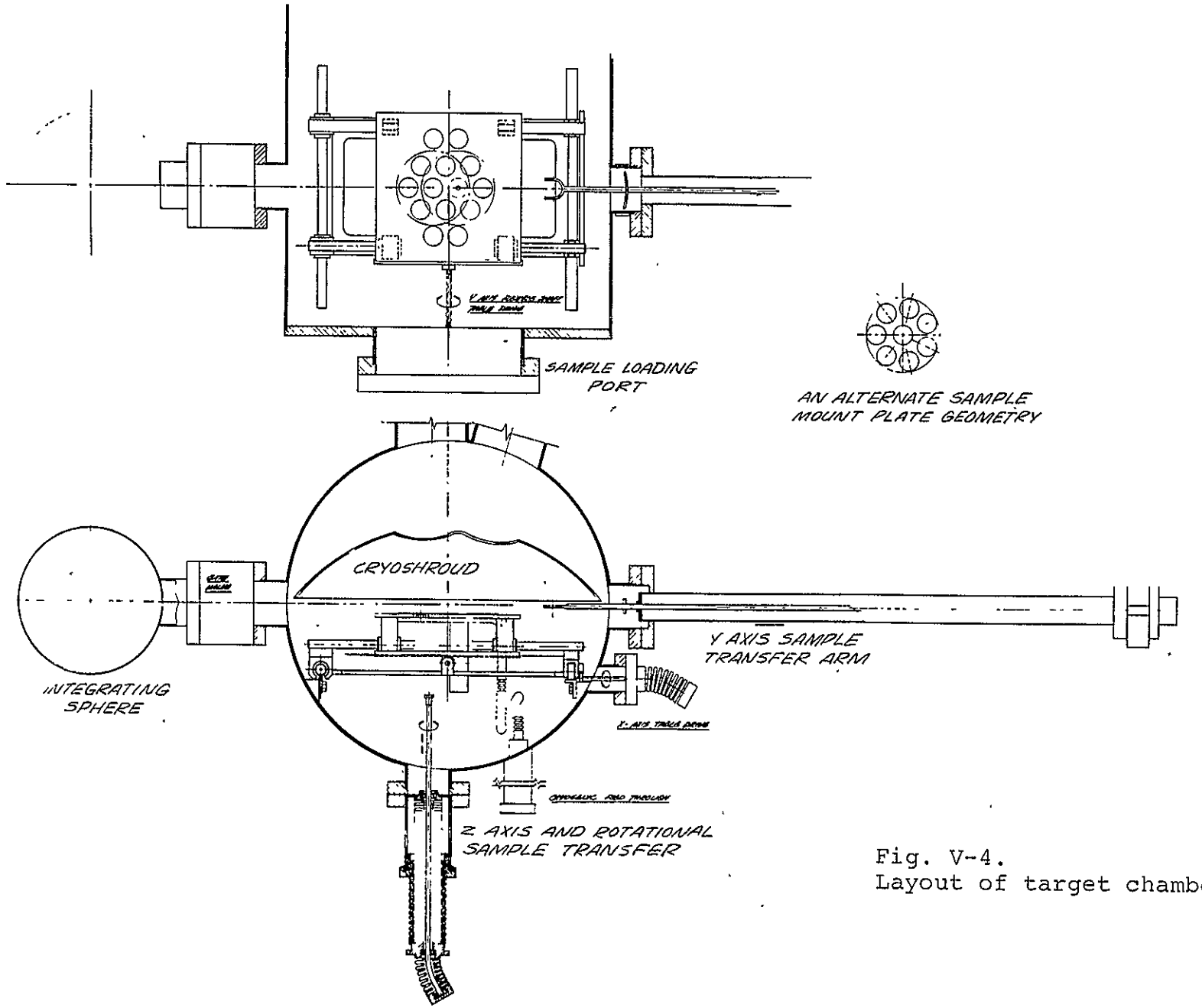

Fig. V-4.
Layout of target chamber.

The temperature control of the mounting plate is accomplished by circulating fluid through flexible lines in the vacuum system to the sample plate. Thus, the plate can operate down to about 100°K (the boiling point of nitrogen). Operating temperatures of about 330°K can be obtained by using either a higher boiling fluid or electric resistance heaters. Thermocouples can be used to determine the mounting plate temperature and thus the sample temperature.

A liquid nitrogen cooled shroud is located over the sample stage. This shroud, which is shown in Fig. V-4, serves several functions. It acts as a collimator for the incident photon and proton beams. The inner surface is coated to have absorptivity of about 0.95 so that the shroud will trap nearly all of the reflected photon radiation. This coating is formed by anodization or oxidation of the surface. The surface will condense the materials that are evaporated or sputtered from the sample and the sample stage. The shroud also serves to simulate the 4°K condition of space that surrounds a satellite. The radiation sink provided by the 100°K shroud is essentially equal to the 4°K condition of space which surrounds the ∿300°K satellite.

2. Beam Measurement Equipment

The sample mounting plate also supports the apparatus for determining the flux, energy, and profile of the proton and electron beams and the flux and profile of the photon beam. The determination of the ion beam purity requires a mass spectrometer which could be located below the sample plate. These detectors, as well as some pressure sensors, are part of the control loop which regulates the operation of the ion source and the neutralizer.

The determination of the flux, energy, and profile of the proton beam is best accomplished by means of a Faraday collector. This is a deep collector cup with a length of about four times the diameter of the cup. It is shown in Fig. V-5. The narrow deep geometry of the cup is necessary to reduce the electric field at the bottom of the cup. The field is due to the potential difference between the cup and the surroundings. As a rough rule of thumb, the field in a tube falls off about e fold for each length down the tube equal to a diameter length. Thus, for a 4 to 1 ratio, the potential at the base of the collector is of the order of a few percent of the magnitude of the potential difference between the collector and the shield at its entrance. The low potential is essential to trap all secondary electrons and ions that are formed by the collection of energetic particles at the bottom of the Faraday collector. A short collector can be used if grids are used to suppress the secondary electron currents. Systems which use a short open collector or a collector in which the walls and base of the collector are separated are subject to errors due to the losses of the secondary currents.

The most accurate determination of the proton beam flux, energy, and profile is obtained when the neutralizer and the photon source are turned off. This can be done (prior to the introduction of dielectric samples into the system) by using metal blanks in place of the samples. The reason for this is to avoid the problems associated with measuring small currents of positive ions in the presence of neutralizer electron and photoelectron currents of equal or larger magnitude.

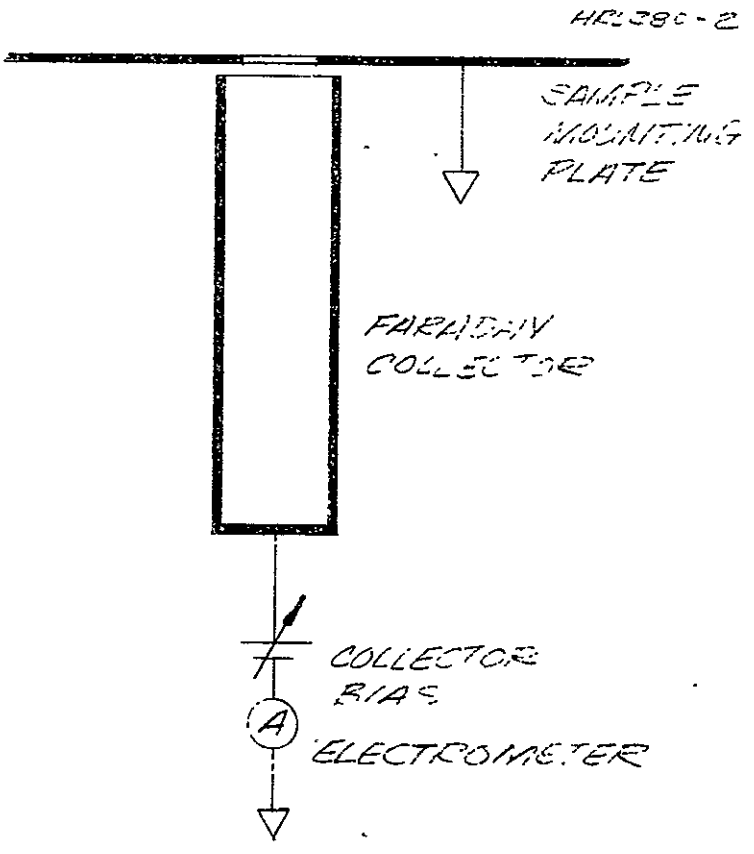

Fig. V-5. Faraday collector.

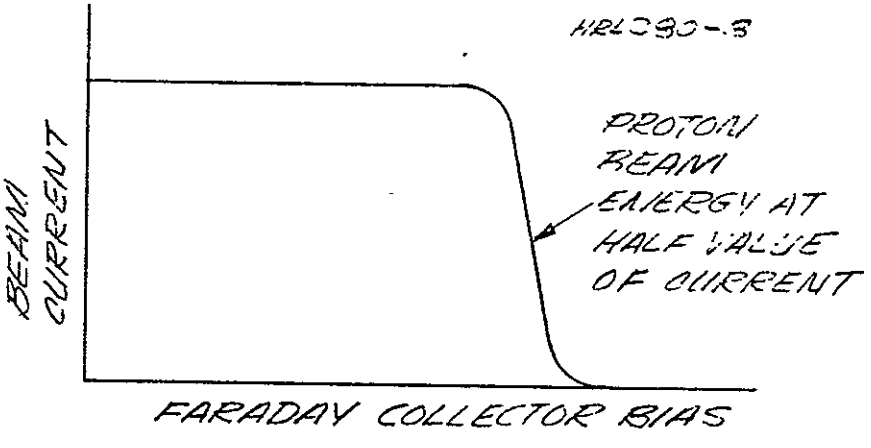

Fig. V-6. Beam energy.

The flux is measured by allowing the beam to pass through an aperture of known area into the Faraday collector. The flux is the beam current per unit area. There are two aspects of the proton beam energy that must be measured: the proton energy and the energy spread. The proton energy is determined by measuring the beam current as a function of the bias potential placed on the Faraday collector which is shown in Fig. V-5. A representative curve is shown in Fig. V-6. The energy spread of the proton beam is given by first derivative of the current. This is shown in graphical form in Fig. V-7.

The profile is determined by measuring the beam flux (at any fixed set of operating conditions) at a number of points by moving the sample plate in the x-y plane. The cross sectional area of the Faraday collector is established as a compromise between signal strength and resolution. The collector shown in Fig. V-5 has a 1 cm diameter aperture which is 10% of the beam diameter and 1% of the beam area. The sample size is estimated to be 2.5 cm diameter. Thus the detector is about 1/6 the sample area. If desired, the flux, energy, and profile of the electron beam can be measured in a similar manner with the proton and photon beams off.

Simultaneous measurement of the proton and electron beams are needed to regulate the operation of both sources, to provide the data about the proton dose rate, and to verify the degree of beam charge neutralization. To do this, it is necessary to separate the positively charged ion component from the negatively charged electrons. This can be accomplished by passing the ion and electron beam through a combined electric and magnetic field. This is shown in Fig. V-8. An alternative method of measuring the two components is to use a modulating grid collector. This is shown in Fig. V-9.

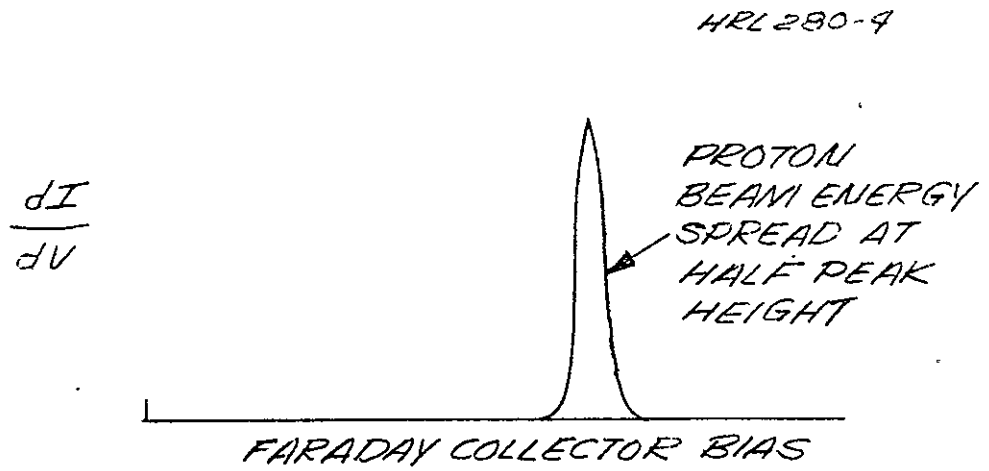

Fig. V-7. Beam energy spread.

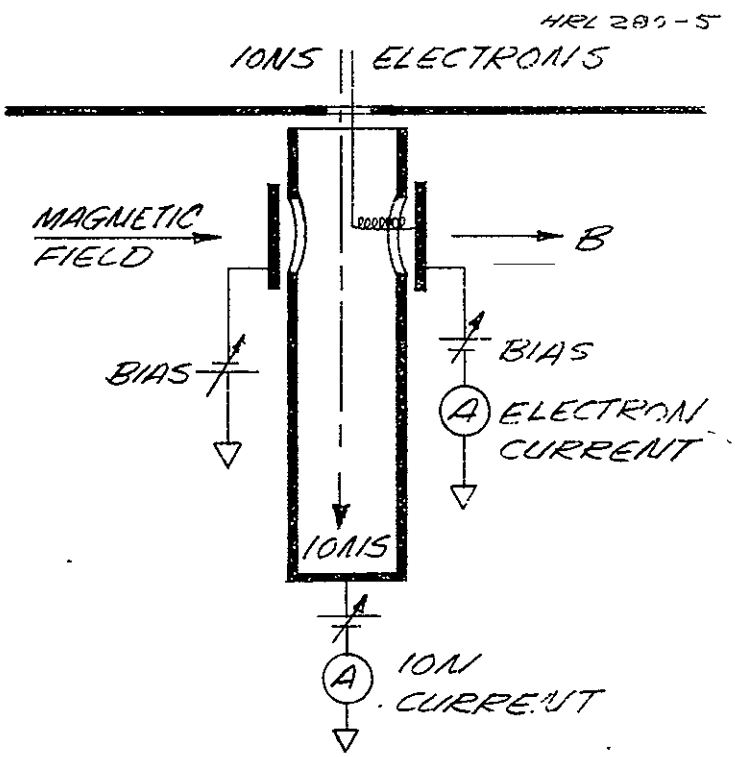

Fig. V-8.
Ion-electron separator.

Grids 1 and 3, the collector shield, and the aperture plate are at ground potential. Grid 2 has a modulated square wave potential applied to it. This grid modulates the electron component, leaving the ion component to reach the collector. Grid 3 serves to reduce the capacitive coupling of the modulated grid and the collector. Grid 4 is used to suppress secondary electrons. This type of collector was developed for use on the Explorer 10 by the M.I.T. group (Ref. V-1).

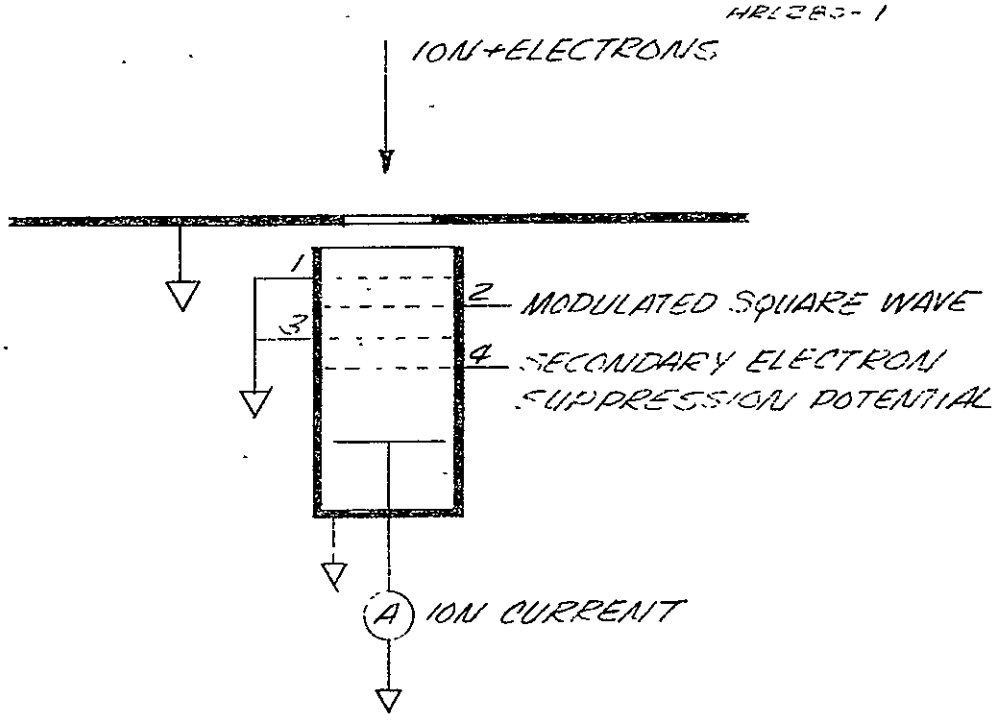

Fig. V-9. Ion-electron separator.

Some of the experimental problems that should be anticipated in the design of the measurement apparatus include both extremely low signal levels and the high noise levels that can result from the rf generator used in the ion source, the plasma in the ion source, stray electron currents in the chamber, and photoelectrons. While there is little that can

be done about the low signal levels (e.g., signal of the order of 10^{-13} A), there are a number of remedies for the high noise level. The rf and plasma noise can be reduced by the use of π or T section filters or by the use of ferrite beads. The design of the filters can be obtained from any standard text. Carefully designed shields are the most effective way of preventing the stray electron currents from measurement as part of the signal. Photoelectric currents can be suppressed by operating the collector at a slightly positive bias with respect to the surroundings.

Mass spectrometric analysis of the proton beam to determine the beam purity is essential in solar wind simulator systems that use the Bennett type rf mass separators to purify the proton beam. This is because of the variable filtering of this device (see Section IV-B). A mass analysis of the proton beam formed in the proposed optimized system is unnecessary because the design of the magnetic field mass separator beam purifier will produce an essentially pure proton beam. Nevertheless, a discussion of the design requirements for a mass spectrometer analyzer is included in this section to make this report a complete survey of the elements of a solar wind simulator.

The design requirements for the mass analyzer, which could be used to determine the beam purity, involve some unique features because of limitations imposed by the operating conditions of the solar wind simulator. The two most important problems are the very low signal strength and the high ion energy. A conventional mass spectrometer operates with ion currents that are significantly larger than that of the solar wind, and with ion energies that are much lower than the 0.5 to 3 keV energy range of the solar wind.

The magnitude of the signal (assuming a beam current density of 3×10^{-11} A-cm^{-2}) is limited by the geometry of the entrance aperture of the analyzer, the transmission through the analyzer, and the requirement for detecting impurities to a specific precision. If we assume an entrance area of 0.1 cm^2 and 100% transmission through the analyzer, the maximum proton signal at the detector would be 3×10^{-12} A. If a precision of ±0.5%, is desired (i.e., measurement of the proton content to 99 ± 0.5% and of the total impurity level to 1 ± 0.5%), the detector must be able to measure signals to below 1.5×10^{-14} A. The minimum signal level will be even smaller because resolution of the impurities is necessary to the determination of the total impurities.

The measurement of dc signals of this magnitude is difficult and requires the use of a 10 or 14 stage electron multiplier to amplify the signals by a factor of about 10^6. Even so, the measurement of the output signal (of the order of 10^{-9} A) is difficult due to the presence of rf noise (produced by the ion source).

The type of impurity will be dependent on the purity of the gas, the type of ion source and mass separator used, and the composition of the residual gas in the system. In general, we expect the two most prominent impurities to be H_2^+ and H_3^+. Residual gas and impurities in the H_2 gas supply will result in the production of ions such as CH_4^+, OH^+, H_2O^+, N_2^+, O_2^+, CO^+, and CO_2^+. Detection and measurement of H_2^+ and H_3^+ in the H^+ beam is much easier than the detection of the higher mass ions. This is particularly difficult because of the kilovolt energies associated with the solar wind particles. For example, a 5 cm radius of curvature magnetic deflection mass spectrometer analyzing an H^+, H_2^+, H_2O^+, and CO_2^+ mixture of ions (all having energies of 1 keV) would require magnetic fields of 910, 1290, 3860, and 6050 gauss. The last two would require a complex electromagnet.

A proposed beam purity analyzer would have the following characteristics. It would consist of a 60° sector magnetic mass separator mounted on a vacuum flange below the sample plate. The entrance aperture would view the proton beam through one of the holes in which the samples are usually mounted. The presence of the large electromagnet makes it necessary to put it outside the chamber. The detector would consist of a 14 stage electron multiplier.

The presence of fast neutrals at the target is anticipated only in systems using the rf type mass separator to purify the ion beam. The detection of these fast particles requires a mass analyzer (similar to that just discussed) that has a special ionizer section. This is because the neutrals have velocities associated with energies of 1000 eV. This means the neutral transit time through the electron beam in the ionizer is a few percent of the transit time of a room temperature gas.

The ion-electron converter (Refs. V-2, V-3) can be used for visual check of the beam shape and density variations. This consists of a fine metal mesh and an electron excited phosphor on a plate. The ions strike the mesh, generating secondary electrons which strike the phosphor that is held at a high positive potential this is shown in Fig. V-10. Use of an electroformed nickel mesh of 400 wires/cm gives resolution on the order of 25 to 50 μm.

E. THEORY AND DESIGN OF THE VACUUM SYSTEM

The goal in designing the vacuum system for the solar wind simulator is to provide an ultrahigh vacuum (UHV) environment for the experiments in the proton and photon irradiation of the thermal control coating materials, in order to simulate the conditions of interplanetary space. The

desired conditions are that all gases evolved from the surfaces are pumped to prevent their return to the surfaces, that the photon radiation (either reflected or emitted from the surface) is trapped to prevent its reflection onto other samples, and that the arrival of residual gas and radiation from the vacuum walls is negligible.

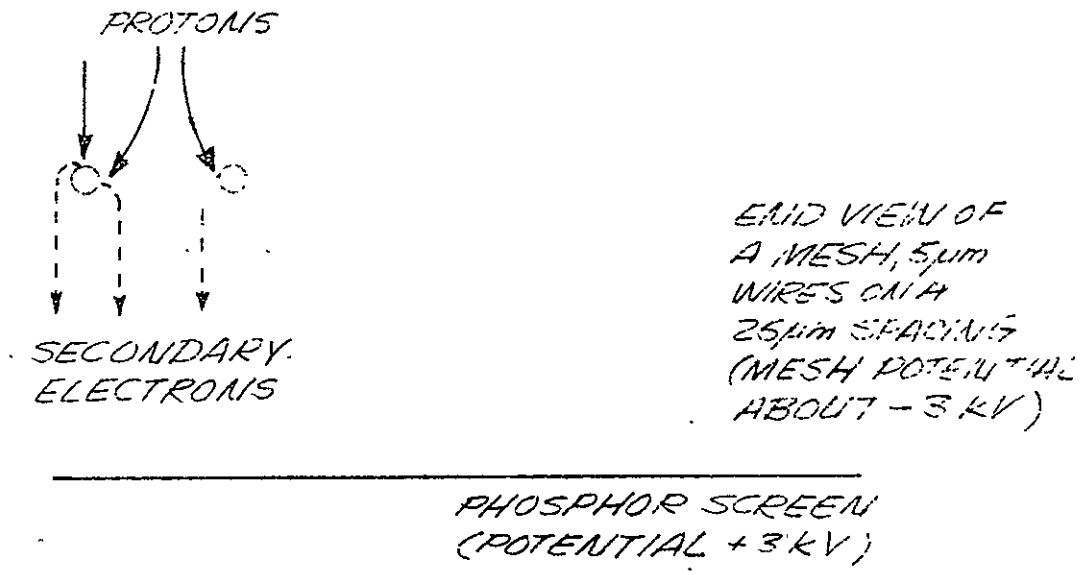

Fig. V-10. Ion-electron converter.

The proposed simulator consists of three subsystems which can be isolated from each other. These subsystems are the ion source, the integrating sphere, and the sample chamber. The bulk of the gas load will be pumped at the ion source. The ion source chamber can be isolated from the main chamber in order to permit either chamber to be let up to atmospheric pressure for loading or for repairs. The analysis of the components is presented in the following sections.

Estimates of the gas pressure in the interplanetary space are of the order of 10^{-13} Torr (Ref. V-4) for thermal energy particles and of the order of 10^{-11} Torr (Ref. V-4) for the directed stream of the solar wind from the sun. The achievement of these pressures in a laboratory vacuum system is possible but only at great expense, and is limited to systems where all the materials (including the samples) are selected on the basis of having low outgassing rates. In the case of the solar wind simulator the large gas load, which is made up of neutral hydrogen that comes from the ion source and of the variety of gases that result from the outgassing of the samples of thermal control coatings and of the internal coating of the integrating sphere, made it a practical impossibility to achieve a 10^{-13} Torr pressure.

The task of establishing an operating pressure for the optimized solar wind simulator concept is difficult because of the necessity of specifying (in addition to the maximum total operating pressure) the limit on the partial pressure of the residual gases that can be present in the vacuum station. Because of the limited amount of information it is not possible to establish a priori tolerance limits for the pressure of residual gases in the system. Instead, it is advisable to use a sensitive residual gas analyzer (RGA) to determine the partial pressures of the gases and to correlate this with the experimental observations.

1. Optimum Design Concept for the Solar Wind Simulator Vacuum System

A conceptual design for the vacuum system for the solar wind simulator is shown in Fig. V-1. The basic system has been divided into three component areas; the ion source and beam forming component, the main chamber which contains the samples, and the integrating sphere. This division is a

natural one that results from the differences in the gas loads and the vacuum problems associated with each of these components.

The ion source, which presents the major gas load to the total system, is differentially pumped to minimize the gas flow into the main chamber. This is accomplished by focusing the ion beam through a 0.2 cm diameter hole in the aperture plate that isolates the ion source and mass separator section from the rest of the system. This feature represents a major advantage of the system which expands a single small beam as opposed to a system which uses a broad beam. The ion source and the beam forming chamber are isolated from the main chamber by a high vacuum gate valve. This makes it possible to maintain the vacuum in one section, while the other section is open for modification of components or samples. This is especially important if it becomes necessary to repair or modify the ion source while the samples are kept in a UHV environment.

The internal reflective white coating of the integrating sphere has a very high surface to volume ratio; therefore, when it is exposed to air, it can adsorb a large amount of gas, which presents a large gas load to the system. The fragile nature of this coating makes it advisable to minimize the number of times the surface is subjected to the evacuation process. For these two reasons, the integrating sphere has a gate valve to isolate it from the main chamber.

The main vacuum chamber contains all the remaining equipment needed for the proton-photon irradiation of the thermal control coatings. This includes a temperature controlled stage on which the samples are mounted, the sample transfer mechanism, the probes to measure the ion, electron, and photon flux distribution at the target plane, equipment to analyze the beam purity and the vacuum condition, a liquid nitrogen cooled shroud, and the vacuum pumps.

The physical size of the vacuum chamber and the layout of the component is primarily dependent on the choice of the sample transfer mechanism. The design shown in Fig. V-4 involves the use of linear and rotational motion manipulators that are compatible with the UHV requirements of the experiment. This means that sliding-turning manipulators that use elastomer seals may not be used if the system is to be baked out. The two basic types of UHV manipulators involve motion mechanically transmitted through a bellows or motion achieved by magnetic coupling through a thin walled stainless steel tube. Both types can be obtained from several manufacturers of vacuum equipment.

The magnetically coupled mechanism combines linear and rotational motion over a distance as large as 1 m. The ability to travel long distances makes this device useful in transporting the sample from the z-axis manipulator to the integrating sphere. The magnetic coupling limits the torque that can be transmitted into the vacuum system. Because of this feature, this mechanism is not suited for use in locking/unlocking of the sample holder to the sample plate. In addition, the limited torque can result in an uneven motion during the start or stop of the unit if the inertia of the unit and its load is large. This factor may also limit the accuracy to which it can be repositioned.

In the bellows sealed units, direct linear and rotational mechanical motion is transmitted into the vacuum chamber through the bellows which acts as a flexible element of the chamber wall. The advantages of this type of device are the large torque that can be delivered and the accuracy with which the manipulator can be repositioned. The linear motion is limited by the length of the bellows. Devices with linear travel up to 20 cm are listed in catalogs. Devices with longer travel would have to be made up as a special

order. The combination of rotational and linear motion into one unit (using two bellows) is very expensive compared with the magnetically coupled device. This combined unit would be best suited for the locking/unlocking z-axis transfer mechanism. Two rotary devices, which use a bellows seal, would be used to drive the sample plate in the X and Y plane.

The design of these moving components must include provisions for lubricating the contact surfaces with lubricants that are compatible with the UHV environment. In the absence of a lubricant, the friction mechanism is believed to be due to the contact of small areas on the two surfaces, the formation of chemical bonds between the surfaces, and the rupture of these bonds (Refs. V-5, V-6). In the presence of oxygen, most metals form oxide films which limit the number of bonds and also the bond strengths, thus limiting the friction between the metals. For vacuums below 10^{-8} Torr, the rate of arrival of gas to the surfaces is low and thus the rate of reformation of the oxide films is low. This is reflected in an increase in the friction between the two metal surfaces. Failure results in a great increase in wear of the surfaces and in the seizing of the surfaces as a result of cold welding.

Lubrication of the contacting metal surfaces is necessary to prevent damage to the sliding or rotating components. Greases and oils may not be used because of the danger of outgassing of these materials, which could result in a coating being formed on the samples of thermal control materials. Dry film lubricants such as molybdenum disulfide (Ref. V-7) are used in UHV system components. The service life of the film, which depends on the method of application and on the applied load, can be of the order of a thousand hours (Ref. V-8).

2. Measurement and Analysis of the Vacuum Conditions

The measurement of the total residual gas pressure and the analysis of the residual gas in the vacuum system is an important element in the operation of the solar wind simulator. An accurate characterization of the vacuum environment is necessary for several reasons which are cited below. Both before and during a test, it is necessary to verify that the vacuum environment is better than a designated standard. During the run, the partial pressure of a specific gas may change and thus indicate a change in the apparatus or the sample. Analysis of the residual gases is useful in determining the environment to which the samples are exposed.

The Bayard-Alpert ion gauge is used to measure the total residual gas pressure over the range of 1×10^{-3} to 1×10^{-10} Torr. The cost of the gauge tube is low and the cost of the control supply is moderate. As a result, it is used in almost all UHV facilities. If the system is capable of operating down to the 10^{-14} Torr range, other forms of ionization gauges can be used to measure the pressure. These include the Helmer gauge, the Redhead gauge, and the Kreisman gauge. As these units cost two or more times the price of the Bayard-Alpert units, they need not be considered unless the system is capable of operating at pressures below 10^{-10} Torr.

The most popular residual gas analyzer is the rf quadrupole mass spectrometer. Several corporations manufacture this type of instrument. These are capable of measuring partial pressures of 10^{-14} Torr, but because of the variable gain of the electron multiplier detector and the variable transmission of ions through the analyzer section, these instruments are generally used for qualitative rather than quantitative measurement of the residual gases. In addition

to electronic control of the transmission, it is possible to electronically adjust the sensitivity, the mass range of the scan, and the scan rate in order to obtain the maximum information.

In addition to locating real and virtual leaks and identifying the gases evolved from the samples due to desorption or decomposition, the residual gas analyzer is important in the accurate determination of the pressure in the vacuum system. In a system in which the residual gas is mainly hydrogen, the failure to correct for the smaller ionization cross section of hydrogen can cause a significant error in the measurement of the total gas pressure.

The response of the ionization gauge tubes is calibrated as a function of air or N_2 gas pressure. Thus, in systems which consist of N_2, O_2, CO, CO_2, and H_2O the ion gauge controller reading accurately represents the true pressure to within a few percent. Because the ionization cross section of hydrogen is a smaller value, the gauge response of hydrogen is about 0.4 (Refs. V-9, V-10) of the nitrogen value. As a result, the ionization gauge control readings for the hydrogen system must be multiplied by 2.5 to obtain the true value for the hydrogen pressure. The RGA is used to determine the relative concentration of the various gases in the system, so that the partial pressures of each gas may be determined.

3. The Use of a Sputter Ion Pump in a Hydrogen Atmosphere

The most common pump type used in UHV systems at present is the sputter ion pump. The features which favor this wide usage are the freedom from contamination by the pumping medium, the silent operation, the freedom from the need for cooling fluids such as water or cryogenic liquids, the ability to bake out the pump, the relatively simple construction, and the low operating cost. Some negative features

are the relatively high cost of the pump and its controls and the operating characteristic which causes the pump to stop operation or fail if the gas load causes the pressure to exceed about 1×10^{-2} Torr.

Under normal conditions, the sputter ion pump is a good choice for a UHV system. Systems in which hydrogen is the major gas species present are an important exception because of the unusual nature of the sputter ion pumping of hydrogen gas. This problem will be discussed in this section.

Rutherford and Jepsen (Refs. V-11, V-12) have observed that the hydrogen pumping speed of sputter ion pumps with titanium cathodes is about twice the pump's rated speed for nitrogen. The pumping mechanism for hydrogen was shown to be due to a chemical reaction (gettering) with the cathode material. This is in contrast to the normal sputtering and titanium burial mechanism by which other gases are pumped. This statement is based on the following evidence. The sputtering yield of the very light hydrogen ions is negligibly small (see Section III-B-3). Several hydrogen atoms are pumped for each electron collected at the anode. This indicates that much hydrogen is pumped without being ionized. Weighing the cathodes before and after pumping and after vacuum firing showed that the major part of the hydrogen was pumped by the cathodes. Extensive cracking and swelling of the cathodes occurred. Pumping continued after the discharge was turned off, with a time of 1×10^{3} sec for an e-fold decrease in the pumping speed.

This unique aspect (the chemical pumping of hydrogen by adsorption in the titanium cathodes) may present problems in the use of the sputter ion pump in the solar wind simulator. The cathodes, which are designed to operate for long periods of time in the normal sputter mode of operation, will swell

and crack due to the formation of titanium hydride. This could cause shorting of these electrodes to the anode. The swelling can cause the cathodes to warp, which in turn can cause a large decrease in the cathode to pump wall contact area. This contact is essential for the cooling of the cathodes. The bombardment by 5 keV ions is the cathode heat source. For a typical 500 liter sec^{-1} ion pump, the power input is 0.5 kVA at a pressure of 1×10^{-5} Torr, 3.5 kVA at a pressure of 10^{-4} Torr, and 5.1 kVA under starting conditions. If the cathode fails to make good thermal contact with the walls of the chamber, its temperature can exceed 250°C, the point at which the titanium hydride decomposes. This can lead to an increase in pressure which increases the discharge and can cause destruction of the electrode.

The best solution to this problem is to provide a large capacity titanium sublimation pump in addition to the sputter ion pump. The sublimation pump, which operates by evaporating a film of titanium over a large surface area, chemically getters all but the inert gases. With this combination the sublimation pump serves to pump the major portion of the hydrogen gas as well as all the other gases except the inert gases. The sputter ion pump is necessary for the pumping of these gases and for the inert gases.

The selection of the appropriate size of sputter ion pump and the sublimation pump can be made on the basis of the ion source operating characteristics. If the use rate of hydrogen gas is known, it is a relatively simple exercise to estimate the pump capacity needed to maintain a specific pressure in the ion beam transit chamber. For example, a commercial rf ion source has a hydrogen use rate of 4 cm^3(STP) $hour^{-1}$. If the desired chamber pressure is 10^{-6} Torr and the gas temperature in the chamber is about 300°K, the pump conductance S is determined by applying Boyle's law and Charles' law as follows:

$$S = .4 \ \frac{cm^3}{hour} \times \frac{hour}{3600 \ sec} \times \frac{liter}{10^3 \ cm^3} \times \frac{300°K}{273°K} \times \frac{760 \ Torr}{10^{-6} \ Torr}$$

$$\approx 10^3 \text{ liter-sec}^{-1} \text{ (at } 10^6 \text{ Torr)}$$

If the system is designed so that the pipe conductances are much greater than the pump conductance and thus can be ignored, the minimum pumping rate Q is given as follows:

$$\begin{aligned} Q &= SP \\ &= 10^3 \text{ liter-sec}^{-1} \times 10^{-6} \text{ Torr} \\ &= 10^3 \text{ liter-sec}^{-1} \times 10^{-3} \ \mu m \\ &= 1 \ \mu\text{liter-sec}^{-1} \end{aligned}$$

This pumping rate considers only the hydrogen gas under steady operating conditions. The total pump capacity of this portion of the system must take into account both the increased hydrogen flow which may occur as a transient condition and the normal gas load of the system.

This safety factor must be a generous one, for unlike the conventional mechanical and diffusion pumped systems which easily recover from a momentary overload, the operation of the ion pump can be seriously affected by a pressure overload. If the pressure pulse is sufficient, the power supply, which operates the sputter ion pump, changes its operating mode into a lower voltage-higher current one. This is a built-in safety feature, designed to protect the ion pump electrodes. If the pressure pulse exceeds about 5×10^{-4} Torr, the point of maximum throughput for the ion pump, both the throughput and pump speed decrease. A feedback loop develops in which the pressure continues to increase and the pumping capacity to decrease. The end result

is that the trip circuit in the ion pump power supply will shut down the system. This failure mode is rare because the systems are designed with sufficient reserve pumping capacity to take care of normal pressure bursts.

4. Theory, Design, and Operation of a Titanium Sublimation Pump.

The titanium sublimation pump operates on the principle of pumping chemically reactive gases (H_2, N_2, O_2, CO, CO_2) by gettering them on a titanium film. The film is formed by evaporating (subliming) the titanium by either direct resistive heating of a titanium wire (or a titanium wrapped heater) or by electron bombardment heating of titanium-metal. The metal is evaporated onto a cooled surface (generally water cooled but sometimes liquid nitrogen cooled) where the vacuum gases can react with the film. The advantage of this system is that it is possible to obtain very high pump speeds at a relatively low cost. The problem is that the titanium film pumps chemically reactive gases only.

The operating characteristics of a typical titanium sublimation pump are shown in Fig. V-11. Each curve on the graph is for a specific titanium evaporation rate. At the high pressure end, the residual gas arrival rate is great enough to combine with all the available titanium so that the speed is dependent on the titanium arrival rate. At the low pressure end, the pump speed is dependent on the arrival of gas from the system. This is referred to as the area limited speed of the pump. The total speed of the pump is thus dependent on the rate of titanium evaporation in the high pressure region, and on the surface area on which the metal is deposited in the low pressure range.

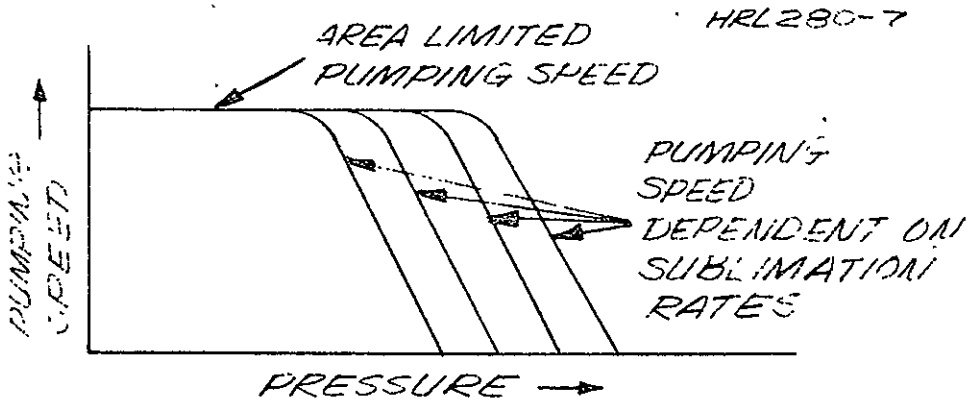

Fig. V-11. Characteristics of a titanium sublimation pump.

The area limited speed S_A of the pump can be obtained from the product of the surface area and the intrinsic speed which is given in Table V-I (Ref. V-13), and thus $S_A = S_i A$. Because of the large pumping speeds that are possible with this technique, it is critical that the conductance of the system be calculated in order to determine an accurate estimate of the net pumping speed. This is shown below.

Dushman (Ref. V-10) has formulated the following equation to approximate the conductance of a cylindrical tube of length ℓ(cm), and of radius a(cm), for a gas at a temperature T(°K) and having a molecular weight M (grams mole^{-1})

$$F = 3.64\ K'\ A \left(\frac{T}{M}\right)^{1/2} \text{ liter-sec}^{-1}$$

$$= 3.64\ \frac{1}{1 + \frac{3}{8}\ \frac{\ell}{a}}\ \pi\ a^2 \left(\frac{T}{M}\right)^{1/2}$$

The values of K' are given for values of ℓ/a. The over-all pumping speed S_R of the system which consists of a number of tubes 1, 2, etc., and the pump is given as follows

$$\frac{1}{S_R} = \frac{1}{S_A} + \frac{1}{F_1} + \frac{1}{F_2} \text{, etc.}$$

TABLE V-1

Intrinsic Speed for a Titanium Surface S_i = liter-sec^{-1} cm^{-2}

Surface Temperature	Gas					
	H_2	N_2	O_2	CO	CO_2	H_2O
20°C	3.1	4.6	1.5	9.3	7.7	3.1
-195°C	10	10	6.2	10.8	9.3	14

An example of this calculation is made for the system shown in Fig. V-3. The chamber is 34 cm long and 20 cm in diameter; the side tube is about 16 cm long and 20 cm in diameter. The sublimation pump body is about 30 cm in diameter and 34 cm long. Thus, the various calculations are given below.

$$S_A = S_i \, A_{(wall)}$$

$$= 3.1 \text{ (liter-sec}^{-1} \text{ cm}^{-2}) \text{ 34 (cm) } \pi \text{ 30 (cm)}$$

$$= 9940 \text{ liter-sec}^{-1}$$

The conductance of the side tube is

$$F_1 = (3.64)(0.625)(\pi\ 10^2)\left(\frac{300}{2}\right)^{1/2}\ \text{liter sec}^{-1}$$

$$= 8750\ \text{liter-sec}^{-1}$$

The conductance of the chamber is given by F_2.

$$F_2 = (3.64)(0.439)(\pi\ 10^2)\left(\frac{300}{2}\right)^{1/2}$$

$$= 6150\ \text{liter-sec}^{-1}$$

Thus the over-all pump speed is

$$\frac{1}{S_R} = \frac{1}{9940} + \frac{1}{8750} + \frac{1}{6150}$$

$$S_R = 2650\ \text{liter-sec}^{-1}$$

Thus the system is adequate to operate the ion source, which uses 4 cm^3 (STP) hour^{-1} of hydrogen gas.

5. Cryogenic Pumps

The use of liquid helium cooled cryogenic pumps is not advisable for a system in which the predominant gas load is hydrogen. The reason is that the vapor pressure of hydrogen is of the order of 10^{-6} Torr at a cryopump temperature of the order of 4.5 to 4.2°K (Ref. V-14). This value is poorer than that which can be obtained from the TSP and the ion pump.

F. CONTROL LOOP SYSTEMS

The continuous operation of the solar wind simulator for long periods (i.e., of the order of 1000 hours) requires the use of control circuits. The ion source pressure, which is of the order of 10 to 30 μm, is monitored by means of a capacitance manometer. This unit servocontrols a variable leak valve which adjusts the gas pressure in the ion source. The beam current at the target is monitored by means of a collector such as that shown in Fig. V-8. This information is fed back to the ion source power supplies to regulate the beam flux to the target. The same is true for the neutralizer and the photon source.

G. SUMMARY AND CONCLUSIONS

The design that has been produced satisfies all of the requirements for the simulation of the solar wind in the laboratory environment. Of the two ion sources that were analyzed in Section IV-A, the rf was used in this design. The ion optics system was designed to collimate a fine beam of protons through a 0.2 cm aperture and expand it into a 10 cm beam at the target. This has two advantages: (a) the small beam permits the use of a simple magnetic mass separator to purify the beam and (b) the small aperture permits differential pumping of the system. The use of the magnetic mass separator results in a simple design in which the problems due to energetic (charge exchange formed) neutrals and of energetic Lyman α photons from the source are avoided completely. The use of an isolation valve between the proton beam source and the sample chamber permits the pressurization of either part of the system without damage to the other half.

SECTION VI

CONCLUSIONS AND SUMMARY

Based on the foregoing discussion it may be concluded that it is practical to simulate in the laboratory the interaction between the solar wind and a thermal control coating. In order to accomplish this effectively, it is necessary to provide a mass separator that deflects the protons out of the beam of ions, neutrals, and photons which emerge from the source. It is also necessary to provide a neutralizing electron beam at the target to assure that the kinetic energy of the protons which strike the target is accurately controlled.

Based on a first order analysis, it was concluded that the results of the proton-sample interaction would be the same for a pulsed and continuous beam. If this can be verified experimentally, considerable simplicity and versatility can be achieved by rastering a small proton beam over the target area rather than expanding the small beam into a dilute broad beam.

A representative system has been described in detail in Section V. It consists of an rf proton source, a sector type mass separator and a series of einzel lenses to control the beam dimensions. The entire system is housed in a vacuum chamber which may be valved off from the main vacuum chamber to permit source repairs or adjustments without exposing the samples to atmosphere. The source chamber is separated from the main chamber by a small aperture and differentially pumped to prevent the high gas load from the source from reaching the main chamber. Separate techniques are discussed for varying the proton energy and current density at the target.

In order to pursue this optimized design further, several key experiments are required:

1. Verify the source emittance diagram experimentally.
2. Establish the current range over which the rf source will operate stably.
3. Verify the source lifetime of 10^3 hours under typical operating conditions.
4. Compare dc and pulsed proton beam interactions with the test samples.

ACKNOWLEDGMENTS

The work reported herein was carried out in the Ion Device Physics Department of the Hughes Research Laboratories. This department is managed by Mr. J.H. Molitor. The work was performed under Contract NAS 2-5585, managed by Mr. E. Streed and Mr. J. Kirkpatrick of Ames Research Center. Those contributing to this report are:

H.J. King	program manager, ion source evaluation
D.E. Zuccaro	assistant program manager, system definition and design
J.W. Ward	ion optical calculations
S. Kami	mechanical system design
F. Ault	mass separator analysis
W. Knauer, C. Berggren, H. Levine	consultants

REFERENCES

II-1. A.G. Stanley and J.L. Ryan, "Charged Particle Radiation Environment in Synchronous Orbit," Technical Report 443, Contract AF 19(628)-5157, MIT Lincoln Laboratory, 15 May 1968.

II-2. E.N. Parker, Space Sci. Rev. 4, 666 (1965).

II-3. A.J. Dessler, Rev. Geophys. 5, 1 (1967).

II-4. E.N. Parker, Space Sci. Rev. 9, 325 (1969).

II-5. A.J. Hundhausen, Space Sci. Rev. 8, 690 (1968).

II-6. S.J. Bame, A.J. Hundhausen, J.R. Asbridge, and I.B. Strong, Phys. Rev. Letters 20, 393 (1968).

II-7. J. Hirshberg, A. Alksne, D.S. Colburn, S.J. Bame, and A.J. Hundhausen, J. Geophys. Res. 75, 1 (1970).

II-8. M. Neugebauer and C.W. Snyder, J. Geophys. Res. 71, 4469 (1966).

II-9. I.B. Strong, J.R. Asbridge, S.J. Bame, and A.J. Hundhauser, in "Zodiacal Light and Interplanetary Medium," J. Weinberg, Ed., NASA SP-150, 1967.

II-10. M.D. Montgomery, A.J. Bame, and A.J. Hundhausen, J. Geophys. Res. 73, 4999 (1968).

III-1. F. Grønlund and W.J. Moore, J. Chem. Phys. 31, 1132 (1959).

III-2. Matheson Gas Products, General Catalog 27; Air Products and Chemicals, Catalog No. 5068.

III-3. D.D. Swofford, V.L. Mangold, and S.W. Johnson, Thermal Design Principles of Spacecraft and Entry Bodies, J.T. Bevans, Ed. (Academic Press, New York, 1968), p. 667.

III-4. L.A. Nelson, Handbook of Solar Simulation for Thermal Vacuum Testing, J.S. Griffith, Ed. (Institute for Environmental Sciences, 1968), p. 3-1.

III-5. J.E. Gilligan and G.A. Zerlant, AIAA Paper No. 69-1025, AIAA/ASTM/IES 4th Space Simulation Conf., Los Angeles, 8-10 September 1969.

III-6. S. Dushman, Scientific Foundations of Vacuum Techniques, J.M. Lafferty, Ed., 2nd ed. (Wiley, New York, 1962).

III-7. W.L. Fite, Ann. Geophys. (France) 20, 47 (1964).

III-8. W.L. Fite, A.C.H. Smith, and R.F. Stebbings, Proc. Roy. Soc. (London) A268, 533 (1962).

III-9. W.L. Fite, R.F. Stebbings, D.G. Hummer, and R.T. Brackmann, Phys. Rev. 119, 663 (1960).

III-10. A. Dalgarno and H.N. Yadav, Proc. Phys. Soc. A66, 173 (1953).

III-11. H.S.W. Massey and E.H.S. Burhop, Electronics and Ionic Impact Phenomena (Oxford University Press, New York, 1952).

III-12. R. Curran, T.M. Donahue, and W.H. Kasner, Phys. Rev. 114, 490 (1959).

III-13. D.W. Koopman, Phys. Rev. 154, 79 (1967).

III-14. J.P. Keene, Phys. Mag. 40, 369 (1949).

III-15. J.B. Hasted, Proc. Roy. Soc. (London) A205, 421 (1951); A212, 235 (1952); A222, 74 (1954).

III-16. J.B. Hasted and J.B.H. Stedeford, Proc. Roy. Soc. (London) A227, 466 (1955).

III-17. J.B.H. Stedeford and J.B. Hasted, Proc. Roy. Soc. (London) A227, 406 (1955).

III-18. H.B. Gilbody and J.B. Hasted, Proc. Roy. Soc. (London) A238, 334 (1956).

III-19. W.H. Cramer, J. Chem. Phys. 35, 836 (1966).

III-20. M. Kaminsky, Atomic and Ionic Impact Phenomena on Metal Surfaces (Academic Press, New York, 1965).

III-21. C.D. O'Brian, A. Lindner, and W.J. Moore, J. Chem. Phys. 29, 3 (1958).

III-22. O.C. Yonts, C.E. Normand, and D.E. Harrison, Jr., J. Appl. Phys. 31, 447 (1960).

III-23. C.R. Finfgeld, "Proton Sputtering of Polycrystalline Gold," Ph.D. Thesis, Virginia Polytechnic Institute, November 1967.

IV-1. American Institute of Physics Handbook (McGraw-Hill, New York, 1963), pp. 4-319.

IV-2. C. Goodyear and A. Von Engel, "Atomic Ion Production in Radio Frequency Ion Sources," Munich Conf. on Ion Sources, Vol. 1.

IV-3. L.J. Kieffer, "A Compilation of Critically Evaluated Electron Impact Ionization Cross Section Data for Atoms and Diatomic Molecules," Joint Institute for Laboratory Astrophysics, Report No. 30, Boulder, Colorado, February 5, 1965.

IV-4. M. Hoyaux and I. Dujardin, Nucleonics 4, 7; 4, 12; 5, 67 (1949).

IV-5. D. Blanc and A. Deghilh, J. Phys. Radium 22, 230 (1961).

IV-6. R.N. Hall, Rev. Sci. Instr. 19, 905 (1948).

IV-7. P.C. Thoneman, J. Moffatt, D. Roaf, and J.H. Sanders, Proc. Roy. Soc. 61, 483 (1948).

IV-8. ORTEC Model 320 RF Ion Source Data Sheet.

IV-9. C. Swan and F. Swingle, Rev. Sci. Instr. 23, 636 (1952).

IV-10. P.A. Redhead, Can. J. Phys. 45, 1790 (1967).

IV-11. S. Dworetsky, R. Novick, W.W. Smith, and N. Tolk, Rev. Sci. Instr. 39, 1721 (1968).

IV-12. Constructed by H.J. King and D.E. Schnelker; unpublished.

IV-13. G.O. Brink, Rev. Sci. Instr. 37, 857 (1966).

IV-14. L.P. Smith and G.W. Scott, Jr., Phys. Rev. 51, 1025 (1937); 53, 677 (1938); 55, 954 (1939).

IV-15. D. Bohm, The Characteristics of Electric Discharges in Gases (McGraw-Hill, New York, 1949).

IV-16. T. Finkelstein, Rev. Sci. Instr. 11, 94 (1940).

IV-17. F.M. Penning, Physica 3, 873 (1936).

IV-18. W. Knauer, J. Appl. Phys. 33, 2093 (1962).

IV-19. V.M. von Ardenne, Z. Phyzik 43, 91 (1942); 120, 227 (1943).

IV-20. Constructed by H.J. King; unpublished.

IV-21. Hughes Research Laboratories Staff, "Ion Engine Thrust Vector Study," Final Report, Contract JPL 952129, Hughes Research Laboratories, 1969.

IV-22. M.D. Gabovich, "Extraction of Ions from Plasma Ion Source, Instruments and Techniques of Experiment (Russian), No. 2, 1963," Air Force Translation FTD-MT-63-181, 1963.

IV-23. J. Hyman, Jr., W.O. Eckhardt, R.C. Knechtli, and C.R. Buckey, AIAA J. 2, 1739 (1964).

IV-24. N.B. Kramer and H.J. King, J. Appl. Phys. 38, 4019 (1967).

IV-25. O. Reifenschwerber and K. Frohner, Nucl. Instr. Methods 30, 398 (1964).

IV-26. W.H. Bennett, J. Appl. Phys. 21, 143 (1950).

IV-27. P.A. Redhead and C.R. Crowell, J. Appl. Phys. 24, 331 (1953).

IV-28. R. Lebduska and B. Meckel, "Solar Wind Simulator and Advanced Design with Extended Operational Capabilities," AIAA Paper No. 70-31, January 1970.

IV-29. M.G. Inghram and R.D. Haydon, Handbook on Mass Spectroscopy (Nuclear Science Series, National Academy of Science, Washington, D.C., 1954), No. 14.

IV-30. R.M. Sternheimer, Rev. Sci. Instr. 23, 629 (1952).

IV-31. S. Penner, Rev. Sci. Instr. 32, 150 (1961).

IV-32. W. Bleakney and J. Hepple, Phys. Rev. 53, 521 (1938).

IV-33. K. Ogilvie and R. Kittredge, Rev. Sci. Instr. 39, 459 (1968).

IV-34. L. Wahlin, Nucl. Instr. Methods 27, 55 (1967).

IV-35. K. Spangenberg, Vacuum Tubes (McGraw-Hill, New York, 1948), p. 394.

IV-36. M. Cotte, Ann. Phys. (Paris) 10, 333 (1938).

IV-37. A. Galets and P. Rose, "Optics of Electrostatic Accelerator Tubes," in Focusing of Charged Particles, A. Septier, Ed. (Academic Press, New York, 1967).

IV-38. H.R. Enge, "Deflecting Magnets," in Focusing of Charged Particles, A. Septier, Ed. (Academic Press, New York, 1967), Vol. 2, p. 211.

IV-39. F. Heise and O. Rang, Optik 5, 201 (1949).

IV-40. Spangenberg, op. cit., p. 425.

V-1. H.S. Bridges, et al., Space Res. 3, 1113 (1963).

V-2. G. Kuskevics, J. Appl. Phys. 39, 4076 (1968).

V-3. D.M. Jamba and O. Husmann, J. Appl. Phys. 38, 2630 (1967).

V-4. L.A. Nelson, op. cit., Section 3.

V-5. F.P. Bowden and D. Tabor, Friction and Lubrication of Solids II (Oxford University Press, New York, 1964).

V-6. E. Rabinoqicz, Friction and Wear of Materials (Wiley, New York, 1965).

V-7. V.R. Johnson and G.W. Vaughn, J. Appl. Phys. 27, 1173 (1956).

V-8. R.W. Parcel, et al., Trans: AVS Vac. Symp. 10, 3 (1963).

V-9. W.G. Brombacher, "A Survey of Ionization Vacuum Gauges and Their Performance Characteristics," NBS Technical Note 2098, National Bureau of Standards, 3 February 1967.

V-10. S. Dushman, op. cit., p. 324.

V-11. S.L. Rutherford and R.L. Jepsen, Rev. Sci. Instr. 32, 1144 (1961).

V-12. S.L. Rutherford, S.L. Mercer, and R.L. Jepsen, 1960 Seventh National Symposium on Vacuum (Pergamon Press, New York, 1961).

V-13. B.E. Kietzmann and D.R. Robertson, "General Characteristics of Titanium Sublimative Pumps," Report No. VAC 2224A, Varian Associate Vacuum Division.

V-14. E.S. Borovik, S.F. Grishin, and Ya. Grishina, Soviet Phys. — Tech. Phys. 5, 506 (1960).

APPENDIX A

ANALYSIS OF A SCANNED PROTON BEAM TECHNIQUE

I. INTRODUCTION

From an engineering standpoint, the fabrication of a proton gun using a scanned beam to achieve uniform irradiation offers several advantages over a flooded beam approach. This includes uniform irradiation with a simpler intensity control.

In considering the use of a rastered beam, however, the possibility of effects on the kinetics of color center production must be examined. The goal of a successful simulator is to produce, for a given proton dose, the same color center density that would be obtained in the low flux, uniform irradiation of the space environment. Two aspects of the rastered versus flooded beam approach may affect the ultimate color center density; these are the higher rates associated with the rastered beam and the dead time where the raster spot is sweeping the remainder of the sample.

The following discussion considers a number of aspects of the color center production and defines the dependence upon the irradiation mode. Specific examples are given in Ref. A-1. The processes considered are

- Displacement Production
- Electronic Transitions
- Color Center Density

It is concluded that for rates practical for laboratory simulation, the rastered and flooded beam will result in the same defect level for equal proton doses.

II. PROTON BEAM PARAMETERS

For the current discussion, we will consider an idealized rastering action. For this, the total beam current on the sample will be considered constant, because the flux in the rastered beam is higher by the ratio of the sample area to the area of the beam spot size ($A/\Delta A$). We will also consider that there is no overlap on the beam sweep, and the dead (flyback) time is zero. The beam geometry is taken as rectangular, and the exposure time of an element of area t is then related to the raster rate t_o by $t = (\Delta A/A)\, t_o$. The raster time t_o is the total time required to sweep the entire sample.

III. DISPLACEMENT PRODUCTION

The displacement yield of protons in the kiloelectron volt region has been shown to be of unity order in typical pigment materials. Specifically for MgO, the yield varies from 0.72 displacements/proton at 1 keV to 1.71 displacements/proton at 3 keV. These values were determined on the basis of the Lindhard theory and are developed in detail in Ref. A-1.

The equation describing the increase in displacement density with fluence developed in Ref. A-1 considers several factors. These include

- Initial separation less than a minimum critical distance r* will result in immediate recombination of the vacancy interstitial pair.
- The distribution in energy received by the target ion and the resulting distribution in displacement distance.

- The material parameters that determine nuclear cross sections and displacement ranges.

This model was solved analytically within the dependence on the parameter r*. The resulting equation was found to depend only upon the total fluence (i.e., the flux appears only in terms involving the product of flux times time) and therefore, would indicate no dependence upon irradiation mode, rastered or flooded.

The model would break down, however, if the density of mobile ions ever increased until there was a significant interaction between them. The previous development considered a mobile ion in an otherwise perfect lattice structure. In order to estimate the time scale for such processes, we may consider the velocity of the moving ion. The average energy transferred to the target ion is the order of 20 eV for protons in the low kiloelectron volt range and target ions of the order of 25 AMU's. A simple calculation of the velocity yields approximately 10^6 cm/sec. In Ref. A-1 an average range of displacement was shown to be the order of a few Angstroms, indicating a displacement time the order of 10^{-14} sec. This energy is then released to the lattice as thermal vibrations and may as a worst case estimate be taken as the order of 10^{-11} sec (Ref. A-2).

The most difficult number to define is the density of mobile ions at which interactions become important. A rough estimate may be made as follows. The average displacement distance is approximately two to three lattice spacings (Ref. A-1). Extending this to five for a worst case, the volume associated with each moving ion is then on the order of 500 lattice sites $(4/3)\ \pi r^3$, r = 5. The point at which there would be a 1% chance that two moving ions are created within this volume is given by

$$500 \cdot N_d = 0.01 \cdot N_o$$

where

$N_d \equiv$ mobile ion density = 1 cm^3

$N_o \equiv$ target ion density = 1 cm^3

For MgO, the value of N_o is approximately 5×10^{22} resulting in a density of $N_d = 10^{18}/cm^3$.

The actual density of mobile ions is given by

$$N_d = \frac{N' \Phi t_D}{R_p}$$

where

$N' \equiv$ displacement yields/proton
$\Phi \equiv$ proton flux
$t_D \equiv$ time constant on displacement production
$R_p \equiv$ proton range ($\sim 10^{-6}$ cm)

Inserting the numbers from above, we obtain

$$\Phi = \frac{N_d R_p}{t_D}$$

$$= \frac{10^{18} \times 10^{-6}}{1 \times 10^{-11}} = 10^{23} \text{ protons/cm}^2$$

which exceeds the practical limits possible for laboratory simulation by several orders of magnitude.

For displacement production, it may then be concluded that

- High rate effects will not occur until fluences well in excess of practical simulation levels are reached.
- At working flux levels, the displacement density is a function of the total fluence only and therefore will not vary between the rastered and flooded mode of irradiation.

IV. ELECTRONIC TRANSITIONS

As with displacement production, the possibility of high rate effects upon analysis of the electronic transitions involved in color center production must be considered. The method of analysis is typically based upon a set of rate equations which describe the generation, trapping, and recombination of the electron-hole pairs produced by the proton. The particulars of these equations will vary with the materials, but may be described by considering a specific set. Again, we refer to the MgO study of Ref. A-1; the general technique of rate equation analysis received a thorough discussion in Ref. A-3.

Consider first the rate of production of free holes:

$$\frac{dp}{dt} = g + \frac{p_h}{\tau} - k_1 p(H - p_h) - k_{2p} R$$

where

$p \equiv$ free hole density
$g \equiv$ ionization rate
$p_h \equiv$ trapped hole density (color center)
$\tau \equiv$ thermal trap lifetime
$k \equiv$ rate constant
$R \equiv$ recombination center density.

The first term is the number of electron-hole pairs created per unit volume and time. The second represents an increase in free holes due to thermal release of trapped carriers. The third term describes hole trapping and the last describes recombination.

The corresponding equation for trapped hole density is

$$\frac{dp}{dt} = k_1 p(H - p_h) - \frac{p_h}{\tau}$$

and it must also be noted that H is really a function of time. The value of τ is known from bleaching studies and for centers which pose a problem to long missions will be of the order of hours or longer. The value of g is estimated at worst case by assuming that all the energy goes into ionization and an energy of three times the band gap, on the average, is required to form an electron hole pair. Therefore,

$$g = \frac{\Phi \cdot R_p}{R_p (3E_g)}$$

where

$E_p \equiv$ proton energy

$R_p \equiv$ proton range

$E_g \equiv$ band gap

Thus, for an insulator such as MgO

$$g_{3KeV} \sim \frac{\Phi \cdot 3 \times 10^3}{30 \times 10^{-6}} = 10^8, \Phi$$

The recombination centers R are provided by impurity levels such as C_r and F_e in MgO. The density may be estimated from the impurity analysis and for 100 ppm material would be of the order of 10^{18} centers/cm^3. The rate constants k and k_2 are given by the product of thermal velocity of the free carrier and interaction cross section. For a coulomb attractive center, which the R center would be expected to be, we obtain

$$k_2 = \bar{v}s \simeq 10^{+7} \times 10^{-13} = 10^{-6} \quad \frac{cm^3}{sec}$$

The constant k_1 may vary from the same to three orders of magnitude smaller. The possibility of dependence upon radiation mode is associated with the difference in flux between the rastered and flooded beam. The possibility of high rate effects may show up in two ways. First, if the density of free carriers exceeds $10^{19}/cm^3$, the direct interaction between carriers becomes important and would negate the validity of the set of rate equations. Second, if the free carrier density is the order of the recombination center density R, then R will not remain a constant but must be determined by additional rate equations. The additional equations would involve more parameters which must be determined and limit the usefulness of the model.

We may estimate the free hole density by considering the first rate equation. During radiation, the direct generation of free carriers would exceed the thermal trap release in most circumstances. The initial concentration of H centers will be approximately equal to R (one positve ion vacancy is generated for each two trivalent impurity ions) and p_h will be much less than H:

For the case of MgO, and generally most other material, the trapping cross section will be much less than the recombination cross section. Considering these assumptions, a good approximation for early time is

$$\frac{dp}{dt} = g - k_2 p R$$

From this, the effective lifetime is seen to be $\tau_p = 1/k_2 R = (10^{-6} \times 10^{8}) = 10^{-12}$ sec. and the free carriers will be in equilibrium on a time scale that is very rapid compared with irradiation times. Therefore,

$$p \sim g/k_2 R = 10^{8} \Phi/k_2 R \quad .$$

For the numbers quoted above for MgO, $p = 10^{-4}\Phi$. As in the case of defect production, we again find a flux exceeding normal simulation levels is required to produce high rate effects. For example, a flux of 10^{14} protons/cm^2/ sec would be typical of the rastered beam which makes $p \sim 10^{10}$ holes/ cm^3 $<< 10^{18}$.

In summary, we may conclude

- High rate effects would only occur above 10^{21} protons/cm^2/sec, which is well in excess of laboratory simulation levels.
- Rate equations describing production of free carriers will not depend on the irradiation mode, rastered or flooded.

V. COLOR CENTER DENSITY

Subsequent to the production of displacements, the vacancies may capture free carriers which may then display an absorption band in the solar spectrum. These color

centers provide the mechanism by which thermal energy is transmitted to the coating.

The steady state density of color centers will depend on the displacement density and thermal depth of the trapping center. To represent a serious problem for thermal control surfaces, the room temperature lifetime must be on the order of hours or greater.

Possible effects of irradiation mode (rastered or flooded) upon the color center density may result from heating effects on the raster rate relative to bleaching times.

The rate equation for color center production was

$$\frac{dp_h}{dt} = k_{1p}(H - p_h) - p_h/\tau$$

The coefficient k_{1p} was estimated as

$$k_{1p} = (10^{-9})(10^{-4})$$
$$= 10^{-13}\ \Phi$$

in Section III of this Appendix. Practical levels for Φ may vary from 10^{+9} (flooded beam, low rate) to 10^{+15} (rastered beam, high rate). The value of $1/\tau$ for a several hour lifetime is on the order of 10^{-4}. Since $p_h \leq H$ for all values of time, the thermal bleaching term is important only when $p_h \sim H$. At low proton flux levels, the free hole density is approximately constant at the value of g/k_2R and the color center density will be governed by the value of H, which was shown earlier to depend only upon the total fluence and not the flux. At high flux rates, the coefficient k_{1p} is of the order of unity and any deviation of p_h from H would be changed rapidly (on the order of seconds) and p_h would closely track the value of H, again resulting in a dependence only upon total fluence.

The second question of raster time relative to thermal bleaching time may be considered in terms of the average time color centers have been available for thermal bleaching. Consider the color centers generated during a time equal to one raster cycle. Those generated by the rastered beam may be considered as generated at the start of the cycle and would then have the cycle time plus the remainder of the experiment to bleach. Those generated by the flooded beam have an average of half the cycle time plus the remainder of the experiment to bleach. Obviously, for raster rates much greater than the total irradiation time, this difference is insignificant. Typical raster rates are 10^3/sec and total irradiation times are typically $>10^3$ sec; therefore, the raster time is insignificant compared with irradiation time.

In summary, we may conclude

- Color center density is determined by defect density and, therefore, is a function of total fluence. Mode of irradiation, rastered or flooded, is not significant.
- The relation of bleaching time to raster rate is insignificant for typical operating procedure.

REFERENCES

A-1. H. Levin, et al., "Study of Color Center Formation in White Power Compounds," NASA CR 73337 July 1969.

A-2. G.J. Dienes, Radiation Effects in Solids (Interscience, New York, 1957), Vol. II., p. 37.

A-3. R.H. Bube, Photoconductivity of Solids (Wiley, New York, 1960)